A Study of Ship Wave Resistance From an Analysis of the Wave Pattern using Close Range Photogrammetry

by

A.J.C. PATERSON
B.Sc (Civil) Engineering, Cape Town

A thesis submitted to the
University of Cape Town
in partial fulfillment of the requirements
for the degree of
Master of Science in Engineering

October 1986

Department of Civil Engineering
University of Cape Town

to my parents

DECLARATION

I, Angus John Cawood Paterson, hereby declare that this Thesis is my own work and that it has not been submitted for a degree at any other university.

Signed by candidate

A.J.C. PATERSON

October 1986

SYNOPSIS

In this thesis the wave pattern generated by a moving ship is investigated experimentally using close range photogrammetry. The author has been primarily interested in validating a new approach in the determination of the wave making resistance of a ship by means of the energy contained within the wave pattern. Secondary considerations were the measurement of the total ship resistance and other dynamically related applications; squat and trim, bow and stern wave profiles and their interactive effects.

The proposed theoretical approach in this analysis of the wave resistance from the wave pattern is essentially phenomenological. As a ship proceeds through the fluid, it generates a set of waves radiating from the bow and stern due to the pressure differences along the hull. Energy is needed to maintain this system and is supplied at a constant rate by the ship, this being the energy required to overcome wave-making resistance. If the total change in energy within the wave pattern can be evaluated over a time interval associated with a known ship movement, then the energy difference will be a related to the wave making resistance.

To verify this proposal the wave height contour plots of a Series 60 (C_B = 0,60) model ship were analysed for a range of Froude numbers. The work done by the ship in propagating the wave pattern was found by numerically integrating the square of the wave elevations to obtain the energy concentrations along each of a series of transverse profiles normal to the sailing line. These consecutive values were further integrated along the length of the sailing line to find the energy contained within the boundaries of the wave field. Thus the wave resistance could be found by calculating the energy increase in a known time interval caused by the work done in moving the ship over a known distance.

A unique photogrammetric wave height measurement technique previously installed at the wave basin was used to obtain the water surface elevation contour plots. The accuracy is estimated to be within 2 mm. For this present analysis, however, certain modifications to the wave basin to accommodate the requirements of model towing were necessary. The total resistance was measured using two methods, a load cell/data acquisition

unit and a sensitive spring balance. Some 20 stereopairs were analysed to obtain results of squat, trim and hull wave profiles.

The basic theory applicable to ship resistance and fluid dynamic drag is presented, along with analytical and experimental methods of determining the resistance components of a ship. A brief description of the photogrammetric procedures and equipment is given.

Finally, there is a comparison of the experimentally measured results with previous work. The total resistance curves agree extremely well, deviations occurring due to possibly either the small size of the model, i.e. scale effects, or the sensitivity of the towing system, the model being unrestrained and sensitive to phase shifts of the bow and stern waves. A comparison of total resistance, squat, trim and hull wave profiles shows the interactive effects of these on each other. The wave resistance results correspond well in the lower speeed ranges but are consistently higher in the upper ranges. This could be due to two main causes, either the short towing distances involved leading to the measurement of accelerated wave systems at higher speeds and the inclusion of the near field effects, or the neglect of the energy contained beyond the boundaries of the integration.

General conclusions are:

(1) the photogrammetric technique employed yields excellent deformed surface results, the wave pattern being undisturbed by measuring devices;

(2) the dynamic effects of total resistance, and the kinematic results of squat, trim and hull wave profiles are generally fairly consistent despite the limited size of the wave basin.

(3) the proposed method of evaluating wave resistance from the wave pattern is accurate in the lower speeds but yields excessively large forces at the higher speeds, suggesting possible errors due to accelerated waves, shoaling water or neglect of a term becomes significant as the wave celerities increase.

ACKNOWLEDGEMENTS

I would like to thank my thesis supervisors Professor F.A. Kilner of the Department of Civil Engineering, and Professor L.P. Adams of the Department of Surveying, University of Cape Town, for their help and guidance during the two years of this study. Their encouragement, constant enthusiasm and interest were much appreciated.

A particular word of thanks must go to Dr John Pos of NRIO on whose work the wave basin photogrammetric aspects are based, and for his advice during the initial stages of this thesis.

My thanks also to Professor Heinz Rüther and particularly Miss Ann Tregidga of the Department of Surveying for their help, experience and assistance regarding the stereocomparator and computer analysis procedures used during the photogrammetric analysis stage.

I extend thanks to the technical staff, Messrs R.F. Beverton, G. Bertuzzi, D.J. Botha and R. Edge, who helped me with the construction and alterations needed for the experimental photogrammetric wave basin configuration and model towing apparatus. I would also like to thank Messrs J. George, A. Siko and J. Williams for their practical aid and assistance throughout the construction and experimentation stages.

My thanks are also due to the staff of the Department of Civil Engineering for general assistance throughout the two years of the study.

CONTENTS

CONTENTS (continued)

CONTENTS (continued)

CONTENTS (continued)

LIST OF TABLES

LIST OF FIGURES

LIST OF FIGURES - Continued

LIST OF FIGURES - Continued

NOMENCLATURE

A_x	Area of midship section
B	Beam at Midship
C	Resistance coefficient, $C = R/(^1/_2 \rho U^2 S)$
	(with subscripts: pr for pressure resistance; r for residual; t for total; v for viscous; f for frictional; w for wave-making; wb for wave breaking; wp for wave pattern)
C_B	Block coefficient
C_{PR}	Prismatic coefficient
C_S	Wetted surface coefficient
C_X	Midship section area coefficient
E	Energy in wave train
$\overline{E}$	Average energy per metre along sailing line ($^N/_m$ per metre)
Fn	Froude number, $Fn = U/\sqrt{gLWL}$
G_0	Free stream dynamic head ($^1/_2 \rho U^2$)
G_1	Measured total head
H	Draught at Midship
H_f	Flying height (photogrammetric)
L	Wavelength
LWL	Length at water line
L_{pp}	Length between perpendiculars
P_1	Static head due to wave elevation
R	Resistance
	(with subscripts: pr for pressure resistance; r for residual; t for total; v for viscous; f for frictional; w for wave-making; wb for wave breaking; wp for wave pattern)
R_n	Reynolds number, $R_n = U.L/\nu$
S	Wetted surface area at rest
S_1, S_2	Camera positions
U	Ship or Model Speed
V	Displaced Volume
b	Half beam, $b = B/2$
d	Drag function, $d = f(P_1, G_1, G_0)$
g	gravitational acceleration
h(x)	Vertical distance between x-axis and x'-axis (positive above undisturbed free surface); nondimensionalized by $U^2/2g$
h	Wave basin water depth

k	Wave number, $k = g/U^2$
ℓ	Half length, $\ell = L_{pp}/2$
p	Pressure
p_a	Atmospheric pressure
t	Trim (positive for bow up) nondimensionalized by $U^2/2g$
s	Sinkage, nondimensionalized by $U^2/2g$
$\zeta(x)$	Wave elevation along hull, measured relative to the undisturbed free surface plane; nondimensionalized by $U^2/2g$
μ	Viscosity
ν	Kinematic viscosity
ρ	Mass density
x, y, z	Translating coordinate system with x in the opposite direction of the ship's forward motion, z vertically upward, and the origin at the intersection of the planes of the undisturbed free-surface and the midship section.*
x', y', z'	Coordinate system fixed in ship and coinciding with the x-y-z when ship is at rest.

* Midship section is, by definition, at the midpoint between perpendiculars

Subscripts

m	model
p	prototype

1. INTRODUCTION

The determination of ship wave resistance from the analysis of the wave pattern has been a topic of great interest for many years. Present methods predicting wave resistance, both experimentally and analytically, involve the solutions to complex differential equations. This thesis describes research carried out by the author to experimentally determine the wave making resistance of a model ship moving through a calm sea via a detailed analysis of the wave pattern. A novel approach was developed involving the direct integration of the energy contained within the wave pattern.

Sophisticated equipment existed at the UCT Civil Engineering Department to enable the precise mapping of the deformed water surface in a three dimensional wave basin using close range photogrammetry. This apparatus was modified to suit the requirements of model towing. The primary objective of this thesis was to evaluate the proposed energy analysis method of determining wave making resistance utilising the photogrammetric procedures. Secondary considerations were the determination of total resistance, ship squat and trim and hull wave profile measurements.

Chapter two deals very briefly with the historical background to ship wave research dating from the 18th century to the present, highlighting the work of W. Froude and the advances made in ship resistance prediction.

Chapter three deals largely with the theory of ship resistance. A brief review of applicable naval architecture terminology is given. The concept of fluid dynamic drag is discussed and expanded upon, covering the various interactive effects due to frictional and wave making resistance. Elements of first order wave mechanics are presented to facilitate an understanding of ship generated waves.

Chapter four reviews experimental methods and approaches used to determine the various components of resistance and comments on past experimental work and results. The approach used in this study to

determine wave making resistance is derived and presented.

In chapter five the photogrammetric and wave height measurement procedures and techniques used to obtain the water surface contour plots is described in general detail. Laboratory equipment is explained and various alterations to the wave basin to facilitate the photogrammetric procedures are described.

The experimental work performed by the author is described in chapter six. Modifications to the wave basin and surrounding area, including the towing apparatus and force measurement techniques are presented along with illustrations. The measurement procedures for total resistance, squat, trim and wave making resistance are discussed.

In chapter seven the experimental results obtained for the total resistance coefficient curves are compared with past results and deviations discussed. The results of squat and trim measurements are provided along with measurements of the hull wave profiles and evaluated to corroborate the total resistance trends. The generated wave pattern contour maps for five Froude numbers are presented, along with the photogrammetric stereopairs, which can be viewed using a pair of stereoscopic viewers. The derived wave making resistance calculations are discussed and compared, deviances are explained and a critical analysis of the propsed method is included. A brief photographic comparison of ship wave patterns is presented.

In chapter eight, general conclusions are given regarding ship resistance, laboratory photogrammetric wave height measurements, and the use of the proposed method of ship wave resistance determination.

2. HISTORY OF SHIP WAVE INVESTIGATIONS AND SHIP RESISTANCE

The study of ship-produced waves using ship models has interested both naval architects and engineers for several centuries. One of the first noted treatises on Naval Architecture published by the famed mathematician, Euler, in 1773 stated the following concerning ship models:

> "From good Models in Miniature which represent Vessels exactly as they are, very important Experiments upon the Resistance of Vessels may be very usefully made; and which is so much necessary, as the Theory upon the Subject is still very defective."

From these origins the study of ship generated waves has been a source of great interest but the above statement still holds true today. However, there still persists a great deal of uncertainty regarding the accuracy of present analytical and experimental methods of calculating the various forms of resistance.

Euler referred to Sir Isaac Newton's theory of fluid resistance based upon the notion that the resistance resulted directly from the impact of the fluid particles on the forebody of the object, resulting in a differential equation from which the solid of least resistance could be calculated. Euler (1755) and d'Alembert (1752) both demonstrated what is known as d'Alembert's paradox, the zero resistance of bodies in uniform motion through an ideal fluid, and Euler stated that the whole hull had to be considered when dealing with resistance problems. Newton's concept was not finally dismissed until Froude had completed his work, and dominated ship building ideas for almost two centuries.

In the period between Newton and Froude a large number of individual experiments were carried out using a towing cable and falling weights. d'Alembert (1775) showed that the resistance of ships increased, not as the square of the speed and originally thought, but more rapidly, and demonstrated the effects of stern shape and

water depth on drag. The first frictional plank testing was performed in a 120 m dock by Beaufoy in London in the period 1791 to 1798 and quantified the importance of frictional effects. John Scott Russell during the period 1834 - 1840 discovered what he termed "the great primary wave of translation" using both horsepower and falling weights.

In 1870 a meeting of the Royal Institute of Naval Architects was chaired by Russell to discuss the proposal of one William Froude, a retired civil engineer, for the Admiralty to develop a model basin for the scientific testing of ship models. After much debate concerning the lack of agreement and inaccuracies of results to date when comparing model to prototype, Froude answered "... attention has not been paid to the relation which should subsist between the speed at which the model is moved and the speed at which the ship is moved".

This significant relation between model and prototype was the foundation for the science of model towing tank testing as we know it today. Froude devised and constructed his own equipment, towing trolleys, dynamometer and cutting machines to shape models of hard paraffin wax.

Froude proposed that the resistance of a ship at sea consists of surface friction, eddy resistance and wave resistance. He described wave resistance as follows: "... the ship in its passage along the surface of the water has to be continually supplying the waste of an attendant system of waves, which, from the nature of their constitution as independent waves are continually diffusing or transmitting themselves into the surrounding water, or where they form what is called broken water, crumbling away into froth. Now waves represent energy, or work done, and therefore all the energy represented by the waves wasted from the system attending the ship is so much work done by the propellor ...". The wave pattern, composed of both transverse and divergent waves, generated by a moving ship, was described as follows: "the whole wavemaking resistance is the resistance expended in generating first the

diverging bow waves, which as we have seen, cease to act on the ship once they have rolled clear of the bow; secondly, these transverse waves, the crests of which remain in contact with the ship's side, and thirdly the terminal wave, which appears independently at the stern of the ship."

Froude's observations were based on his experimental work. Subsequently, in the late 19th century, Lord Kelvin presented a mathematical theory to describe the crest pattern for a system of waves generated by a moving pressure point, moving at constant velocity over deep water. The pattern is generally correct but does not describe the complete pattern which is generated by a moving vessel. This was to an extent overcome by Havelock (in 1908), who extended the theory to shallow water wave conditions.

Michell in 1898 investigated the wave pattern around the hull of an idealised thin vessel moving through an inviscid fluid. By integrating the pressure distributions over the wetted hull he deduced the wave making resistance of the vessel.

Guilloton devised a method (1960) to calculate the wave surface geometries by breaking down the ship form into a series of wedges distributed evenly along the hull, each wedge contribution being summed to give the final wave pattern.

These methods have not been perfected for practical vessels, only those of thin ship form, and required that the hull be simplified and fixed with respect to the water level (neglecting squat and trim) and effects of the boundary layer are largely ignored or accounted for empirically.

Since the 1960's a concerted effort has been made by naval architects and harbour and coastal engineers to measure ship waves (Sorenson, 1966, 1969) of both model and prototype. Naval architects (Inui, 1962, 1984) are using these observations to produce forms of minimum resistance and recently advances have been made using computers to describe the three-dimensional wave pattern (Miyata, 1985). The

civil and coastal engineer is concerned with the wave systems of moving ships in harbours and estuaries and the erosion of shorelines in channels by ship waves. Shallow water waves also invoke great interest as complex variations occur due to the effects of the seabed.

Ship wave investigations thus cover a wide field of applications of relevance to many disciplines, including naval architects and coastal engineers.

3. THEORY

3.1 Introduction

In this chapter a brief introduction to ship nomenclature is given. The concept of fluid dynamic drag and the relevant laws of dimensional similarity and comparison are discussed. Ship resistance is presented in detail, including the traditional and more recent methods of determination and separation of the individual components. Skin friction and boundary layer phenomena are explained, along with wave making resistance, its cause and its growth. To facilitate an understanding of ship generated waves, first order wave theory is presented along with general characteristics of the wave pattern. A broader account of experimental investigations of wave resistance is given chapter 4.

3.2 Definition of ship terms

3.2.1 Ship geometry

To present a complex three-dimensional form such as a ship hull requires the definition of length, breadth and depth. The three basic ship plan projections are the sheer plan, the half breadth plan and the body plan shown in Fig. 3.1.

The planes parallel to the base of the ship are known as the waterlines and are shown on the half breadth plan. One of the waterlines is known as the designed waterline (DWL), where the ship is designed to float at a predetermined load. The length of the DWL is known as the length on the waterline (LWL). Taking a series of sections perpendicular to the length of the ship at regular intervals results in the body plan, the first section forward being called the forward perpendicular (FP) and the sternmost one, the after perpendicular (AP). The distance between these extreme stations is known as the length between perpendiculars (Lpp). The section halfway between the first and last section is the midship section, the position at which the breadth or beam of the ship is measured. The draught

(depth) is the vertical distance between the base line and the designed waterline and can be represented by measurements taken at different stations.

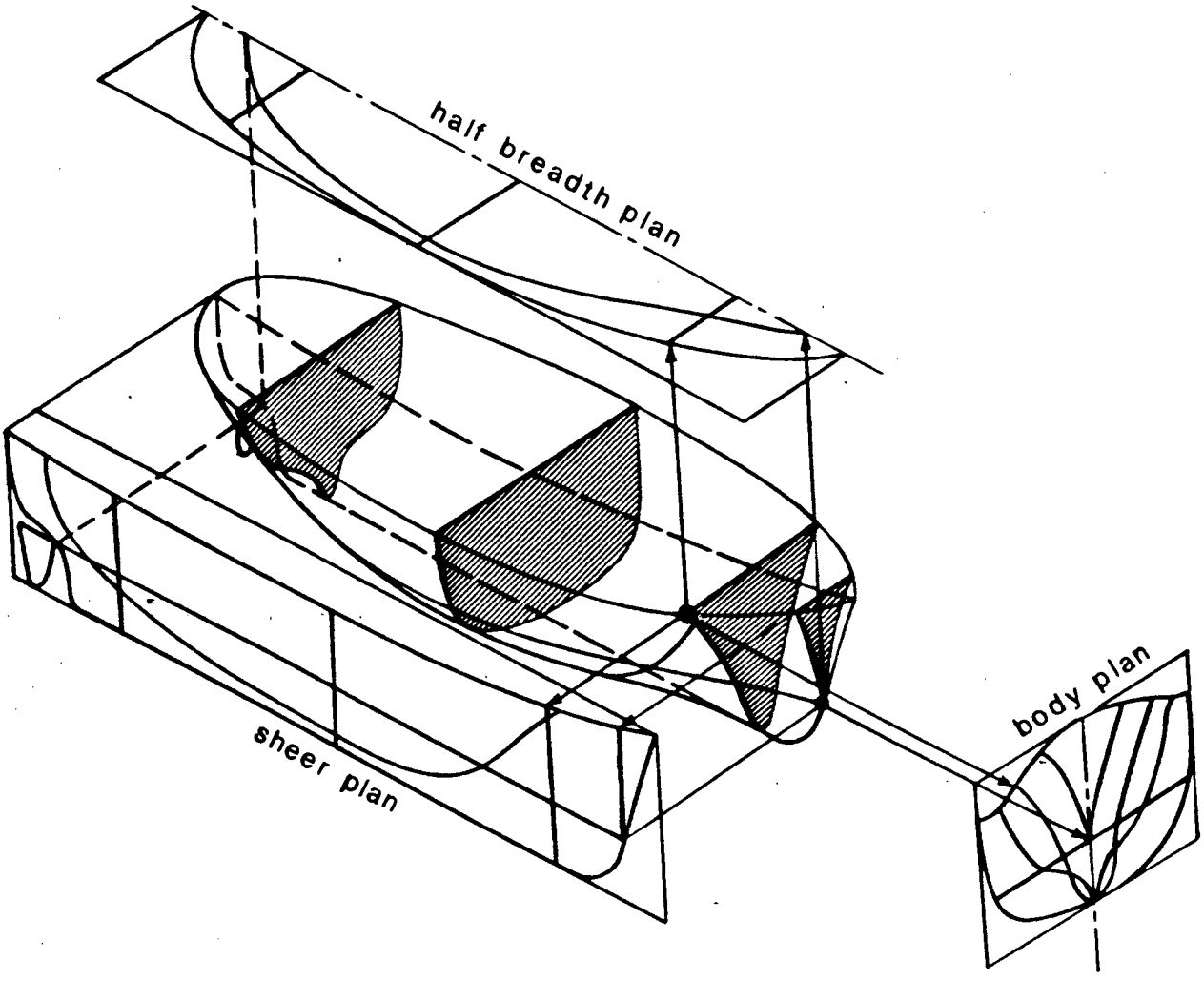

Fig. 3.1: Projection of Ship's Lines

The displacement is the weight of water that the ship displaces when it is floating freely at the DWL and can be calculated using Archimedes' principle: "A body immersed in a liquid is acted upon by a vertical upward force which is equal to the weight of the liquid displaced".

Several form coefficients are used to refer to certain proportionate measurements of a ship. These coefficients are useful in the com-

parison of ship performance characteristics. The most widely used is the block coefficient, C_B, defined as the ratio of the displacement volume of the vessel to its circumscribing rectangle, the length between perpendiculars. (Refer to nomenclature for definition of symbols.)

$$C_B = \frac{V}{Lpp.B.H}$$

Other coefficients used to define a ship's form are:

Prismatic coefficient, $$C_{PR} = \frac{V}{A_X \, Lpp}$$

Midship section area coefficient, $$C_X = \frac{A_X}{BH}$$

Wetted surface coefficient, $$C_S = \frac{S}{Lpp(2H+B)}$$

A comparison of these coefficients is shown in Table 3.1 (Gillmer 1975).

Table 3.1: Typical form coefficients

Coefficients	Destroyer	Cargo Liner	Harbour Tug	Bulk Freighter	Passenger Liner
C_B	0.521	0.643	0.585	0.874	0.597
C_X	0.833	0.967	0.892	0.990	0.956
C_{PR}	0.625	0.644	0.655	0.883	0.625

3.2.2 Ship squat

As a ship proceeds through the water, a large mass of water is forced ahead of her. This volume of water returns down the sides and under the keel, causing an increase in the flow streamlines under the ship, resulting in a decrease of pressure and the ship dropping vertically in the water (see Fig. 3.2).

Ship squat is defined as the average decrease in the keel clearance forward and aft and is given as:

$$S = -(h(bow) + h(stern))/2 \qquad \text{(Eq 3.1)}$$

$$= -(h(-\ell) + h(\ell))/2$$

On smaller vessels ship squat has always been of the magnitude of centimetres and thus inconsequential. However, with the advent of the supertanker, underkeel clearances have been reduced drastically in existing harbour approach channels to the order of 1,0 to 1,5 m (Barass, 1979).

Ship squat is affected by the speed of the ship and varies approximately as the velocity squared. An empirical result quoted by Barass (1979) based on some 300 observations of models and prototypes states, for open water conditions:

$$\text{Squat, } S = \frac{C_B \times U_k^2}{100} \text{ metres} \qquad U_k \text{ is in knots}$$

In restricted waters the squat increases due to the effects of the channel sides and bottom. The shallow water conditions affect the manoeuvrability of the vessel and the speed can drop to as much as 60% of the service speed in confined channels.

3.2.3 Trim

The squat is a measure of the mean vertical change of level of the keel, whereas the trim is a measure of the relative positions of the bow and stern to each other (Fig. 3.2). A change of trim is measured by the sum of the changes in draught at the bow or stern or can be represented by an angle of trim.

$$\text{Trim, } t = h(bow) - h(stern) \qquad \text{(Eq 3.2)}$$

$$= h(-\ell) - h(\ell)$$

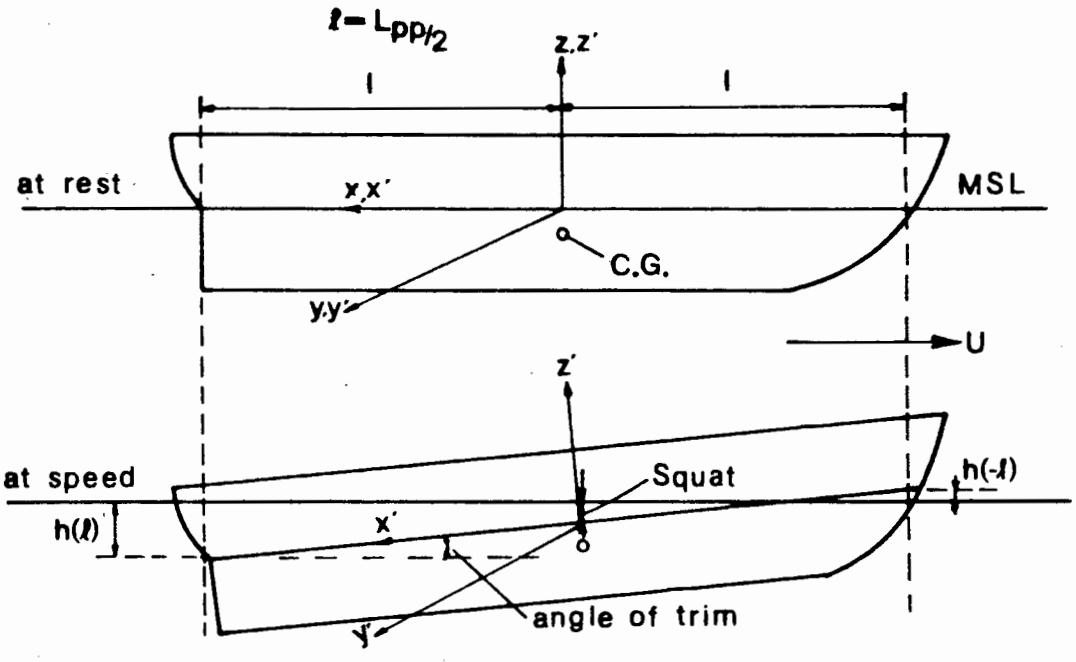

Fig. 3.2: Ship Squat and Trim

3.3 Fluids in motion

3.3.1 Gravity and viscosity effects

In fluid mechanics, flow in a perfect or non viscous fluid is called potential flow. This makes it possible to mathematically resolve flow situations around a body as the tangential stresses are assumed zero. When viscous effects are included in the momentum and energy equations, a set of complex differentiable equations result. There are two properties of real fluid flow that need to be taken into account since their combined result is to cause surface friction:

(1) The absence of all measurable slip at a solid boundary in contact with a moving fluid.

(2) Viscosity.

There can therefore be no boundary to a real fluid that does not affect the flow conditions in its proximity.

Fluid flows in all situations are thus characterised by the interactions that take place between the flow and its boundaries and the opposing forces within the fluid itself.

3.3.2 Laws of dimensional similarity and comparison

In order to compare models to prototypes with confidence, the connecting equations for each form of resistance must be understood. If a resistance is to be evaluated it is important that the various terms be arranged so as to result in an answer in terms of force i.e. MLT^{-2}. The law of dimensional similarity sets out to define variables or groups of variables that may be grouped together in such a manner as to facilitate the determination of a desired relationship. This implies an understanding of the phenomena involved and the connecting relationships in terms of the fundamental units of mass, time and length (Table 3.2).

Table 3.2: Influencing dimensional factors

1.	Length as determining size (L)	L
2.	Velocity as determining speed (U)	LT^{-1}
3.	Mass density as determining inertia (ρ)	ML^{-3}
4.	Viscosity as influencing frictional drag (μ)	$ML^{-1}T^{-1}$
5.	Gravity as affecting weight and potential energy (g)	LT^{-2} LT^{-2}
6.	Shape factors affecting form (r_1, r_2)	non dimensional
7.	Roughness of surface, affecting frictional drag (r_o)	non dimensional

Total Resistance can be written as a function of each of these factors.

$$R = \emptyset(L.U.\rho.\mu.g.r_1.r_2.r_o)$$

The function may usually be represented by a power series and the non dimensional shape factors can be represented by a factor K thus

$$R = \Sigma K L^a U^b \rho^c \mu^d g^e \qquad a, b, c, d, e \text{ unknown indices.}$$

Hence solving for the indices we get as a result (Barnaby, 1969)

$$R = \Sigma K L^2 U^2 \rho \left\{ \left(\frac{\nu}{LU}\right); \left(\frac{Lg}{U^2}\right) \right\} \qquad \text{(Eq 3.3)}$$

Ignoring gravity, we get

$$\text{frictional resistance} = L^2 U^2 \rho \emptyset\left(\frac{\nu}{LU}\right) \qquad \text{(Eq 3.4)}$$

Ignoring viscosity results as

$$\text{non frictional resistance} = L^2 U^2 \rho \emptyset\left(\frac{Lg}{U^2}\right) \qquad \text{(Eq 3.5)}$$

where $\emptyset$ = unknown function

These fundamental equations form the basis of the dimensional analysis procedures used in ship resistance applications and are fully discussed in Section 3.4.1. The interactions within the

fluid can be represented by a series of non dimensional parameters which allow the physical interpretation of the fluid problem. The parameters used for dynamic ship drag applications fall broadly into two categories:

(1) Parameters used for the scaling of any real flow;

(2) Parameters which scale free surface flows.

3.3.2.1 Boundary geometry

For valid scale model testing, the model used has to be geometrically similar to the prototype, i.e. the ratio of any boundary length on the prototype to the corresponding boundary length on the model is the same throughout. The ships are then said to be geometrically scaled models of one another.

3.3.2.2 Reynolds number

The ratio of the inertial forces to the viscous forces acting on a water element is called the Reynolds Number.

$$\text{Reynolds number, } R_n = \frac{UL}{\nu}$$

For the same fluid and temperature (the kinematic viscosity is temperature dependent) the speed of the model to speed of the prototype must be of the the length of the prototype to the length of the model.

$$\frac{U_m}{U_p} = \frac{L_p}{Lm_s} \qquad \begin{matrix} m = \text{model} \\ p = \text{prototype} \end{matrix}$$

For $\beta = L_p/Lm$ then $Um = \beta . Up$ (These speeds are the corresponding speeds for viscous forces.

The Reynolds number also scales the transitional phase between laminary and turbulent flow. Beyond a critical value of Rn, laminar

flow becomes turbulent, a feature recognised by a British engineer Osborne Reynolds (1842 - 1912) after whom the parameter is named.

3.3.2.3 **Froude number**

The Froude Number represents the ratio of the inertial forces to the gravitational forces acting on the fluid element.

$$\text{Froude Number, } F_n = \frac{U}{\sqrt{gL}}$$

The Froude number is independent of viscosity and so applies to inviscid flow analysis. For similarity between model and prototype and taking 'g' and constant, we note:

$$\frac{U_p}{\sqrt{L_p}} = \frac{U_m}{\sqrt{L_m}}$$

$$U_m = \frac{\sqrt{L_m}}{\sqrt{L_p}} \cdot U_p$$

$$= \frac{U_p}{\sqrt{\alpha}}$$

i.e. the model speed must be the prototype speed divided by the root of the linear scale.

These speeds are the corresponding speeds for wave making resistance and are markedly different from the frictional resistance speeds. A comparison of the applicable scaling parameters is given in Table 3.3. For ship applications the length used for Reynolds and Froude number scaling is the wetted waterline length, or LWL.

Table 3.3: Non-dimensional scaling parameters (Blevins, 1984)

Parameter name	Definition	Physical Significance	Application
Boundary Geometry	aspect ratio relative roughness, fineness ratio etc.	scale	general fluid dynamics
Reynolds	$R_n = \frac{U.L}{\nu}$	$\frac{\text{Inertial force}}{\text{Viscous force}}$	viscous fluid dynamic analysis
Froude Number	$F_n = \frac{U}{\sqrt{gl}}$	$\frac{\text{Inertial force}}{\text{Gravity force}}$	free surface fluid dynamics

3.4 Ship resistance

As a ship proceeds along a constant course in a calm see it experiences a retarding force against the fluid flow of the ocean. To overcome this force, the ship must move at some expense of energy. This energy is partly visible in the train of waves following the ship and is also due to the viscosity if the water. Any body moving through a viscous fluid experiences a resistance partly due to the integration of the tangentially acting shear stresses on the body and partly resulting from the integration of the normal stress components over the body affected by the boundary layer growth and separation. Thus the force exerted on a body can be expressed as:

$$F = \int_S \tau \hat{s} dA + \int_S p \hat{n} dA \qquad \text{(Eq 3.6)}$$

i.e. the sum of the tangential shear stress, τ and the normal pressure, p acting over the surface S and resolved along the body axis.

The tangential shear stress results in what is termed skin friction drag because it is resultant of the viscous shear forces acting on

the body. The integration of the normal pressures is called the form or pressure drag.

Although these two components of resistance seem to be mutually exclusive, there are regions of overlap and intersection. The frictional resistance will depend on the wave profile along the hull, and the wave pattern will depend to a degree on the effect of the ship boundary layer and wake, thus the effects of gravity and viscosity interact.

To solve this problem it is convenient to separate the resistance into components of gravity and frictional resistance and make certain assumptions (Section 3.4.1). The need to separate resistance into components is associated with the following facts:

(i) Skin friction is the greater part of resistance and varies from 50% of the total for high speed ships to as much as 90% for average cargo ships (Blevins, 1984).

(ii) For conventional hulls there is not much change in frictional resistance with hull redesign (Gillmer, 1975).

(iii) Resistance resulting from eddies and vortices can be kept to a minimum with sound design.

(iv) Optimum resistance designs are those that produce the smallest waves (i.e. minimum wave resistance).

It is therefore necessary to be able to determine the wave making resistance independently of skin friction resistance so as to minimise the residual resistance.

3.4.1 Froudes method

In Section 3.3.2 it was shown that $R = F(L,U,\rho,\nu,g)$ and that the total resistance is a function of two variables, Reynolds number and Froude number.

$$C_t = \frac{R}{1/2\ U^2L^2} = f\left(\frac{U}{\sqrt{Lg}}, \frac{UL}{\nu}\right) = f(F_n, R_n) \qquad \text{(Eg 3.7)}$$

C_t can be represented graphically by a characteristic surface over the F_n, R_n plane for a particular ship's hull. This plane is defined by:

$$R_n = \frac{L^{3/2}\ g^{1/2}}{\nu}.Fn = \Delta^{3/2}F_n \qquad \text{(Eq 3.8)}$$

$$\Delta = \frac{Lg^{1/3}}{\nu^{2/3}}$$

The value of Δ for a given prototype ship is effectively a constant. For a particular model ship, Δ can only be varied by changing the kinematic viscosity and the range of viscosity achievable in practice by using different fluids is narrow. The zone in the F_n-R_n plane represented by p is different from the zone represented by m and therefore C_T, which is a function of a point in the F_n-R_n plane, will differ in the model and the prototype.

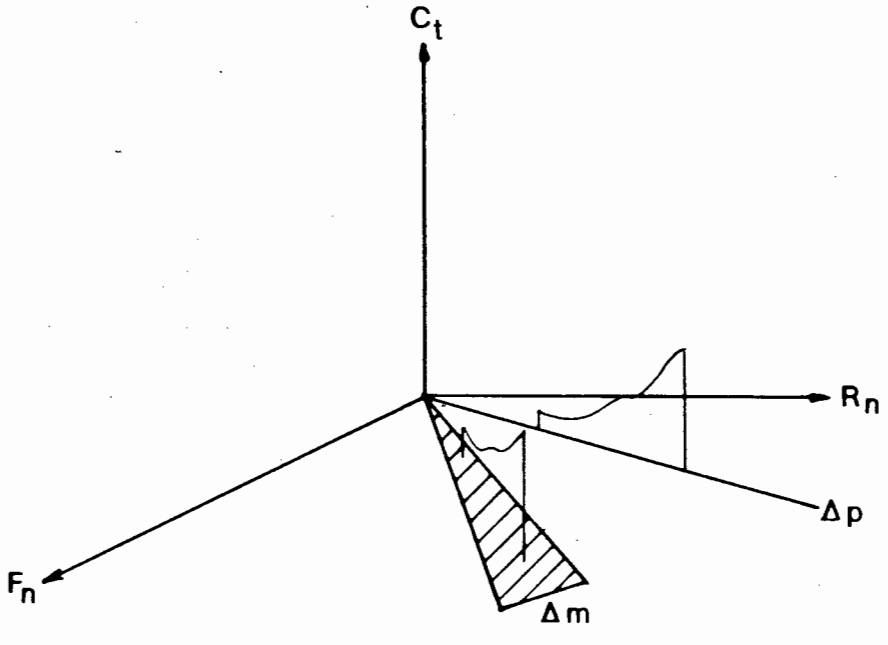

Fig. 3.3: Graphical representation of $C_t = f(F_n.R_n)$

This incompatibility of the curves of C_t was first recognised and understood by Froude, who found that the wave patterns of similar forms of different scales were identical if $UL^{-1/2}$ was kept constant. This leads to the division of resistance as follows, called Froudes Hypothesis.

$$C_t(F_n,R_n) = C_r(F_n) + C_f(R_n) \qquad \text{(Eq 3.9)}$$

Hence the models are tested at the same Froude numbers and the total resistance coefficient of the prototype can be found from

$$C_{tp} = C_{tm} - C_{fm} + C_{fp} \qquad \text{(Eq 3.10)}$$

Separating C_t into two parts by the integration over the wetted surface areas of the stress vectors in the normal and tangential directions (Eq 3.6) gives:

$$C_t(F_n,R_n) = C_{norm}(F_n,R_n) + C_{tang}(F_n,R_n) \qquad \text{(Eq 3.11)}$$

Assuming that the tangential force is determined by the viscosity alone and the normal force determined by the effect of gravity as a result of the waves (see Fig. 3.4) then:

$$C_{norm} = C_{norm}(F_n)$$
$$C_{tang} = C_{tang}(R_n)$$

Replacing the tangential force over the hull surface by the tangential force of a flat plate of the same waterline length and wetted surface area, the frictional resistance coefficient is then defined by:

$$C_f(R_n) = \frac{\text{(Flat Plate Resistance)}}{\frac{1}{2}\rho U^2 S} \qquad \text{(Eq 3.12)}$$

Therefore C_f is now independent of the hull form and the difference $C_t - C_f = C_r$ is a function of Froude number only. The term C_r is termed residuary resistance coefficient and contains wave resistance, form effects, eddy resistance and the effects of trim and sinkage.

3.4.1.1 Validity of Froudes assumptions

The weakness of the assumption is its acceptance that C_r is only a function of Froude number. Many phenomena could interfere with the subdivision of the components, for example:

(i) Reynolds number influence on the eddy resistance;
(ii) Shape effects on the skin friction;
(iii) Absence of a propeller in determining residual resistance;
(iv) Wave breaking resistance;
(v) Effect of the viscous flow in the boundary layer.

Frictional effects are confined to the boundary layer and the frictional wake. Outside of the boundary layer viscosity is negligible although the wave making affects the squat and trim and thus influences the extent of the surface of the boundary layer, in turn affecting the frictional resistance.

Despite these shortcomings in the division of the resistance components, Froudes method has been successfully utilised in all towing tanks.

3.4.1.2 Refinement of Froudes method

In order to redefine residual resistance, the coefficient of eddy resistance is estimated at (Gillmer, 1975),

$$C_e = a + bC_F \qquad \text{(Eq 3.14)}$$

Coefficients a and b are chosen such that at the lower Froude numbers, the curves of C_t and $C_f + a + bC_f$ are coincidental, assuming negligible wave resistance in these ranges. Using this C_e curve, the wave resistance coefficient is often referred to as $C_t - C_f - C_e$.

Another approach to of Froudes method is to define the viscous resistance as half the resistance of a double model tested at scaled Reynolds numbers in a deeply submerged towing channel or a wind tunnel, denoted $C_v(R_n)$.

The wakes of the single and double model do not always correspond at all Froude numbers due to the absence of a free surface and turbulent interchange across this surface, however C_v includes more of the viscosity effects than flat plate resistance coefficients, C_f.

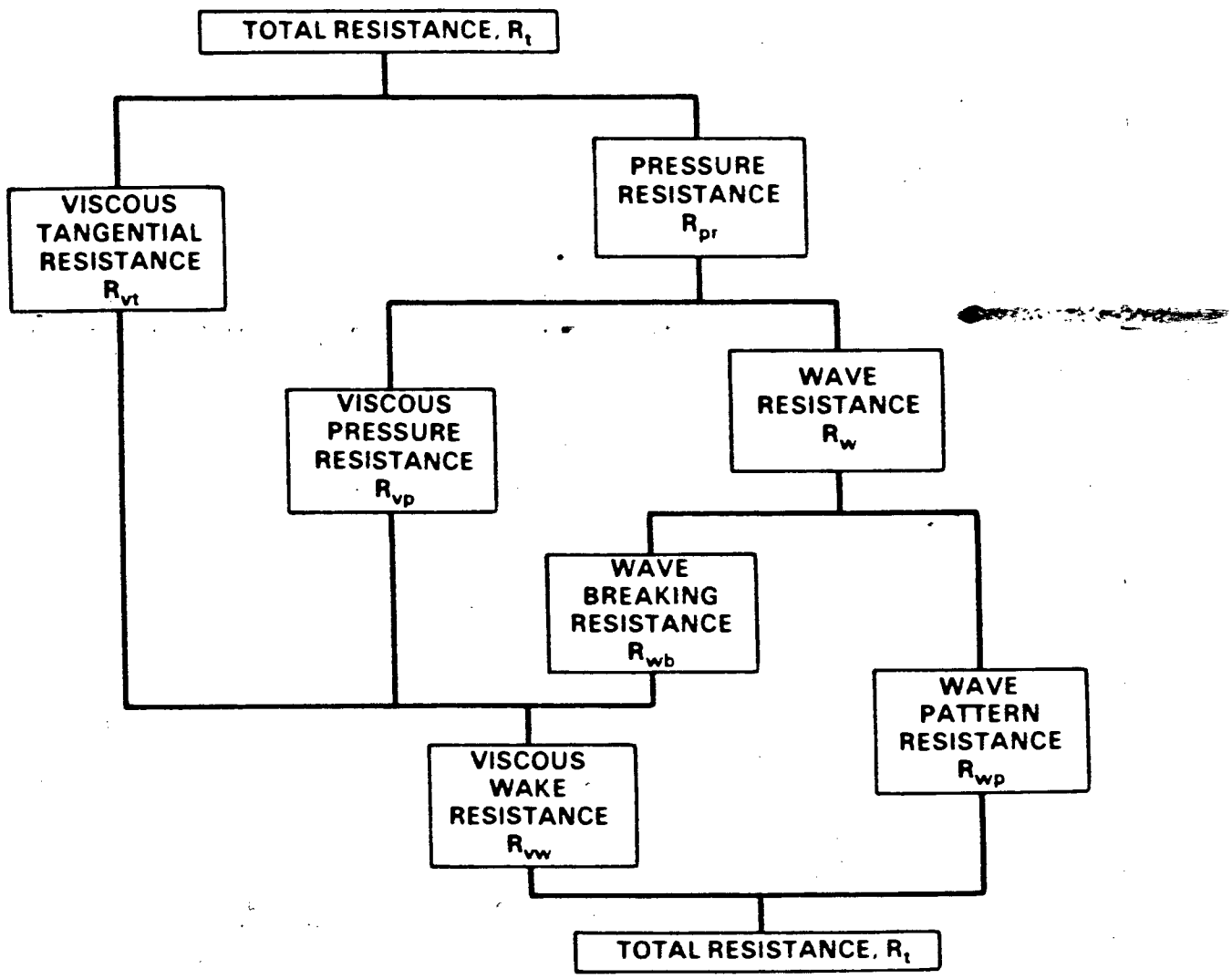

Fig. 3.4: Ship resistance components (Ship Wave Resistance Computations, Volume I, 1979)

3.4.2 Surface friction

3.4.2.1 Froudes method

According to Froude's hypothesis, it is necessary to find the variation of frictional resistance with speed and type of surface for a ship's hull. Froude conducted experiments using thin planks ranging from less than a metre to 15 m in length. Each was coated with different surface roughnesses and towed at varying speeds. The resistances were carefully measured and Froude expressed the result empirically as:

$$R = f.S.V^n \qquad \text{(Eq 3.14)}$$

The coefficient f and the index n were found to vary with both type and length of surface. Froude's results are as follows:

(i) The coefficient f decreases as length increases.

(ii) The index n is generally less than 2, typically 1,85 - 1,90, except for rough surfaces when it remains a constant 2.

(iii) The degree of roughness of a surface has a great influence on the magnitude of f.

Froude established Eq. 3.14, despite certain anomalies he recognised, and a set of suitable f coefficients was provided using n = 1,825 for a typically rough surface. The problem of surface friction was supposedly solved, and not until the recognition of the importance of Reynolds number were there any significant alterations.

3.4.2.2 Boundary layer

A boundary layer exists due to the effects of viscosity on a real fluid (Section 3.3.1). It is assumed that all measurable frictional resistance occurs within this region and it is therefore necessary to define its size, shape and extent.

At the surface of the solid boundary the fluid is at rest (no slip boundary condition), and the flow velocity increases from zero to nearly the free stream velocity in a thin layer adjacent to the surface of the solid. The boundary layer can be visualised as consisting of a large number of stream bands, each with increasing velocity from the surface to the outer extreme. Normal pressures are transmitted across the boundary layer, but the tangential stress does not exceed beyond the edge of the boundary layer. The fluid is thus sheared between the free stream and the solid surface, inducing skin friction.

The flow within the boundary layer can be completely laminar or mainly turbulent, being laminar up to a critical Reynolds number, then becoming transitional in nature and finally fully turbulent (Fig. 3.5). The thickness of the boundary layer is zero at the stagnation point and increases along the surface. The flow accelerates through to the midsection of the ship body and decelerates thereafter, thickening rapidly and separating from the hull surface to form a free shear layer in the wake.

A laminar film separates the hull surface from the turbulent portion of the boundary layer and is found to be of the order to 25×10^{-6} m. Indications are that about 50% of the variation in velocity occurs in this laminar film, resulting in a very high rate of shearing. Considerable changes of momentum take place within the turbulent region outside the laminar film and affect the remaining 50% of the velocity change.

The presence of the laminar film is the cause of many fouling problems and the increase in surface friction can be as much as 200% in tropical regions due to this cause (Barnaby, 1969). Owing to the stationary nature of the laminar film, it enables biological spores to attach themselves to the surface, even at high ship speeds. Because of the lowering of residual resistance, modern ships are dominated by frictional resistance and thus more susceptible to loss of speed due to fouling.

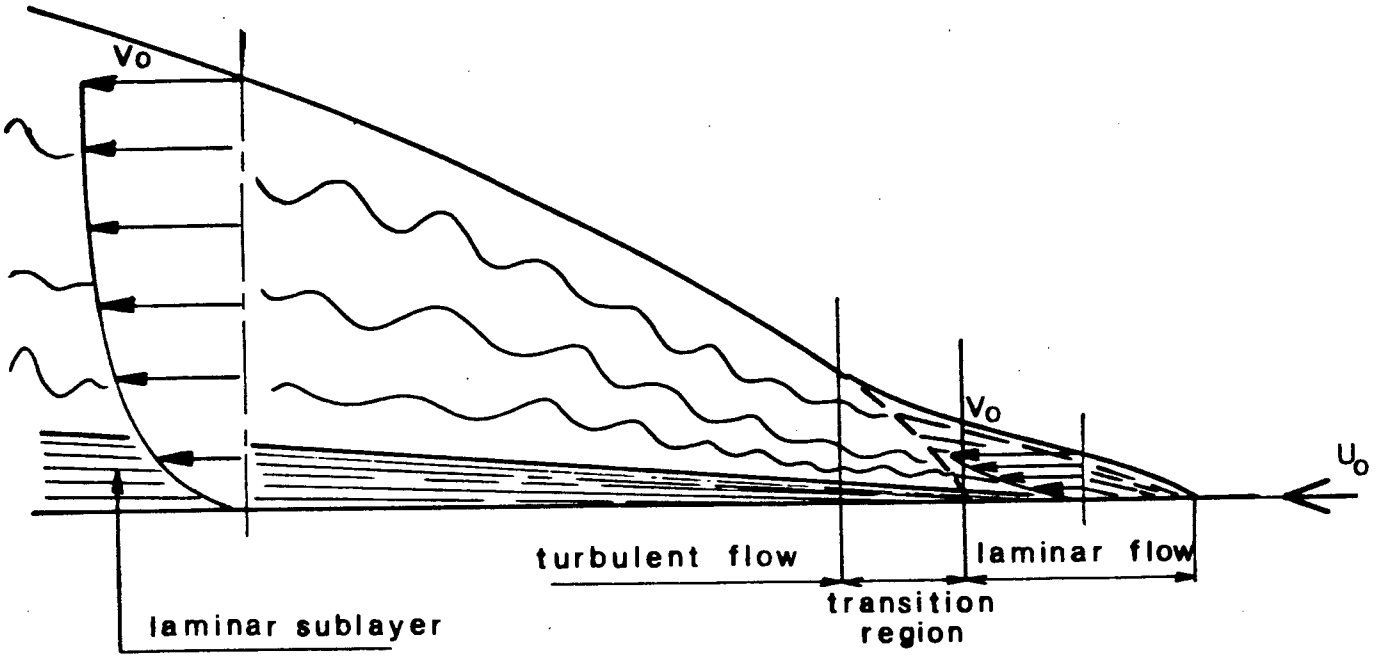

Fig. 3.5: Characteristic elements of the boundary layer

The exact calculation of the three dimensional boundary layer on a ship form has largely been restricted to double ship models (Landweber and Patel, 1979), although several attempts have been made to calculate boundary layer characteristics at non-zero Froude numbers, using approximations to the pressure distributions along the hull. In the case of the two dimensional boundary layer flow problem there exists a number of exact solutions (Blevins, 1984) for free stream flows.

3.4.2.3 Friction lines

The frictional forces that develop within the boundary layer lead to skin friction, the value of which is:

$$R_f = q \times A \times C_f \qquad \text{(Eq 3.15)}$$

where q = the dynamic pressure = $^1/_2 \rho U^2$

A = solid area in contact with fluid

C_f = coefficient of friction.

The value of C_f can be either that associated with a point on the surface or the average value over the entire length, the latter being usually considered for ship application.

The value of C_f depends on a flow parameter (Reynolds number) and on any surface irregularities. Imperfections on the surface may cause shear stresses associated with increased turbulence in the boundary layer. The first expressions for C_f were presented by Prandtl and von Karman in about 1921, giving values for both laminar and turbulent flow.

$$C_f = \frac{1,327}{\sqrt{Re}} \quad \text{(laminar)} \qquad \text{(Eq 3.16)}$$

$$C_f = \frac{0,072}{\sqrt[5]{Re}} \quad \text{(turbulent)} \qquad \text{(Eq 3.17)}$$

Eq 3.17 holds for Reynolds numbers in the lower ranges, but at higher values, the C_f from this equation is too low, the exponential law for velocity distribution no longer being valid.

These initial equations were extended by Schoenherr on the basis of several friction experiments and the following formula was adopted by the A.T.T.C. (American Towing Tank Conference) in 1948 and its use was agreed as the alternative to Froude's method for determining skin friction (Eq. 3.14).

$$\frac{0,242}{\sqrt{C_f}} = \log (Rn.C_f) \qquad \text{(Eq 3.18)}$$

A modification of this line was that of Hughes, that no one curve could represent all shapes of ships, and that a factor be introduced to cover a band of lines representing several LWL/B ratios.

$$C_f' = C_f(1 + r) \qquad \text{(Eq 3.19)}$$

where r = an experimentally determined form factor.

The introduction of the form factor was similar to a method proposed by Dr Telfer using several geometrically similar models. The Telfer method involves determining the total resistance of a prototype directly from model measurements, ignoring the breakdown into frictional and residual components. This method is illustrated in Fig. 3.6. The total resistance coefficients for each of three models (geosims) are plotted. Lines drawn through the same Froude numbers are parallel to the friction line. The friction line is plotted using a linear scale for the inverse cube root of R_n along the x axis for either the Schoenherr or Telfer formulations referred to in Eqs 3.18 and 3.20.

$$C_f = 0{,}0012 + 0{,}34\ (Rn)^{-1/3} \qquad \text{(Eq 3.20)}$$

The lines of varying Froude numbers are cross connected to the resistance curves of the geosims. The intention was to define experimentally the extrapolation slope for the three dimensional ship form, but there are several drawbacks in practice (Lackenby, 1961). When determining C_T for the set of geosims, problems arise due to effects of towing tank wall interference with the larger models (known as blockage), and the elimination of laminar flow on smaller models.

Although it has been conceded that friction coefficients must be based on Reynolds number, a general formula was agreed upon at the 1957 Eighth towing tank conference, known as the "ITTC 1957 model ship correlation line", the equation beineg given below.

$$C_f = \frac{0{,}075}{(\log R_n - 2)^2} \qquad \text{(Eq 3.21)}$$

This line is based upon the original Schoenherr values, but is steeper in the model range and almost identical for ship prototype values. The formulations of Telfer, Prandtl, Hughes, etc. are all reasonably close in the normal operating range for full scale ships and are best represented singly by Eq. 3.21. These formulae all relate to ideally smooth surfaces and the effect of roughness is discussed in the following section.

figure of C_k = 0,00031 was determined for the "Lucy Ashton" using red oxide paint. Average figures for C_k appear to be from 0,0003 to 0,0004 for general paints, but additions have to be made for roughnesses associated with the manufacturing process, e.g. welds, seams, rivets, etc.

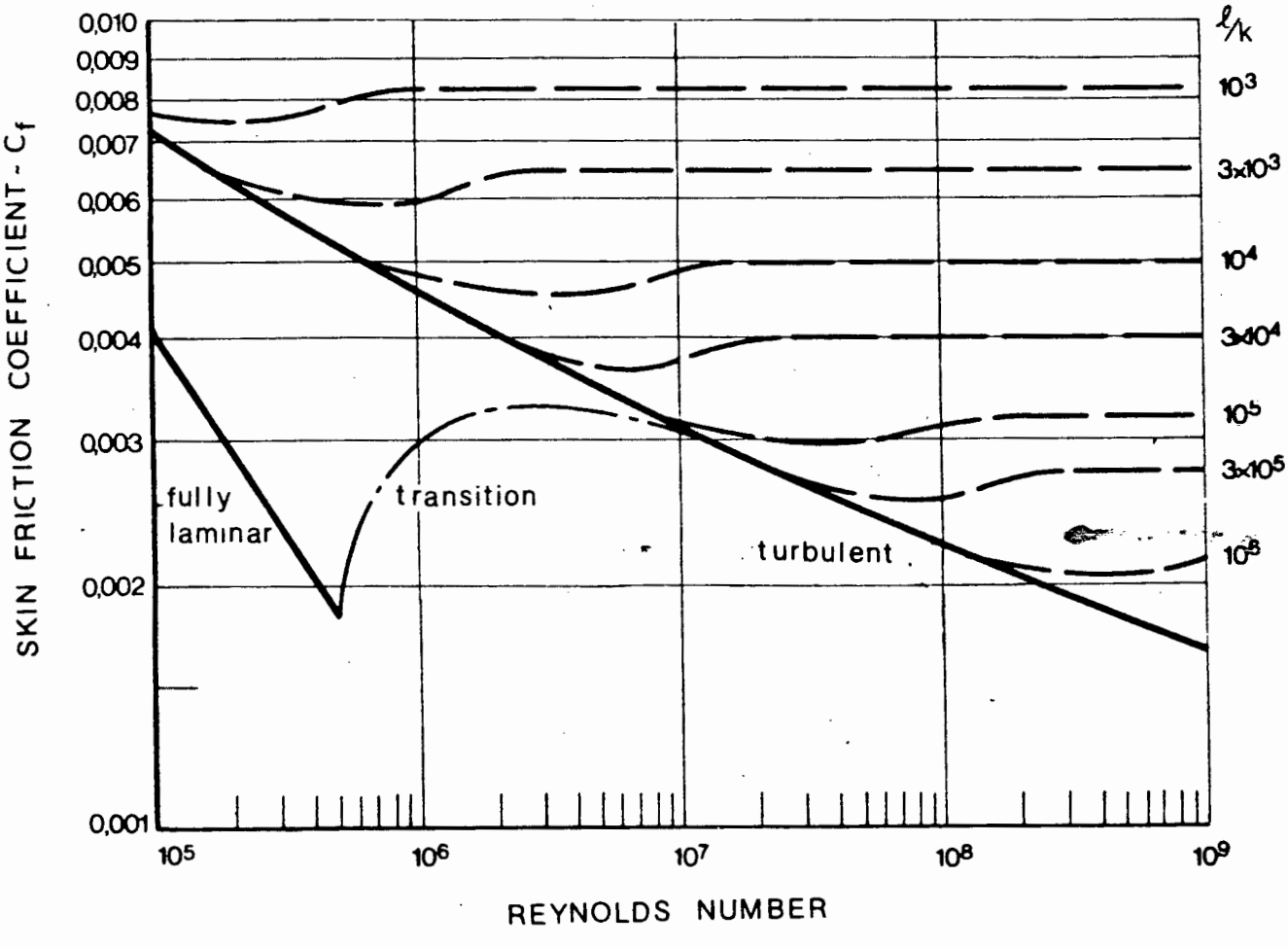

Fig. 3.7: Curves of skin friction coefficient and Reynolds number for surfaces with variable 1 ℓ/k ratio, ℓ being the length of the surface and k the height of the roughness.

The built in roughness generally remains constant, decreases slightly due to corrosion. The paint surface contribution varies according to the extent of fouling and barnacle growth, as confirmed by Lackenby (1961). So long as the roughness does not protrude through the thin laminar sub-layer film at high Rn or through the laminar boundary at low R_n values, the surface remains essentially hydraulically smooth and there is no increase in resistance.

3.4.2.5 Separation, ventilation and cavitation

Considering Fig. 3.8, there is a pressure distribution within the fluid as the streamlines divert around the body. If the free stream static pressure is p (point 1), deviations of local pressure from p are given the symbol p and may be either positive or negative in different zones, associated with accelerations or retardations, as shown. The highest positive pressure occurs at the nose of the body, the minimum pressure occurs some distance downstream from the nose (point 2).

Fluid flow remains attached to the solid surface provided the adverse pressure gradient near the rear of the body is not too steep. This latter effect tends to occur where there is an abrupt change of hull form, when the boundary layer becomes detached at a point known as the point of separation (point 3). As speed increases, the location of the separation point tends to move further upstream. Reversal and eddies occur within the turbulent separation wake, as in the velocity profiles of Fig. 3.8. There will be an increase of resistance due to the wake, but the coefficient will be fairly constant once the wake is established. However, the occurrence of separation and the point of separation depend on the pressure distribution of the aft surface of the body.

Considering a surface model where there is an air to water interface, the local pressure at any point is influenced by the pressure deviation associated with the velocity distribution and also the submergence of the point in question. At points of low pressure air may be sucked into the wake region.

In certain instances the pressure along the hull can be so low that air bubbles are attracted down from the water surface, giving rise to ventilation along the stern separation boundaries.

Where the draught of a ship is very deep, such that ventilation cannot occur, the pressures at isolated point on the hull can fall to nearly absolute zero and be less than that of the vapour pressure,

then vapour bubbles can form in the water, and implode rapidly as they move into higher pressure regions. This is called cavitation and the rapid fluctuations in local pressure can cause severe corrosion and local pitting of the surface.

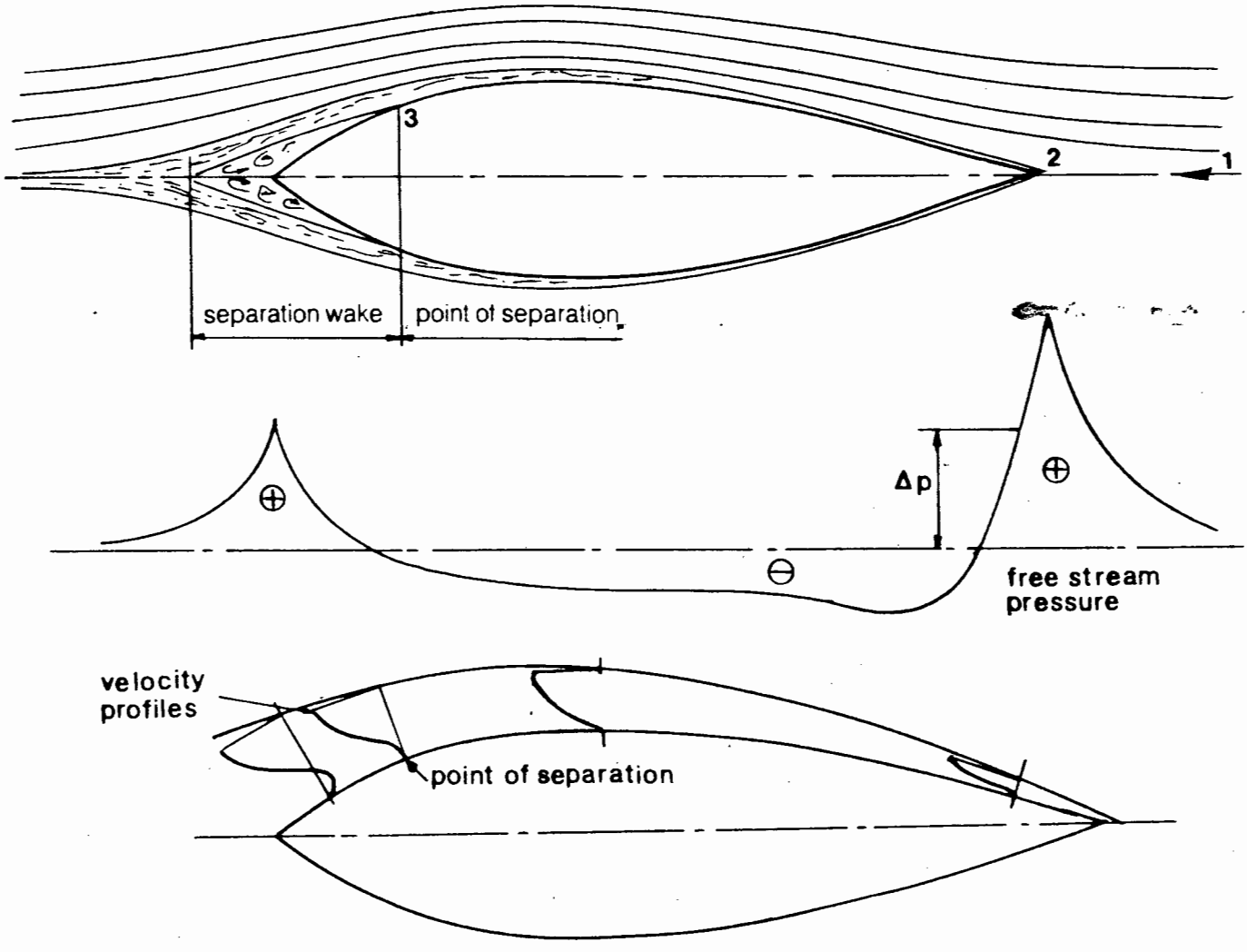

Fig. 3.8 Separation of the boundary layer around a submerged body

3.4.3 Wave making resistance

Considering flow around body shape with symmetrical fore and aft sections, the water surface will respond to the pressure distributions around the hull. The pressure distribution is symmetrical about the midsection of the hull, reaching a peak at the bow and stern and dropping below the free stream pressure at the midsection, as illustrated in Fig. 3.9.

A surface fluid particle responding to this symmetrical pressure distribution will reach a peak elevation just aft of the bow, where the pressure is decreasing. This is due to the presence of a vertical dynamic pressure gradient caused by the vertical accelerations of the particles near the surface. Because of this pressure gradient the positions of the surface particles do not correspond exactly to the pressure distribution around the hull. These inertial differences set up wave motions at bow and stern and along the mid body of the ship.

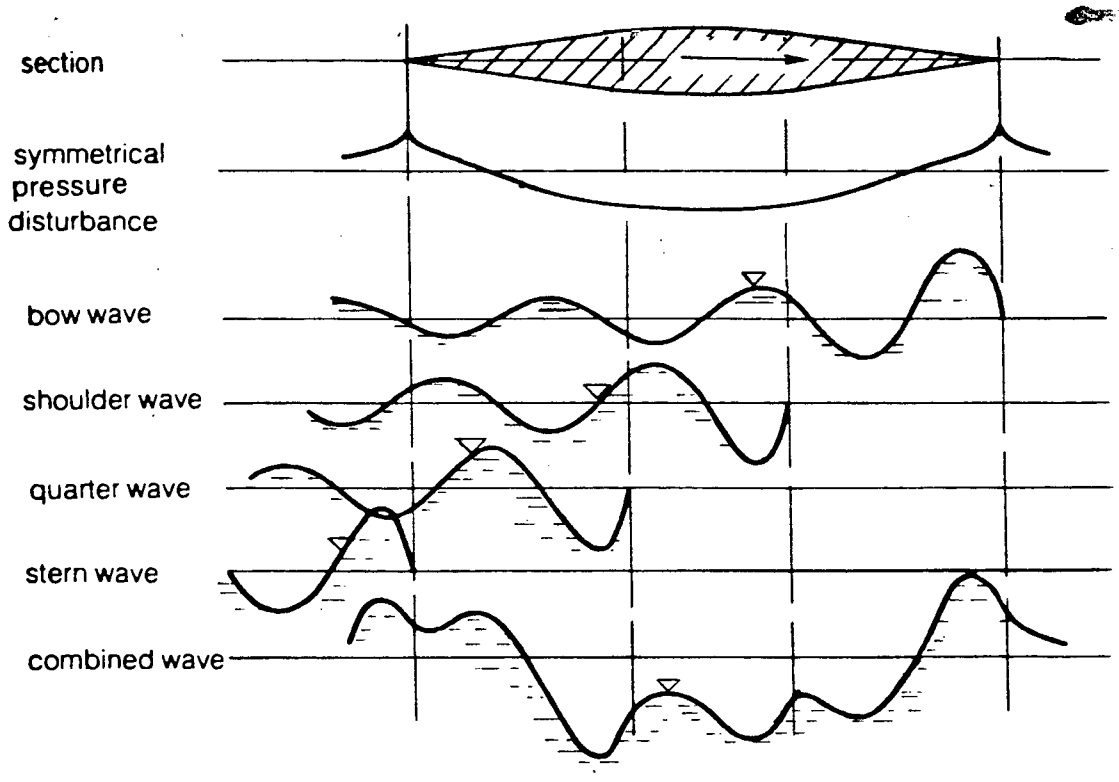

Fig. 3.9 Breakdown of the wave systems for a body of symmetrical fore and aft section and parallel mid body

The resultant wave system set up by these inertial differences is the cause of the wave making component of resistance. To understand the nature of wave making resistance it is necessary to gain an insight into the nature of the generated waves and the resultant wave pattern.

3.4.3.1 Elements of wave mechanics

Most of the developments in the theoretical analysis and prediction of ship generated waves is based upon the linearized theory of free monochromatic gravity waves. The following assumptions are made in the linear wave theory:

(i) Wave amplitude is small compared with wave length and water depth.
(ii) Water is homogeneous and incompressible.
(iii) Surface tension fores are negligible.
(iv) Flow is irrotational - shear stresses are negligible at interfaces of solid/water or air/water.
(v) Pressure at air interface remains constant.

As particle velocity is related to wave amplitude, and wave celerity is related to water depth and wave length, then from (i) above, the particle velocities are small compared with the wave celerity. The definition of a two-dimensional wave is shown in Fig. 3.10.

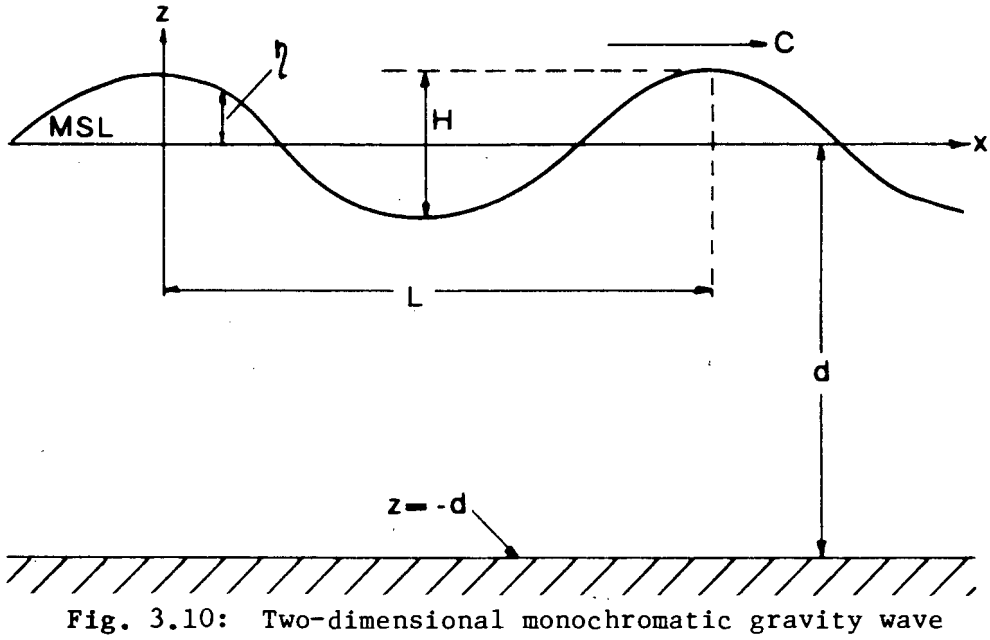

Fig. 3.10: Two-dimensional monochromatic gravity wave

The wave celerity (velocity) is related to wavelength and period by Eq 3.22.

$$C = \frac{L}{T} \qquad \text{(Eq 3.22)}$$

The surface elevation is given by:

$$\eta = \frac{H}{2} \cos (kx - \sigma t) \qquad \text{(Eq 3.23)}$$

where t = time elapsed as wave passes an observer at station x

$k = \frac{2\pi}{L}$ the wave number

$\sigma = \frac{2\pi}{T}$ the wave angular frequency

Hence for the region $-d \leq z \leq \eta$ and $-\infty \leq x \leq \infty$ a solution is needed for the Laplace equation:

$$\frac{\partial^2 \phi}{\partial x^2} + \frac{\partial^2 \phi}{\partial^2 z} = 0 \qquad \text{(Eq 3.24)}$$

where ϕ = velocity potential

Applying the appropriate boundary conditions, a solution results (Stoker, 1957) for $d/L \geq 0{,}5$, a deep water wave, as follows:

$$C_o = \left(\frac{gL_o}{2\pi}\right)^{1/2} \qquad \text{(Eq 3.25)}$$

$$L_o = \frac{gT^2}{2\pi} \qquad \text{(Eq 3.26)}$$

and therefore

$$C_o = \frac{gT}{2\pi} \qquad \text{(Eq 3.27)}$$

Wavelength and celerity depend only upon the wave period. When $d/L \leq 0{,}5$ the wave particle orbital motion reaches the seabed and the celerity and wave length both decrease as it shallows, the period remaining constant.

When $d/L \leq 0{,}5$ (Stoker, 1957) we get

$$C = \sqrt{gd} = \frac{L}{T} \qquad \text{(Eq 3.28)}$$

The water surface profile varies from sinusoidal to roughly trochoidal as illustrated in Fig. 3.11, and the particle orbitals become elliptic.

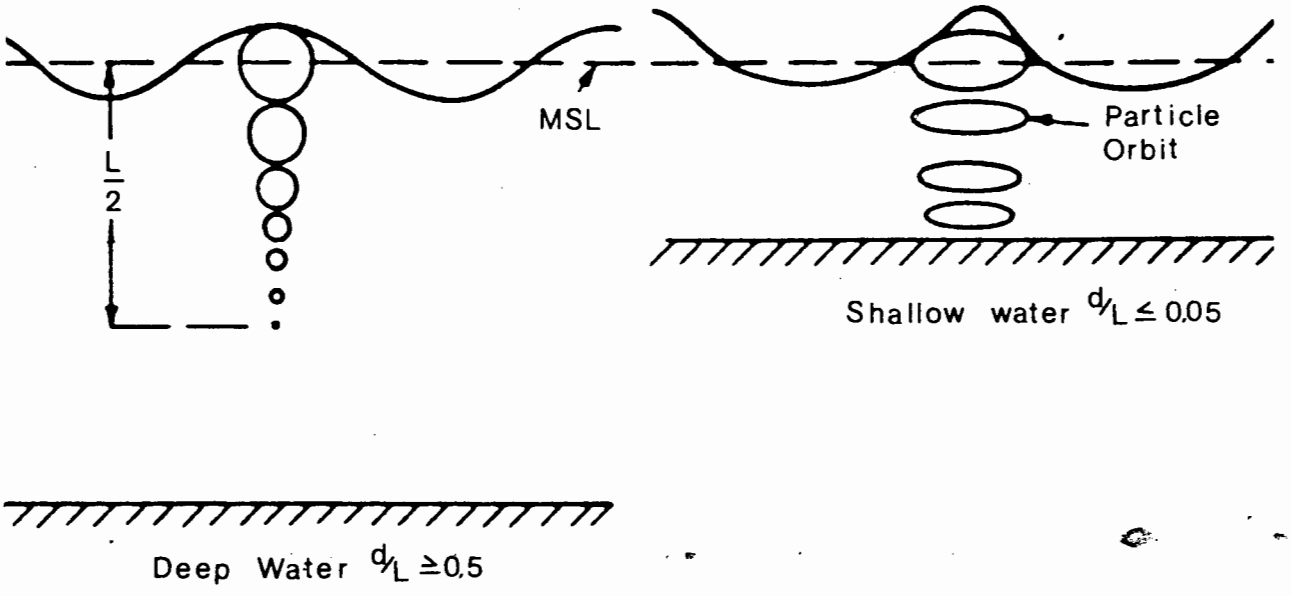

Fig. 3.11: Wave surface profiles and particle orbit geometries

The motion of a wave through water that was previously at rest results in an increase of energy in the water. Firstly, there is an increase of potential energy due to the lifting of the centre of gravity of the water mass and secondly, an increase of kinetic energy due to the acquired velocities of the water particles. The average energy over one wave length and for a unit crest width can be evaluated by integrating both the potential and kinetic energies of an element of water. This yields (Kilner, 1984) for the linearized case)

$$E = \frac{\rho g H^2 L}{8} \quad \text{joules per metre crest length} \qquad \text{(Eq 3.30)}$$

the energy being equally divided between potential and kinetic energy.

For a wave of containing n wavelengths the energy per unit crest is nE.

If the wave profile is not a regular wave, but rather the superposition of several sinusoidal waves, integration of the wave elevations is necessary to find the resulting wave energy.

It can be shown for the linearized case that for n.wavelengths,

$$n\left(w\,\frac{H^2L}{8}\right) = w\int_o^{nL}\eta^2 dl \qquad \text{(Eq 3.31)}$$

Assuming $\eta = a\cos kx$ then $L = \frac{2\pi}{k}$ and $H = 2a$

$$E = K\int_o^{nL} a^2\cos^2(kx)dx$$

$$E = Ka^2\left[\frac{x}{2} + \frac{\sin(2kx)}{4k}\right]_o^{\frac{2\pi.n}{k}}$$

$$E = Ka^2\left[\frac{n\pi}{k} + \frac{\sin(4\pi n)}{4k}\right]$$

$$E = \frac{Ka^2n\pi}{k} \qquad \sin(n\pi) = 0 \quad n = 0, 1, 2, 3 \ldots.$$

by substituting $a = \frac{H}{2}$ and $K = \frac{2\pi}{L}$

$$E = K.n.\frac{H^2L}{8} = \frac{WnH^2L}{8} \text{ as in (Eq 3.31)}$$

This form of the integral has no physical representation other than the summation of the squared surface elevations, but can be used as a useful algorithm to numerically calculate the energy along a surface crest profile of irregular elevations.

3.4.3.2 Deep water wave crest pattern

In 1887 Lord Kelvin proposed a theory to describe the wave crest pattern and amplitude for the wave system generated by a moving pressure point over a deep, undisturbed, inviscid fluid. The system

is illustrated in Fig. 3.12, showing two sets of oblique and diverging waves that move forward and outwards from the disturbance and one set of transverse waves moving in the direction of the disturbance.

The intersection of the tangents of the two wave disturbances intersect at an angle of 54°44' with the sailing line, the cusps forming an angle, α, of 19°28' with the sailing line.

The wave system is stationary with respect to the disturbance, the waves having a phase velocity of

$$C = U \cos\theta ; C_{phase} \qquad \text{(Eq 3.32)}$$

where U is the constant disturbance velocity (ship speed) and θ is the angle between the sailing line and the direction of advance of the wave.

Thus combining Eq 3.25 and Eq 3.32, the wavelength, L, of the transverse wave system is given by

$$L = \frac{2\pi U^2 \cos^2\theta}{g} \qquad \text{(Eq 3.33)}$$

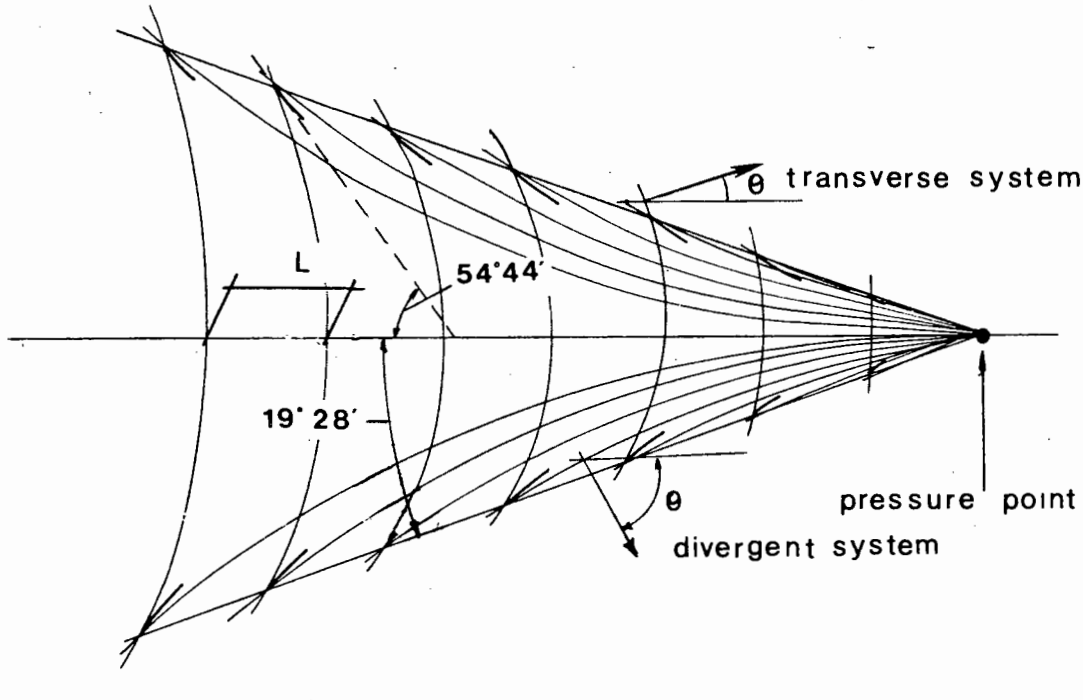

Fig. 3.12: Wave crest pattern generated by a moving pressure point in deep water

Along the sailing line, the transverse waves have the same velocity as the ship, so the wavelength is given by Eq. 3.25 or Eq. 3.33 for $\theta = 0°$. Away from the sailing, at increasing θ, the transverse waves curve in a convex manner, as in Fig. 3.13, the wave-length varying as in Eq. 3.33. The wave pattern is a superposition of plane waves travelling in all directions between $0° \leq \theta \leq 90°$. Between $\theta = 0°$ to 35°16' the waves form the transverse system, for θ = 35°16' to 90° the waves form the diverging wave system.

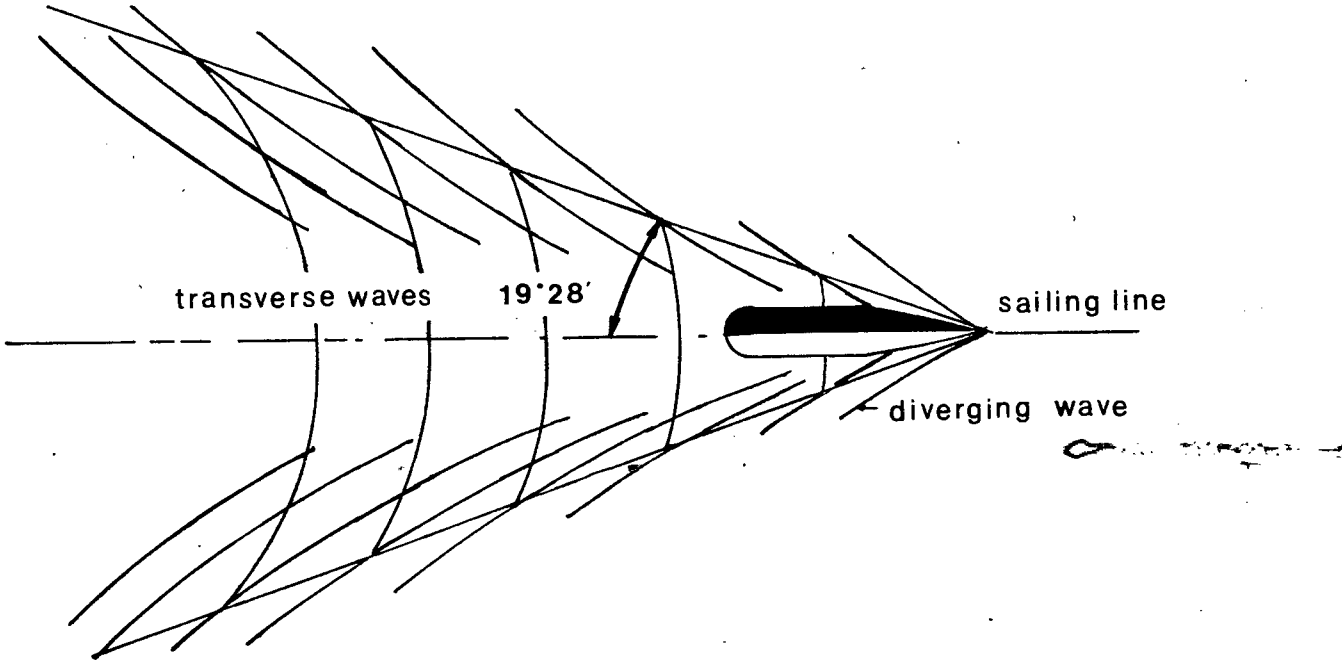

Fig. 3.13: Deep water ship wave crest pattern

The wave patterns can be calculated using a graphical construction (Stoker, 1957) to yield the directions of the curves of constant phase. Stoker gives procedures for determining both the wave patterns generated by a ship in a straight or circular course.

The diverging wave system remains fixed to the ship, while each of the individual wave phases move in a system oblique to the sailing line. This is due to the transfer of energy throughout the wave group. Relative to the ship there is a rearward energy transfer from each wave to the wave behind as the waves move forward and outward. Due to the regular formation of the waves, each wave grows at its

inward end and diminishes at the outward end, resulting in a motion in the direction of the ship. The ship adds energy continually to the inward end of the waves. Diffraction of the waves causes an increase in the crest lengths of each of the successive diverging waves.

3.4.3.3 Shallow water wave crest pattern

As a ship leaves deep water, the generated waves begin to feel the effects of the seabed. Shallow wave conditions result as the velocity approaches Eq. 3.28, and then the wave group velocity approaches the phase velocity ($C_G \rightarrow C$). The wave system now becomes dependent on depth.

As the depth decreases, the diverging wave crests rotate to a position perpendicular to the scaling line, increasing the cusp locus angle as in Fig. 3.14 to 90° for a depth Froude number of 1. The transverse and diverging waves form a single large wave travelling at the same speed as the disturbance. A small amplitude wave travelling in water depth, d, cannot have a velocity greater than the value given by Eq. 3.28, i.e. $(gd)^{\frac{1}{2}}$. Therefore at high ship speeds, the wave system contains no transverse waves, but a series of diverging waves radiating from the disturbance.

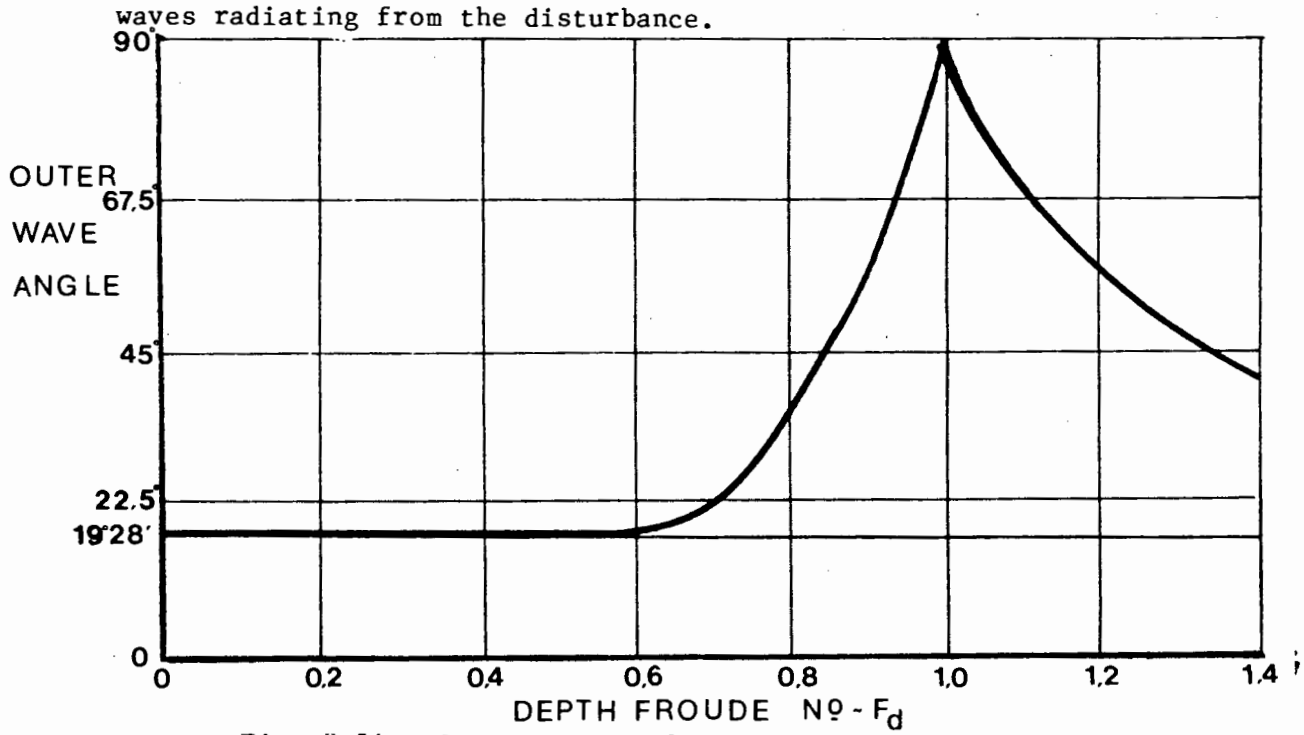

Fig. 3.14: Outer Wave Angle as a function of depth Froude number (Sorenson, 1967)

3.4.3.4 Analytical wave pattern prediction

Two main analytical approaches are used when calculating the wave pattern generated by a moving ship. In both, the following simplifying assumptions are made:

(i) The sinkage or trim of the ship is fixed in response to the waves and flow around the hull. Neglecting sinkage and trim at low speeds in deep water has no significant effect on the wave pattern, but at high speeds in shallow water the differences are quite important. These differences can be reduced by estimating beforehand the sinkage and trim and using these as datum for the calculations.

(ii) The flow velocity near the hull does not differ from the ship velocity, i.e. ignoring the velocity distribution in the boundary layer. Flow past the hull interacts with the wave pattern modifying the pressure variations.

(iii) The linearized wave theory is generally applied, except for Miyata (1985) who simulated non-linear ship waves. First order theory limits applications to lower speeds and thin ships (where small amplitude waves are generated), and deep water (where orbital velocities are negligible when compared with phase velocities).

(iv) The fluid is inviscid. Viscosity causes growth of the boundary layer and decay of waves. The boundary layer increases the effective ship dimensions, thus altering the pressure distributions over the hull. Empirical methods are generally employed to incorporate this growth of the boundary layer.

The two main analytical approaches are classified as direct or indirect. In the direct approach the wave pattern is calculated directly from the hull geometry. The method devised by Guilloton, employs a system of wedges to represent the hull form. Velocity potentials and wave profiles for each wedge are calculated. The wave system is then the summation of each of the wedge contributions.

Emerson (1967) gives calculation procedures employing this method to calculate the wave resistance from the integration of the calculated pressure distributions over the hull. This application was adapted for computerisation by Gadd (1973) and was used for several ship forms, yielding results that compared favourably with model testing.

The indirect approach utilises a continuous distribution of sources distributed on the hull centreline surface axis or a small number of finite sources placed at suitable locations on the hull to generate a wave system equivalent to that generated by the given hull form. Gadd (1975) distributed Rankine sources over a double model of a hull, represented by a series of regular spaced panels. The spacing of the panels is important in gaining a representative distribution of sources. If the generated waves are of a short wavelength compared with the hull (at lower Froude numbers), the horizontal spacing of the sources must be smaller at the bow and stern than at the midsection.

A further development of the indirect method is that of Miyata et al. (1985) and Miyata and Nishimura (1985). A finite difference solution to the Navier-Stokes equations is used to obtain the exact inviscid free surface. The method employs a fixed mesh system of equal spacing of pressure distributions and a further variable mesh spacing to improve accuracy. The generated waves around a Wigley hull are shown in Fig. 3.15. The solution is evaluated at time increments of the water flow accelerated from rest around a stationary ship until the steady state is reached when the free stream speed equals the desired ship speed.

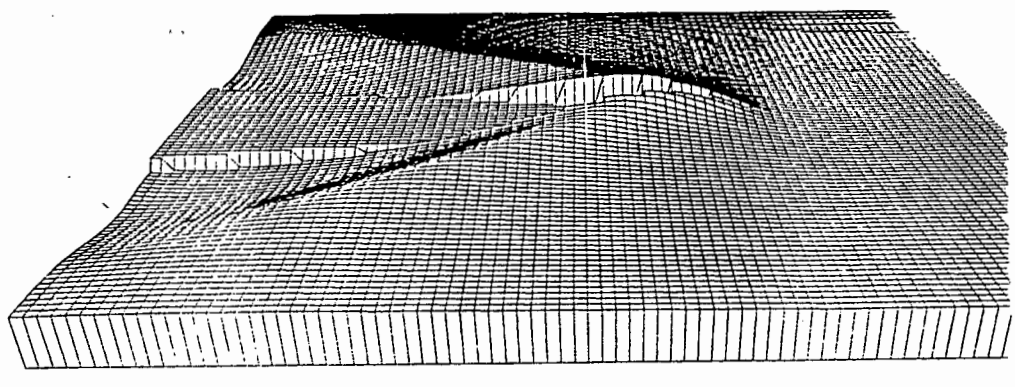

Fig. 3.15: Perspective view of waves around the forebody of a Wigley hull at Fn = 0,289 (Miyata, 1985).

3.4.3.5 Growth of wave making resistance

In section 3.4.3.2 it was shown that for the transverse waves the wavelengths along the ship sailing line were given by Eq. 3.33.

$$L = \frac{2\pi U^2}{g} \text{ for } \cos^2\theta = 0° \quad \text{i.e. } \theta = 90° \qquad \text{(Eq 3.34)}$$

The transverse waves are the greatest source of wave making resistance since they interact with the ship hull. The bow is the strongest source of ship waves (see Fig. 3.9). If a transverse wave is formed at the bow, its wavelength is given by Eq. 3.33 and the effective length of hull between bow wave crest and stern = 0,9 LWL (Blevins, 1984), then there will be a trough at the stern if the effective ship length is half the wavelength of the transverse waves, 0,9 LWL = L/2 or using Eq.3-34,

$$0{,}9\ \text{LWL} = \sqrt{\frac{2\pi U^2}{g}}\ .$$

thus in terms of Froude number

$$\frac{U}{\sqrt{g\,\text{LWL}}} = \left(\frac{0{,}9}{n\pi}\right)^{1/2}$$

F_n = 0,54; 0,31; 0,24; 0,20 ...
for n = 1, 3, 5, 7
trough at stern

Fn = 0,38; 0,27; 0,22; 0,19
for n = 2, 4, 6, 8
crest at stern

where n = number of wavelengths in effective hull length

Thus if the bow is on a crest and the stern in a trough, the ship is effectively climbing a self-produced hill of water, requiring additional energy to overcome this gradient. Therefore wave resistance is maximised at these speeds. Conversely minimum resistance occurs when crests occur at both stern and bow, the ship remaining effectively level. The effects of this juxtaposition of transverse waves is illustrated in Fig. 3.16, showing the wave resistance curve and the contributions of both the transverse and divergent waves.

in 1926, who conducted experiments with mathematically defined hulls so as to compare results with Michell's approximation. The work of Wigley, and later Havelock, who developed the moving pressure distribution theory, required the evaluation of Michell's quintuple integral manually at that time, a lengthy process. Even with the advent of the computer, the conclusions drawn from such early work still remain largely unchanged.

Havelock furthered Michell's approach using an alternative derivative based upon Green's functions, as opposed to the Fourier-integral theorem used by Michell. The methods of solution employed in the wave resistance problem are generally classified into two approaches:

(i) The Greens function approach involving integral equations.

(ii) The direct numerical solution of the field equation using the finite difference method or the finite element method.

The exact formulation of the flow for an inviscid fluid past a fixed ship is given in "Proceedings of the workshop on Ship Wave Resistance Computations" 1979, and for a ship free to trim and squat by Neuman (1976).

The Greens function approach can be classified into two types, depending on the function utilised. The first is Havelock's (or Kelvin source) used most often in the thin ship approximation and the Neumann-Kelvin formulation (Tsutsumi, T., 1979). The second is the Rankine source or fundamental source method used in the low speed theory. In both Neumann-Kelvin theory and low speed theory (Nakatake et al., 1979) the line integral along the ship hull surface and along the free surface is required. Various refinements occur in each of these methods as to the degree of approximation made in each mathematical formulation.

The recognition of the importance of wave breaking resistance on ships by Baba (1976), expecially those of full form, like tankers, needs to be fully developed to include adequate mathematical formu-

lations of breaking conditions. Wave breaking in certain full bodied forms can account for a large proportion of the wave resistance.

The means of predicting wave resistance analytically for a body geometry has led to the formulation of bodies of least resistance (Wehausen, 1973). Inui (1962) developed what he termed waveless forms, hulls of minimum-wave making resistance and developed the bulbous bow, a protrusion forward of the ship's stem. Its purpose is to create a wave system of the same amplitude to the bow and stern waves, but 180° out of phase so as to cause interference between the two systems and thus decrease the wave making due to the effect of superimposition.

4. EXPERIMENTAL METHODS OF DETERMINING SHIP RESISTANCE

4.1 Towing tanks

Towing tanks have evolved from the pioneer work of Froude to being highly sophisticated research facilities utilising extremely sensitive mechanical and electronic recording devices. Froude's tank measured 83 m by 11 m with a water depth of 3 m. It was the first tank to use a travelling carriage and carry accurate instrumentation. The lengths of towing tanks increased as the size of the models tested grew, the longer models yielding better results. One of the largest tanks or basins is in Carderock, Maryland, U.S.A., having a length of some 840 m and a width of 15 m. The depth is 7 m. Models of up to 10 m can be tested at speeds of 60 knots (30 m/s).

The large towing tanks utilise travelling platforms carrying sophisticated data-aquisition equipment and several observers (Fig. 4.1). A typical modern facility will include water treatment, water temperature control, air conditioning, underwater observation and photographic provisions. Carriage control will be from either on board or on-shore control panels and fully computerised. Modern channels are acoustically damped along side walls to reduce vibration and secondary effects due to reflected internal noise.

Most towing tanks have wave generators to be used when performing stability and sea trial tests with random or regular wave trains, an absorption beach being placed at one end to reduce wave reflection.

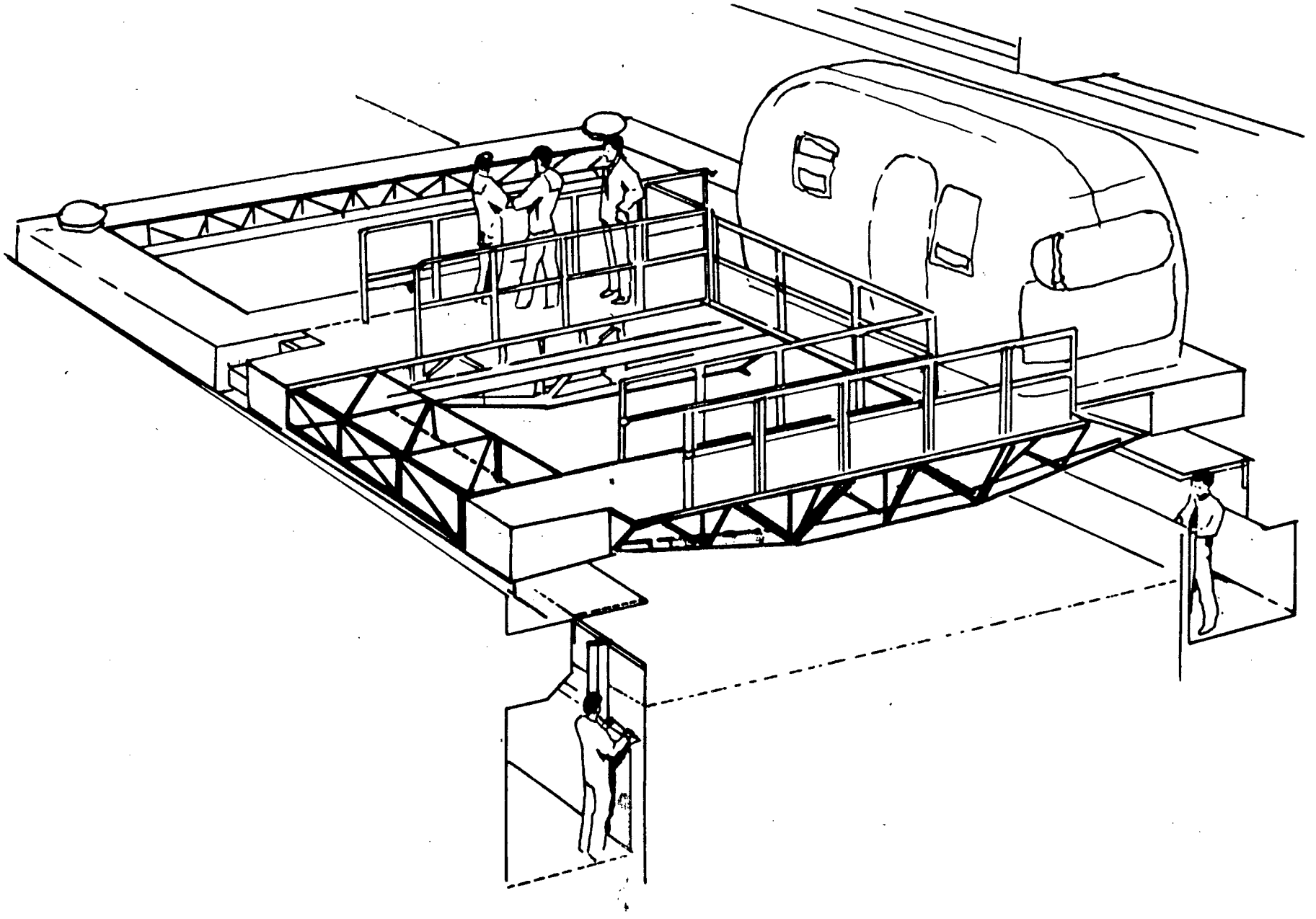

Fig. 4.1: Standard carriage used in modern high performance towing tank.

4.2 Total resistance measurements

The measurement of the total resistance of the model is achieved using instrumentation consisting of a dynamometer, as in Fig. 4.2 or an arrangement of strain gauge load cells. Froude devised the first dynamometer and recorder to be used for measuring ship resistance - apparatus succesfully utilised in Britain until 1950. Considering Fig. 4.2, the model is positioned at the lower end of a diamond shaped frame. A balance weight placed in tray 'a' provides most of the resistance and the extension of the spring records the nett change, improving the accuracy of the measurement, as the percentage difference is a fraction of the total. The spring can be calibrated by placing known weights in pan 'b'.

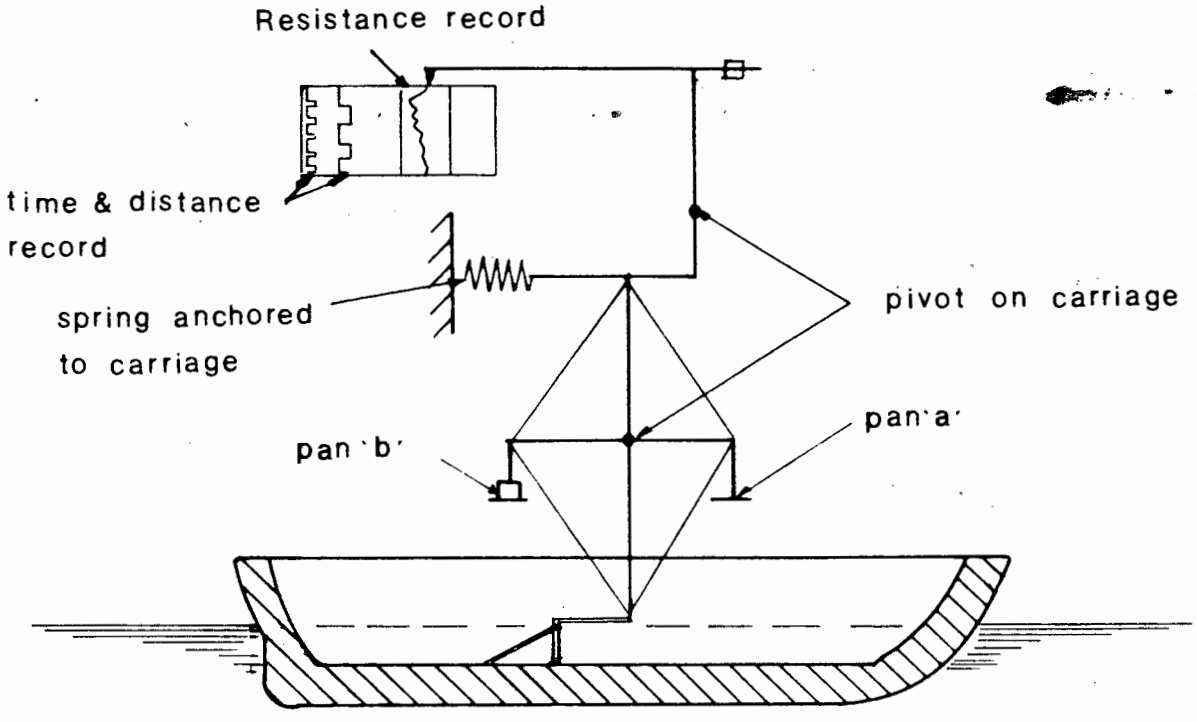

Fig. 4.2: Simplified towing dynamometer

In smaller tanks which require rapid acceleration or do not have towing carriage instrumentation, the gravity or falling weight system is used. These include a system whereby the towing line is attached to a large diameter drum mounted alongside a smaller drum onto which the line carrying the weights is wound. The towing resistance of the model is then the difference of the weights at either end minus the friction of the system divided by the ratio of the drum radii. Other methods to gain initial rapid acceleration utilise heavy weights which can be removed by floating off in a mercury bath once a steady state is reached. Drums of gradually increasing diameter are also used to increase the model speed as the towing line winds on an enlarging spiral until a constant diameter is reached to attain a constant velocity.

The essential difference between the falling weight method and the towing carriage is that the falling weights yield the resistance, leaving the speed to be determined, whereas as the towing carriage/ dynamometer determines the resistance at a pre-determined velocity. A carriage is essential, however, for measurements concerning general ship dynamics.

4.2.1 Turbulence stimulation

Laminar flow can exist on certain models of up to Reynolds numbers of 10^7. This can have a marked effect on the resistance results and turbulence stimulators are needed to reproduce an adequate region of turbulent boundary layer over the length of the model. Types of stimulators are:

(1) Sand strips
(2) Trip wires
(3) Studs
(4) Struts ahead of the model

Allen (1949) found that turbulence stimulators of types (2) and (4) increased the resistance of the model by as much as 10% over a large range of speeds. The most common stimulators are type (3) as used

by Moran (1971) and Ward (1964, 1968), a row of studs being placed ± 0,05 LWL aft of the bow spaced 25 mm apart and projecting ± 2,5 mm. There is a possibility of over stimulation, in that if flow becomes fully turbulent over the length of the model, separation of flow at the stern may vary with scale.

Various tests have been performed, Allen (1949), Gillmer (1975), using ink jets or traces of thread to investigate the streamlines at varying positions along the hull and determine when the boundary layer becomes fully turbulent.

4.3 Division of total resistance into measurable components.

As has been previously discussed, the measured total resistance of the ship is sub-divided into those components depending upon frictional effects and those depending on gravitational effects, according to Froudes hypothesis (Section 3.4.1). Fig.4.3 shows the various sub-divisions of ship resistance and the experimental approaches used to determine the individual components.

Hughes added the form concept of $C_f(1+r)$ to the frictional coefficient C_f, based on the results of geometrically similar models (geosims), this only being an inprovement if the factors were not dependent on Reynolds number. The remaining residual resistance, C_r, now contains wave resistance and an unidentified quantity of form and eddy resistance,

Breaking down the resistance vectorially, the normal pressures are determined by a pressure survey over the hull using fine tappings, and then integrated over the wetted surface area to obtain C_{pr}. This is then subtracted from the total resistance to give the resultant resistance due to the tangential shear stresses. This method does not include the effects of viscous separation, but only the normal pressure components.

Dealing with the physical phenomena of the passage of a ship, we arrive at the third analysis, the formation of waves and the development of a viscous shear wake. To determine the viscous and wave resistance components, a survey of the surrounding energy field is needed;

(a) the area involving the viscous wake;

(b) the region due to the wave surface elevations

This third method has been used most frequently and is dealt with in the proceeding sections.

The measurement of the various wave resistance coefficients, having been defined separately as C_{pr}, C_r and C_w need not necessarily result in direct agreement. Each of these coefficients by their definition, includes or excludes certain effects due to either boundary layer interaction, turbulence stimulation, eddy resistance and form resistance, which the other coefficients do not account for.

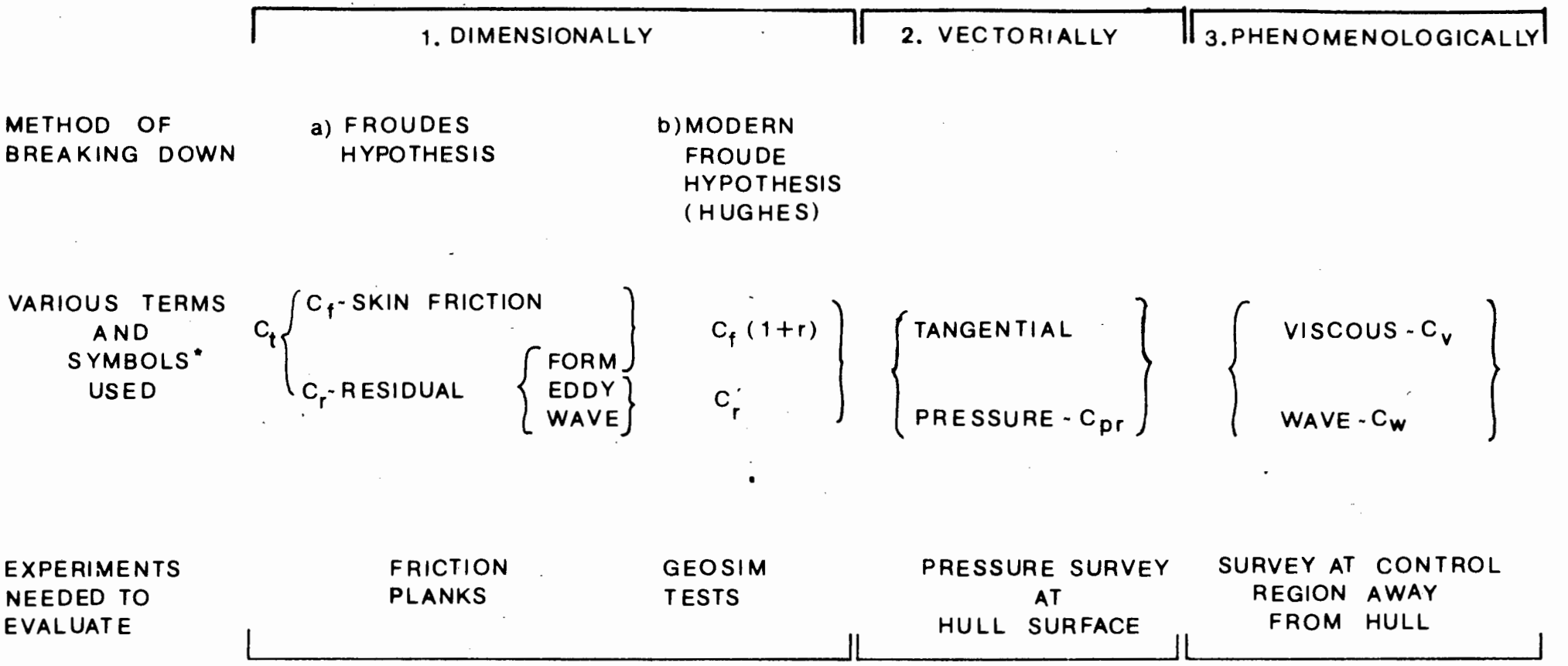

*The various resistances are in coefficient form. $C = \frac{R}{(\rho/2).S.U_m^2}$

Fig. 4.3: Various sub-divisions of ship resistance into measurable components

4.4 Viscous and skin friction resistance

In order to determine the viscous resistance of a model, there are several methods. The viscous resistance, as was briefly discussed in Section 3.4.2.1., can be defined as half of the resistance of a double, or reflex model tested deeply submerged in a towing channel or wind tunnel at the correct Reynolds Numbers. This approach was adopted by Shearer and Cross (1965), Matheson and Joubert (1972) and recently Cooke (1986).

Matheson mounted a reflex model of a tanker, C_B = 0,80, in a wind tunnel, measuring the drag and deducting the resistance of support shrouds to obtain a final result. Several types of turbulence stimulators were used and large differences in drag were found in the higher speed ranges, the agreement being fairly close at lower Reynolds numbers. It was decided that these differences were due to the changes of the origin of the turbulent boundary layer.

The skin friction was measured using Preston tubes placed at intervals over the ships hull. It was found that skin friction varied considerably over the length, being greatest at the bow and falling towards the stern, keeping fairly constant over the midbody. The variations of measured skin friction to that of a flat plate may arise in several ways (Shearer and Cross, 1965).

(i) Variations in the flow regime caused by changes of turbulence stimulators;

(ii) Separation at the stern, also dependent on turbulence stimulation;

(iii) Change of wetted surface area due to varying wave profiles along the hull;

(iv) Effect of changes of velocity over the hull surface.

Another method of determining viscous resistance is through momentum surveys in the ships wake. This has been used by several researchers, most notably Lackenby (1965), Shearer and Cross (1972), Tsai (1972), Townsin (1970) and Miyata (1980). The results show that the viscous resistance determined in such a way correlates closely to that of a reflex model.

The method requires pitot tube measurements to be taken across the wake of the model and analysed to give the head loss and thus the loss of the momentum throughout the wake. The method used by Townsin (1970) is briefly illustrated.

The head loss measurements aft of a 4,5 m 'Victory' model were measured using a combined total head comb and manometer system placed half a model length astern. Measurements of the distribution of the total head across the wake were taken every 51 mm below the mean water level to a depth of 460 mm immersion. The head tubes were spaced 25 mm apart at the edges of the wake and 13 mm apart at the centre. The drag is then calculated using the following equation (Townsin, 1970).

$$\text{drag} = 2\,G_o \iint \sqrt{t - p}\,(1 - \sqrt{t})\,dy\,dz$$

$$= 2\,G_o \iint (d)\,dy\,dz \qquad \text{(Eq 4.1)}$$

where $p = \frac{P_1}{G_o}$

$t = \frac{G_1}{G_o}$

$G_o = \frac{1}{2}\,\rho\,U^2$

$d = \text{drag function}\,f(P_1 G_1 G_0)$

G_1 is the measured local total head and P_1 is the local static head calculated from the wave height. p is the static head in the wake non-dimensionalized by the free stream dynamic head, G_0.

Fig. 4.4 (A) illustrates the variations of d, the drag function of

Eq 4.1 across the wake for one fixed speed. The wake has nearly disappeared at the lower immersion level. The distribution in the upper regions of the wake is due to the rotational nature of the flow. Fluid having a lack of momentum in the middle regions of the wake would be taken upwards at the edges and downwards at the centre, resulting in the peaked distributions shown. The curves in (A) are then integrated with respect to y, yielding a plot of the d.dy with the depth of the wake, shown in Fig. 4.4 (B).

These curves show a minimum at about half the wake depth followed by a bulge tapering to zero at the lower levels, indicating the rotational tendencies of the wake. These results are then integrated to yield the final viscous resistance coefficient, C_V.

The undulating nature of C_V, also confirmed experimentally by Shearer and Cross (1965) shows that viscous resistance is not only dependent on Reynolds number, but is also a function of Froude number.

Momentum loss measurement techniques have become a standard method of experimentally determining the viscous resistance. Miyata (1980) used such a method for determining the component of resistance of free surface shock waves for several ship forms with and without bulbous bows. Miyata and Inui (1985) integrated the contours of loss of velocity head to compare and evaluate the effects of non-linear wave resistance.

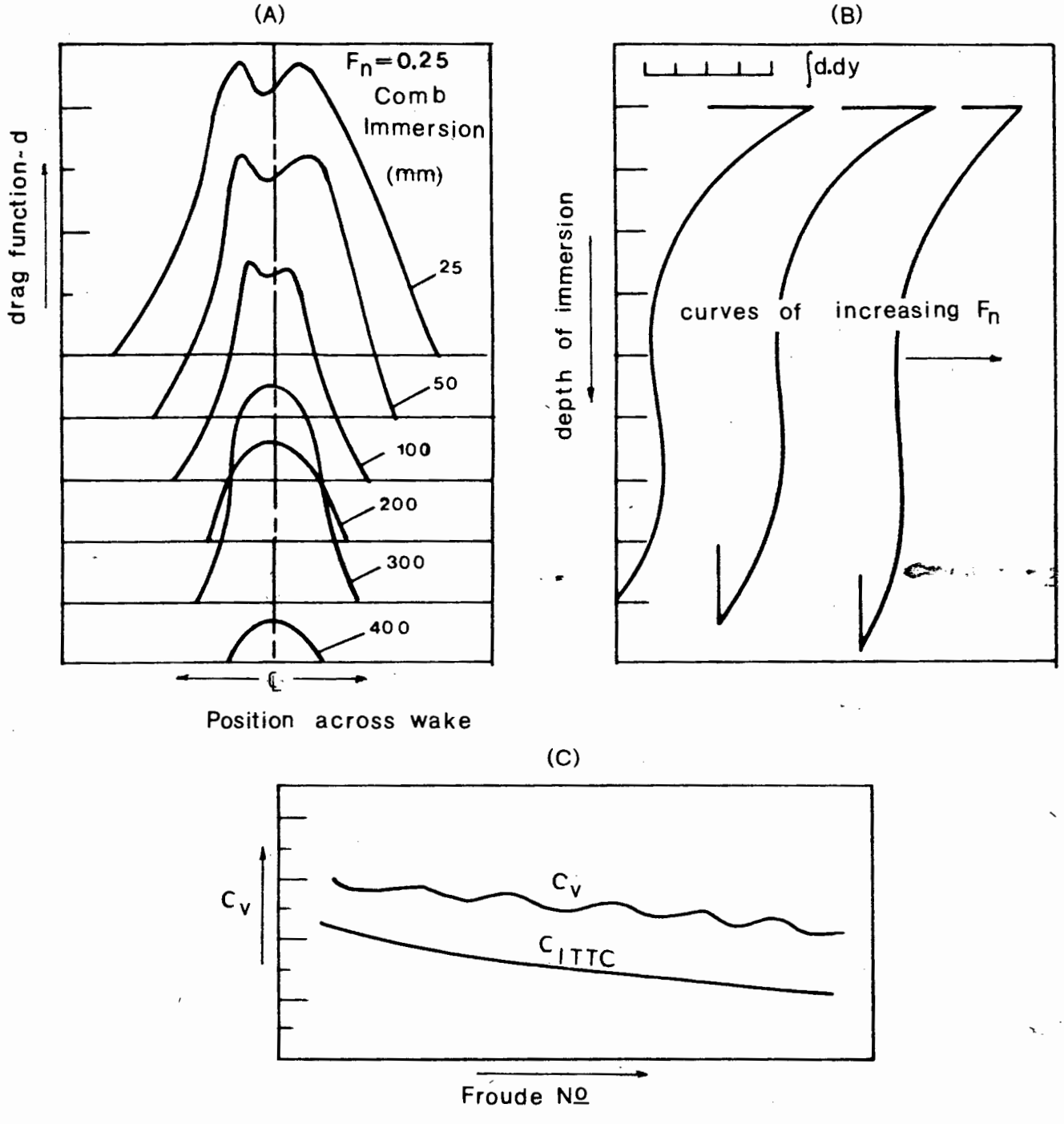

Fig. 4.4: Results of C_v (Townsin (1970) determined using wake traverse measurements

4.5 Wave making resistance

As has been discussed in section 4.3 the wave resistance can be determined using three approaches, dimensional, vectorial and phenomenological, corresponding to he coefficients C_r, C_{pr} and C_w.

Considering the wave pattern generated by a moving ship, the effects of the hull geometry are visible as a direct quantitative measurement of the water surface. Through analysis of the wave pattern the wave resistance can be evaluated using several methods. These methods are independent of hull form, geometry and viscous phenomena associated with the boundary layer. The third measure of wave resistance, C_w, is thus a measure of the amount of energy actually going into the real fluid.

4.5.1. Momentum analysis

Considering a ship moving along a constant path at constant speed, U, as shown in Fig. 4.5, bounded by the space ABCDC'B'. The model creates a system of waves in region I contained within the Kelvin cusp lines.

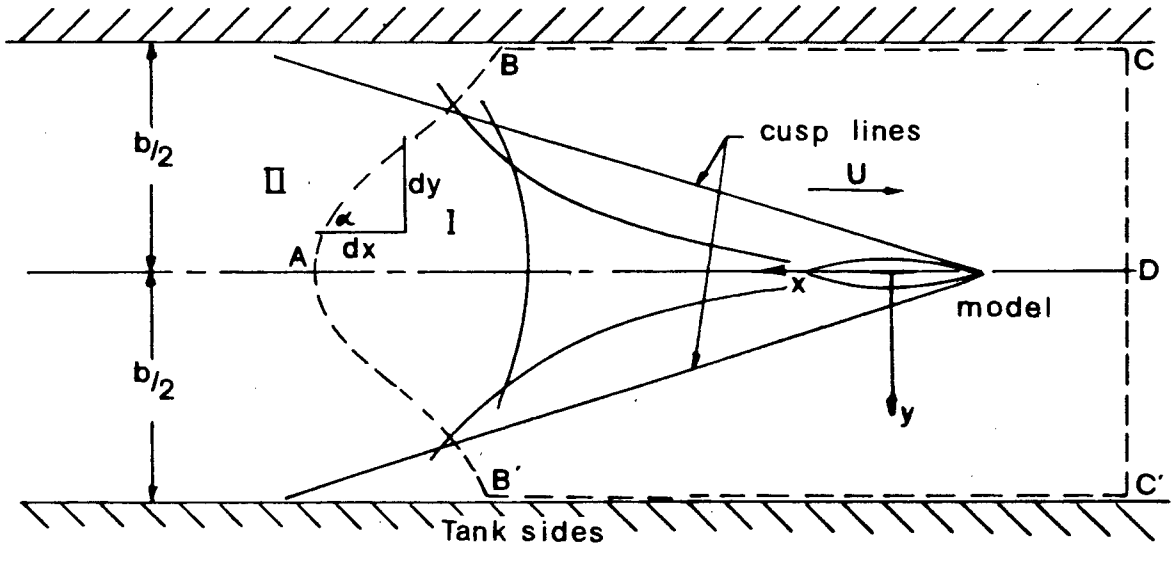

Fig. 4.5: Energy balance control volume

Equating the rate of energy growth to the work done by the fluid at the boundaries of the region, we obtain a general formula to express R_w in terms of the flow components and wave profile at surface AB as (Eggers (1975), Wehausen (1973);

$$R_w = \rho g \int \eta^2 \, dy + \rho g \int_{-h}^{\eta} dz \int_{AB} (U^2 + V^2 + W^2) \, dy \qquad \text{(Eq 4.2)}$$

$$- 2\rho \int_{-h}^{\eta} dz \int_{AB} U \, (U - V \tan \alpha) \, dy$$

where $Z = (x,y)$ is the wave elevation, (U, V, W) are the fluid velocities in the x, y, z directions and $\tan \alpha = {}^{dx}/_{dy}$. This equation is termed the Havelock formula for a general path AB.

4.5.2 Transverse cut method

Using Eq.4-2 and setting the path AB perpendicular to the direction of motion of the model, $\alpha = 0^o$, and assuming a restricted tank width of $y = {}^{b}/_{2}$ then gives:

$$R_w = \rho g \int_{o}^{b/2} \eta^2 \, dy + \rho \int_{-h}^{\eta} dz \int_{o}^{b/2} (- U^2 + V^2 + W^2) \, dy \qquad \text{(Eq 4-3)}$$

To obtain transverse profiles of the ship wave elevations, requires the use of wave probes that move on a transverse track relative to the water at the speed of the model. This generally requires sonic type probes which do not penetrate the water. Several transverse cuts are generally taken at different positions and then a least squares fit gives the average of the values obtained from each profile. The results of Kobus (1967) and Landweber and Tzou (1968) confirm that this method results in errors of less than 1% for profiles taken at more than a ship length behind the model (Wehausen, 1973).

4.5.3 Longitudinal cut methods

The measurement of longitudinal profiles has important advantages over transverse profiles. A wave gauge can be fixed in position while a model or ship passes by obtaining a record of surface elevations that are free of wake interference. In cases where the wave is reflected off the walls of towing channels, assumptions can be made regarding the derived wave profile, resulting in a longer available record length.

For a longitudinal cut method and using Eq. 4.2 and setting $\alpha = \pi/2$ then (Eggers, 1976):

$$R_w = 2\rho \int_{-h}^{\eta} dz \int_{-\infty}^{+\infty} U\, V\, dx \qquad \text{(Eq.4.4)}$$

A series of longitudinal cuts can be evaluated and truncated before the first wall reflection, or a single cut including wall reflections can be used, truncating at an order of series sufficient to ignore additional effects (Moran, 1977) (Fig.4-6).

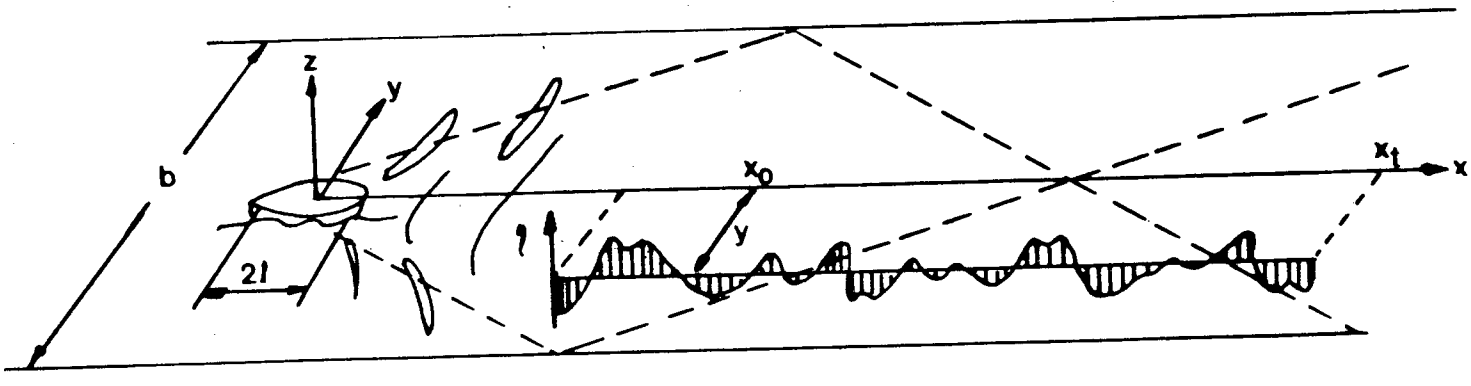

Fig. 4.6: Waves in a towing tank

The wave pattern produced by a moving body is given by (Tsai, 1975):

$$\eta\,(x, k_o) = \sum_{m=o}^{\infty} [C_m\,(k_o) \cos \omega_m x + S_m\,(k_o) \sin \omega_m x] \cos \frac{2\pi m y}{b} \qquad \text{(Eq 4.5)}$$

providing that the record is sufficiently aft of the model to neglect the near field portion of the wave equation (for $x > 2\ell$)

where $k_o = g/U^2$

$$k_m = \sqrt{k_o^2 + \nu_m^2}$$

$$\nu_m = \frac{4\pi m}{b}$$

$$\omega_m = \sqrt{\tfrac{1}{2} k_o (k_o + k_m)}$$

The wave resistance produced by a body is given by Eggers, Sharma and Ward (1967):

$$C_w = \frac{k_o b}{2\ell^2} \left[C_o^2 + S_o^2 + \sum_{m=1}^{\infty} \frac{k_m}{k_o + k_m} (C_m^2 + S_m^2) \right] \qquad \text{(Eq 4.5)}$$

To determine the set of unknown coefficients, Moran and Landweber (1972) used a set of Fourier transforms to determine C_m and S_m for a series of order m.

The positions of the transverse record were varied across the tank width and it was found that for a sufficiently high order series of truncation the values were consistent, suggesting that effect of the wake on this method is negligible.

For a complete theoretical study of the decomposition of the longitudinal cut technique, see Eggers, Sharma and Ward (1967 and Newman (1963). Other researchers having successfully utilised this approach are Tsai and Landweber (1975), Wehausen (1973), Moran (1973).

4.5.4 Other methods of direct measurement

Two other methods, based on equation 4.2, have been proposed and developed by Ward (1964, 1968) involving measurements of functions of the elevation of the water surface.

4.5.4.1 X-Y method

This is based upon the measurement of the force acting on a long vertical cylinder placed in a position suitable for measuring longitudinal wave profiles. The assumption is that the force exerted on the cylinder by a plane oncoming wave is proportional to the wave amplitude, a prediction based upon the linearized theory of water-wave diffraction in an inviscid fluid.

The force components on the cylinder in the x and y directions are measures of the wave amplitude and being measured over the depth of the cylinder, provide measured quantities of the depth integrals in Eq. 4.2.

The problem associated with this method is the calibration of the force of the waves on the cylinders for sufficiently small wave amplitudes. The forces involved are due to the accelerations of the water particles during diffraction of the waves. Circular cylinders have substantial viscous drag in a viscous flow and this could interfere with the force measurements. Ward overcame this by using cylinders of diameter large enough such that the viscous forces are small in relation to the inertial fores (Ward and Snyder, 1968).

4.5.4.2 Lateral wave slope measurements

An alternative measurement of an integrable quantity associated with wave height was proposed by Ward (1968), who measured the lateral wave slope along longitudinal profiles. Thus a measure of $d\zeta/dy$ was used to obtain the wave resistance from Eq. 4.2.

A resistance type probe was specially developed, employing three vertical thin stainless steel wires. These wires could be rotated in either direction to produce slope variations of 0,20 radians, thus enabling accurate calibration of the lateral slope of the water surface.

4.6 Proposed method for experimental evaluation of the wave resistance from the wave pattern

Equipment exists in the UCT Civil Engineering Laboratory to take instantaneous stereo photographs of a waved water surface in the wave basin and through computer analysis an accurate graphical contour plot of the deformed surface is obtained (see Chapter 5). Through a previous feasibility study (Paterson, 1984) by the author, it was decided that the equipment could be utilised for determining the wave pattern generated by a moving ship.

If the free wave pattern of a model ship can be plotted accurately, then this wealth of information can be utilised to yield the wave drag of the ship.

Using Froude's original concept of wave making drag "Now waves represent energy, or work done, and therefore all the energy represented by the waves wasted from the system attending the ship is so much work done by the propellor ..." (Ch. 2 pg 4). The following method was proposed.

The approach is essentially a derivative of the phenomenological viewpoint to evaluating wave resistance. Considering Fig. 4.7 illustrating the wave pattern generated by a moving vessel between two planes I and II. Plane I being ahead of the ship, plane II being in the rear of the ship. At time t_0 the wave pattern is illustrated as solid lines. In a time increment of Δt, it will have advanced to the position B, shown by the dashed lines. (At time $t_1 = t_0 + \Delta t$). There is an increase in the energy of the fluid between planes I and II equal to the increase of wave energy corresponding to the increase in the area of the free wave pattern.

The wave pattern of a moving ship is stationary with respect to the ordinates of the ship. A contour plot of the water surface elevations at time $t_0 + \Delta t$, or position B, will contain the portion of the wave field included beyond plane II at position A.

The cross hatched area in (C) of Fig. 4.8 represents the additional wave energy generated in the time interval Δt, denoted $\overline{E}\,\Delta x$, where $\overline{E}$ is the average energy per metre along the sailing line in the cross hatched zone.

The rate of increase of energy in the wave field is equivalent to the rate of work done by the ship as it advances against wave making resistance, R_w, expressed as equation 4.7:

$$\overline{E}\,\Delta x = R_w\,\Delta x$$
$$R_w = \overline{E} \qquad \text{(Eq. 4.7)}$$

The wave making resistance is thus found by evaluating the energy increase in the surface wave pattern. The basis of this thesis is to apply such a method at several ship speeds to validate the proposed energy analysis procedure.

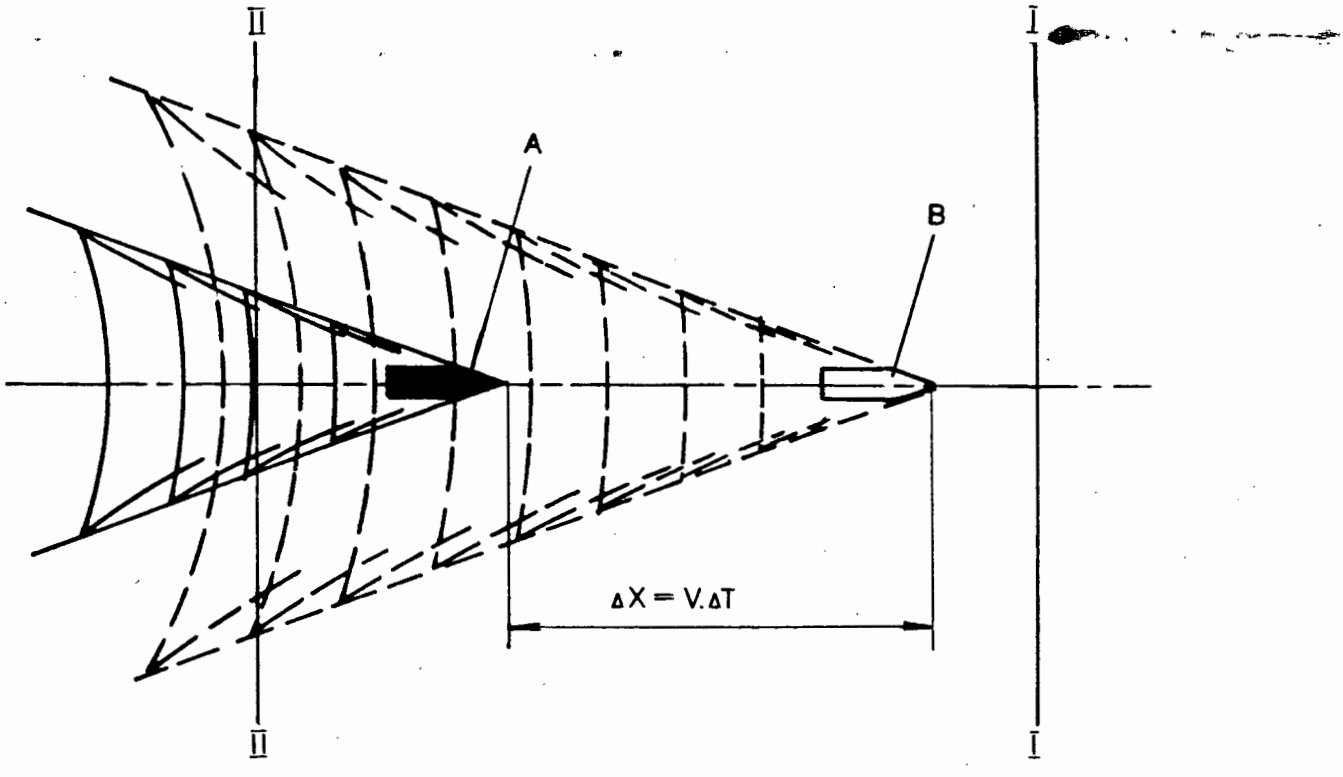

Fig. 4.7: Wave pattern of a moving ship advanced through a distance Δx.

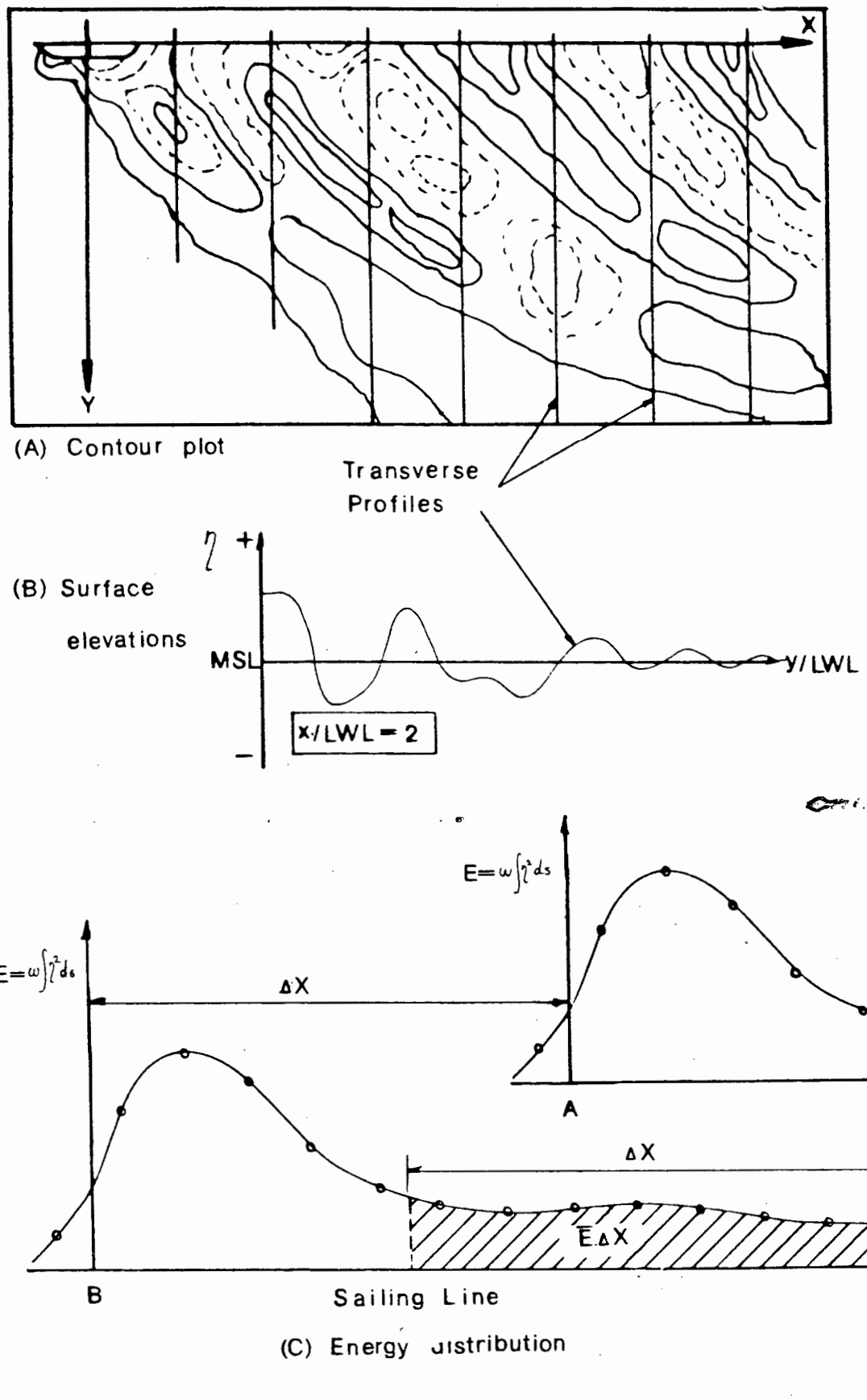

Fig. 4.8: Determination of wave resistance R_W

5. PHOTOGRAMMETRIC WAVE HEIGHT MEASUREMENT

5.1 Close range photogrammetry

5.1.1 Introduction

Photogrammetry is the science of recording reliable, accurate, information concerning physical objects and the environment through the processing and interpretation of photographic images. Two distinct fields of photogrammetry exist:

(1) Metric photogrammetry involving precise and detailed analysis to determine the spatial dimensions of objects.

(2) Interpretive photogrammetry involving photographic interpretation and remote sensing in order to recognise and identify objects.

Close range photogrammetry is a branch of metric photogrammetry encompassing situations where the distance between object and camera ranges from as little as a fraction of a millimetre to distances of up to 300 m.

This study deals with dynamic ship applications requiring the use of two cameras to simultaneously record the action and obtain a stereopair (a pair of photographs taken of the same physical object, each one being taken at opposite ends of a baseline).

5.1.2 Basic theory of short range photogrammetry

In order to determine the complete geometry of a three dimensional terrain, two photographs are needed. Consider Fig. 5.1, describing the determination of the height of a single point. The two cameras are both positioned vertically and situated at the same altitude (H_f) at positions S_1 and S_2.

The point A at height h_A above datum appears at a_1 and a_2 on the equivalent positions shown on the negatives at S_1 and S_2. The distance S_1S_2 is the base line distance, B.

If one constructs $S_1\tilde{a}_2$ parallel to S_2A_2, then it can be seen from similar triangles that:

$$\frac{a_1\tilde{a}_2}{S_1PP_1} = \frac{B}{H_f - h_A} \qquad \text{(Eq. 5.1)}$$

$S_1PP_1 = f$, the focal length of the camera and $a_1\tilde{a}_2$ is known as the absolute parallax of point A. Therefore the absolute parallax of point A is given as:

$$P_A = \frac{f \times B}{H_f - h_A} \qquad \text{(Eq. 5.2)}$$

$$\text{thus } h_A = H_f - \frac{B \times f}{P_A} \qquad \text{(Eq. 5.2)}$$

In order to measure the parallax of a point, surveying equipment, such as a parallax bar or stereocomparator is needed. If h_A is known, any point (say D) in the stereopair overlap area can be found by the following procedure.

Using Eq. 5.2, calculate P_A since f, B, H_f and h_A are known. Measure the difference in parallax (P_A-P_D) between point A and point D, using photogrammetric survey apparatus. As P_A is known, P_D can be found. Thus h_D can be calculated using Eq. 5.3. h_D is called the crude height of point D. These parallax equations assume the camera axes to be truly vertical and the camera stations the same height. This is rarely true in practice and the equations are modified to suit the general case.

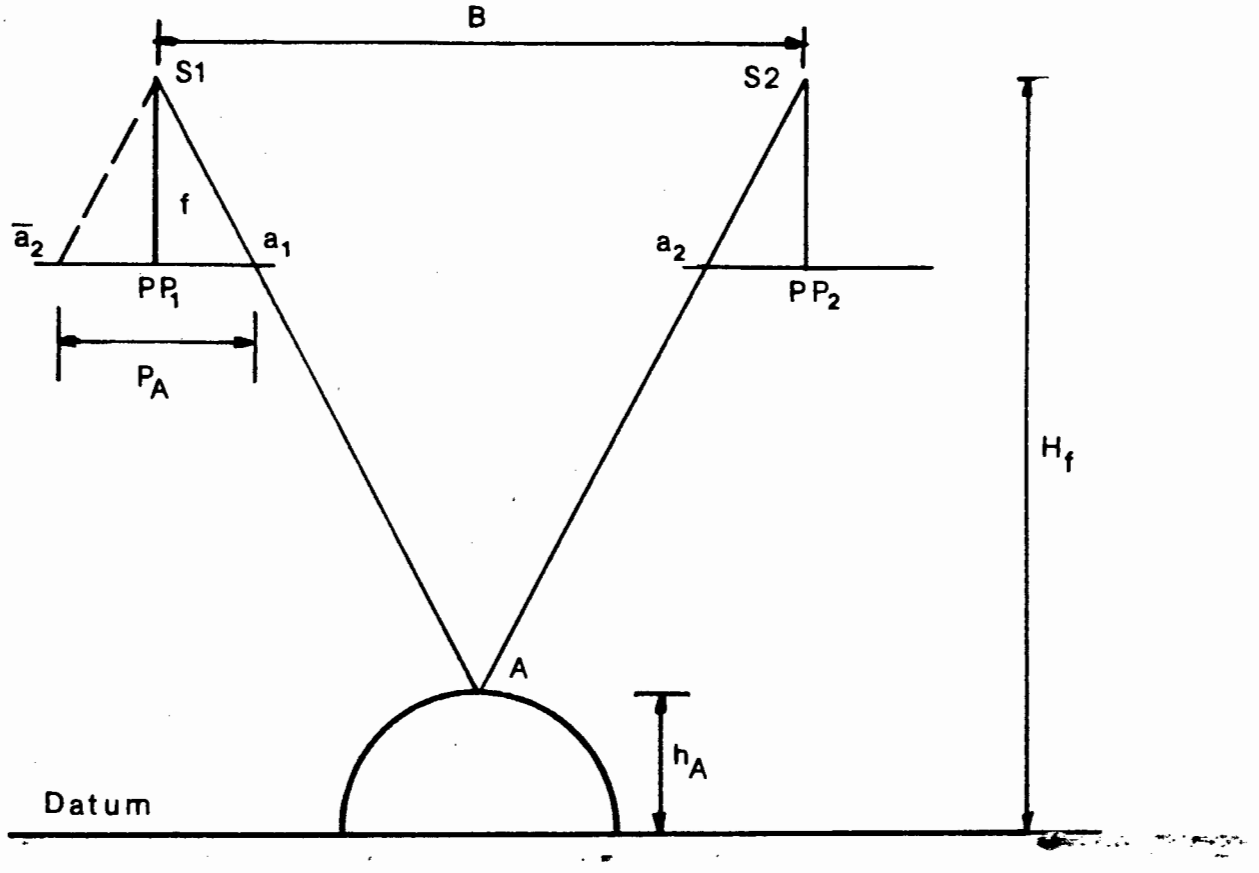

Fig. 5.1: The determination of the height of a point on the terrain

5.2 Previous wave pattern measurement using photogrammetry

The first recorded instances of photogrammetric wave height measurement were made in Germany early this century. Cameras were mounted on several vessels in the period 1925 - 1939 in attempts to measure ocean swell characteristics. Most of these efforts were only partially successful due to the problems of reconstructing the reciprocal positions of the cameras to each other on the negative plates and to maintain a base line of suitable length.

Wave length elevations have been measured by cameras placed along the coastal zone (Adams, 1978). Techniques have been developed to determine the wave energy spectra at sea using aerial stereophotography. At higher altitudes the cameras are mounted in separate aircraft flying a known distance apart, or at lower levels mounted on helicopters.

Close range photogrammetry has been used to determine wave heights in several applications of hydraulic modelling. Pos (1984) developed the present procedure used for the determination of breakwater-gap diffraction problems. Ship wave patterns have been analysed by Sorenson (1968), Inui (1962) and Moffit (1968). The paper by Moffit was found to be the most pertinent and a full discussion is given in the next section.

5.2.1 An appraisal of the paper "Wave Surface Configuration" by Prof. F.H. Moffit

Moffit set out to determine the feasibility of applying stereo photogrammetry to measure the wake of a ship model in a wave basin. The model basin covered an area of 19 m x 45 m and was filled to a depth of 200 mm. The model used measured 1600 mm in length and 200 mm across the beam. Stereopairs were taken using two Rolleiflex wide-angle cameras located 6 m above the wave basin. Kodak Tri-X glass plate negatives were used to obtain the necessary exposure speed for lighting conditions. To synchronize the firing of the cameras, pneumatic air releases triggered the shutters simultaneously. To

obtain the water surface configuration confetti was strewn over the surface by hand. This caused problems due to local basin currents and the extent of the area to be covered. The negatives had to be reduced to diapositives to obtain the same horizontal and vertical scales, a time consuming and tedious process requiring a reduction printer of high accuracy. The reduced diapositives were measured on a Balpex stereoplotter. The relative orientation of the plates was difficult to obtain due to the random and systematic errors which Moffit ascribed to the relatively crude system used and the distortion due to the wide angle camera lenses. Moffit recognized that the hydraulic engineer must specify the areas to be measured to the photogrammetist. This is extremely important if one is to infer useful information from the plots, as the stereoplotter operator might not recognize critical aspects of the wave pattern.

Several ship runs were photographed and at higher speeds y-parallax was detected due to the movement of the wake during the exposure interval of 1/60 second. This was adjusted for in the stereoplotting and contour maps were successfully drawn of the water surface. The estimated accuracy of these plots was $\pm$ 4 mm on the water surface which, when dealing with plotted heights of a maximum of 40 mm represents a percentage error of 10%.

Although this study did not produce highly accurate results it did verify the usefulness of such a method of wave height determination.

5.3 Equipment

5.3.1 Zeiss Jena UMK 10/1318 universal measuring camera

A pair of Zeiss Jena metric cameras was used for this study. Each camera utilises the almost distortion free Lamegon 8/100 lens system and is mounted on a single second theodolite alidade. The cameras were mounted in specially designed wooden carriages above the wave basin. The principal distances of the cameras can be altered so as to allow for focusing for distances from 3,6m to infinity. The cameras are designed for use with large format glass plate negatives. Due to the unavailability of glass plates, it was decided to mount Ilford HP5 sheet film onto used plates. A special spray adhesive was used to coat the plates and this permitted easy removal of the film for developing. The rating of the film was 400 ASA.

5.3.2 Carl Zeiss Jena Steko 1818 stereocomparator

The analysis of the negatives was performed using the Carl Zeiss Jena Steko 1818 Stereocomparator in the Surveying Department's photogrammetry laboratory at U.C.T. (Fig. 5.2). Observations were done in stereoscopic mode using both plates at all times. The accuracy of this instrument is better than 10 μm in x and y co-ordinates and 2 μm in px and py readings. A Motronic electronic analogue to digital display unit was interfaced to a Hewlett Packard 9816 computer as described in Section 5.3.3.

5.3.3 Hewlett Packard 9816/UNIVAC 1100 system

The analysis of the projective transformation parameters obtained from the stereocomparator was done on a Hewlett Packard 9816 mini computer. The stereocomparator was linked to the HP9816 via the Motronic display unit. Using this system, the x, y and px, py data was fed directly to the computer and stored on disk. This data was then transformed into XYZ co-ordinates using a Projective Transformation program written by Prof. H. Ruther of the Survey department. The XYZ data was then transferred to the mainframe UNIVAC 1100 for subsequent processing and plotting.

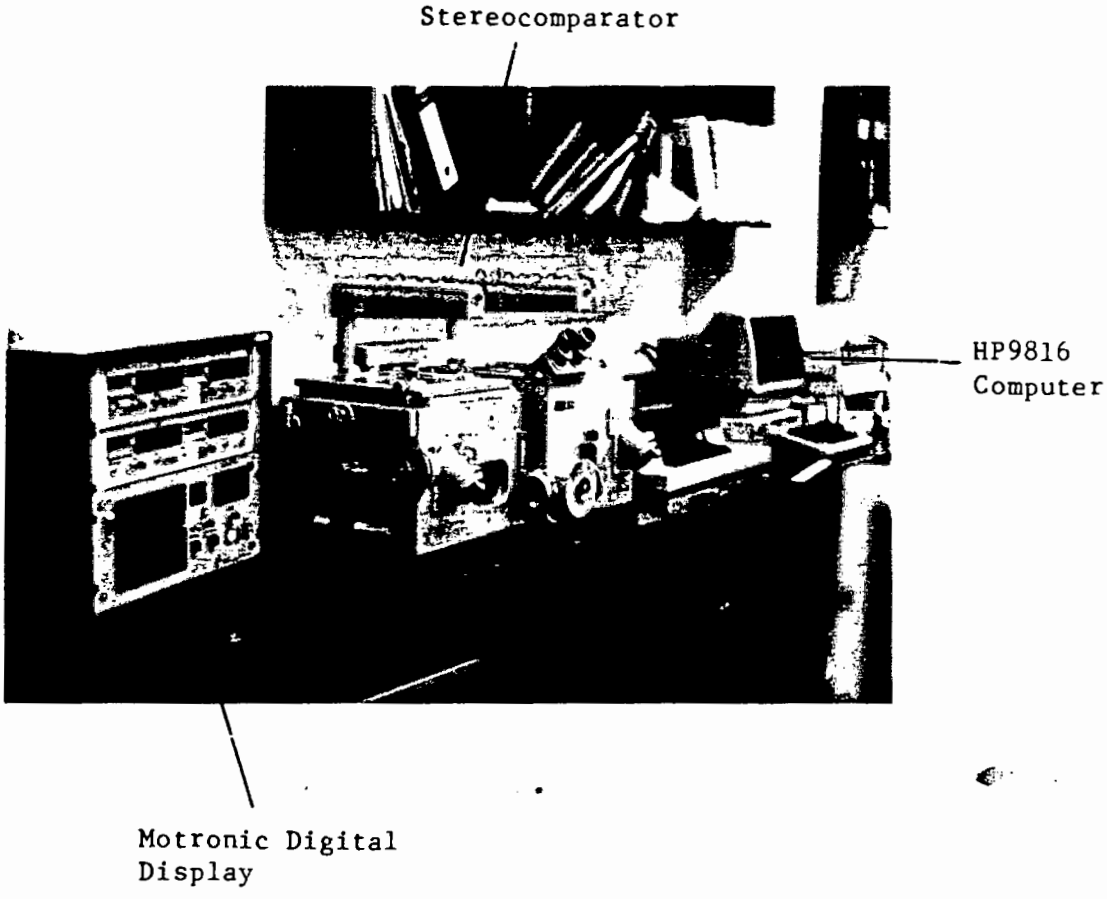

Fig. 5.2: Stereocomparator and peripherals

5.4 Laboratory photogrammetric wave height measurement

5.4.1 Water penetration

When taking photographs of a waved water surface it is necessary to highlight the surface, for accurate identification on the photographs. Two fundamental techniques have been used to define the water surface for photographic purposes.

(1) Discolouration of the water so as to reduce light penetration to a minimum.

(2) Application of a thin flexible film of some reflective substance on the water surface.

The second method was used by Moffitt (1968) as described in Section 5.2.1 and by Inui (1962). Inui sprayed fine aluminium powder on the surface. The powder separated when the ship passed through and did not "close" in the wake, due to the effects of the boundary layer and turbulence, thus rendering a large area aft of the ship wake unusable for photographic purposes.

The first approach was adopted and developed by Pos (1984) at U.C.T., using a concentration of 7 to 8 ml/litre of Shell Dromus B Soluble Cutting Oil, to render the water an opaque white throughout. The light penetration using this concentration is approximately 1 mm. The viscosity of the solution was compared with clear water (Pos, 1984) and no difference could be detected. This is the approach used in this study.

5.4.2 Camera configuration

The Zeiss Jena cameras were positioned 5 m above the wave basin and spaced 1.9 m apart. This provided an effective field of view of 6 m x 8 m and an overlap of 6,2 m. Fig. 5.3 shows the cameras in their wooden mounting boxes. These carriages allowed for the easy removal of the cameras and could be levelled by means of a three bolt tri-brach arrangement.

Fig. 5.3: Photographic platform

5.4.3 Camera firing system

Since the water is in motion, it is necessary to fire both cameras simultaneously so as to minimise the effect of image movement, using fastest possible exposure times.

In order to use the Zeiss cameras this way, a synchronization box is provided which fires both cameras simultaneously when a manual switch is operated. For this exercise the manual switch was bypassed by a photo-electric relay circuit which, when broken, would activate a timer, allowing the synchronization box to discharge a capacitator and fire the cameras. The light beam was placed across the wave basin and activated by a black perspex plate mounted on the ship's stern.

5.4.4 Illumination

It is essential to provide sufficient illumination of the water surface to allow for adequate exposure of the photographic emulsion at high shutter speeds. The configuration used consisted of four 250 W overhead projectors mounted above the wave basin (Fig. 5.4). Each of these illuminated an area of 3 m x 3 m.

These projectors were pre-focused for water depths up to 600 mm at intervals of 100 mm. The positions of the reflex mirrors were marked on the supporting arms.

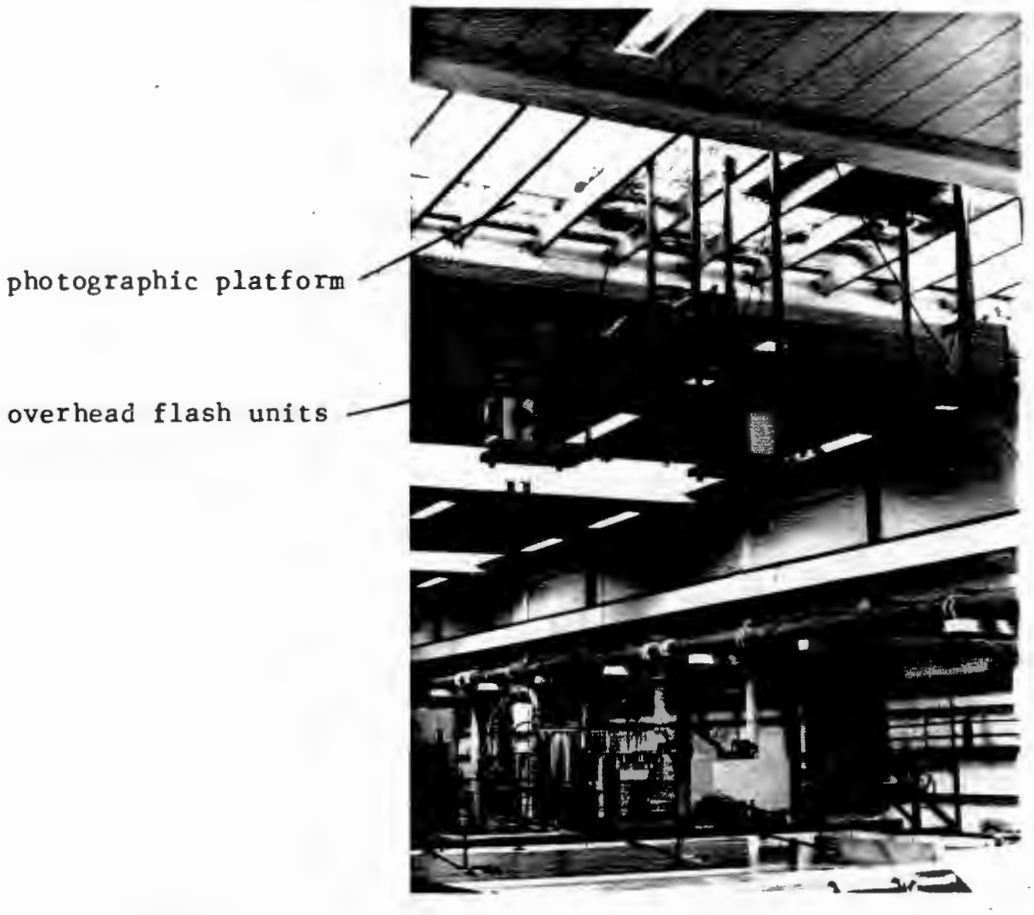

Fig. 5.4: Projector platforms above wave basin

5.4.4.1 Flash systems

Problems encountered in the stereographic analysis of the stereopairs are often caused by a poorly defined surface and blurred images due the movement of the surface during the shutter interval. To overcome these problems, Pos (1984) developed the overhead flash system which was utilised in this study. The four overhead projector bulbs were replaced by flash tubes rated at 50 J. As these tubes have an illumination duration of less than 1 ms, the resulting stereophotographs are 'frozen' in motion and sharp and well defined.

The sequence of operation of the flash system is shown in Fig. 5.5. The camera synchronization circuit is activated by the photo-electric circuit and the slow camera activates the flash contact. A shutter speed of $^1/_{30}$ second was chosen for adequate illumination and good exposure of the control points on the negatives and also to ensure synchronisation on both camera shutters when the flash was fired by the slower camera.

5.4.4.2 Photographic contrast

The soluble cutting oil overcomes the problem of water penetration but introduces inadequate photographic contrast on the surface, i.e. the white wave surface would appear blank. To overcome this problem, Pos (1984) utilised random patterns positioned on the overhead projectors which were flashed onto the water surface at the time of exposure.

This provided an excellent black and white contrasting surface when viewed stereoscopically. The random pattern was chosen above regular repeated images so as to reduce eye strain and operator fatigue when analysing the plates. Regular patterns tend to fuse together and oscillate when viewed for a period of time.

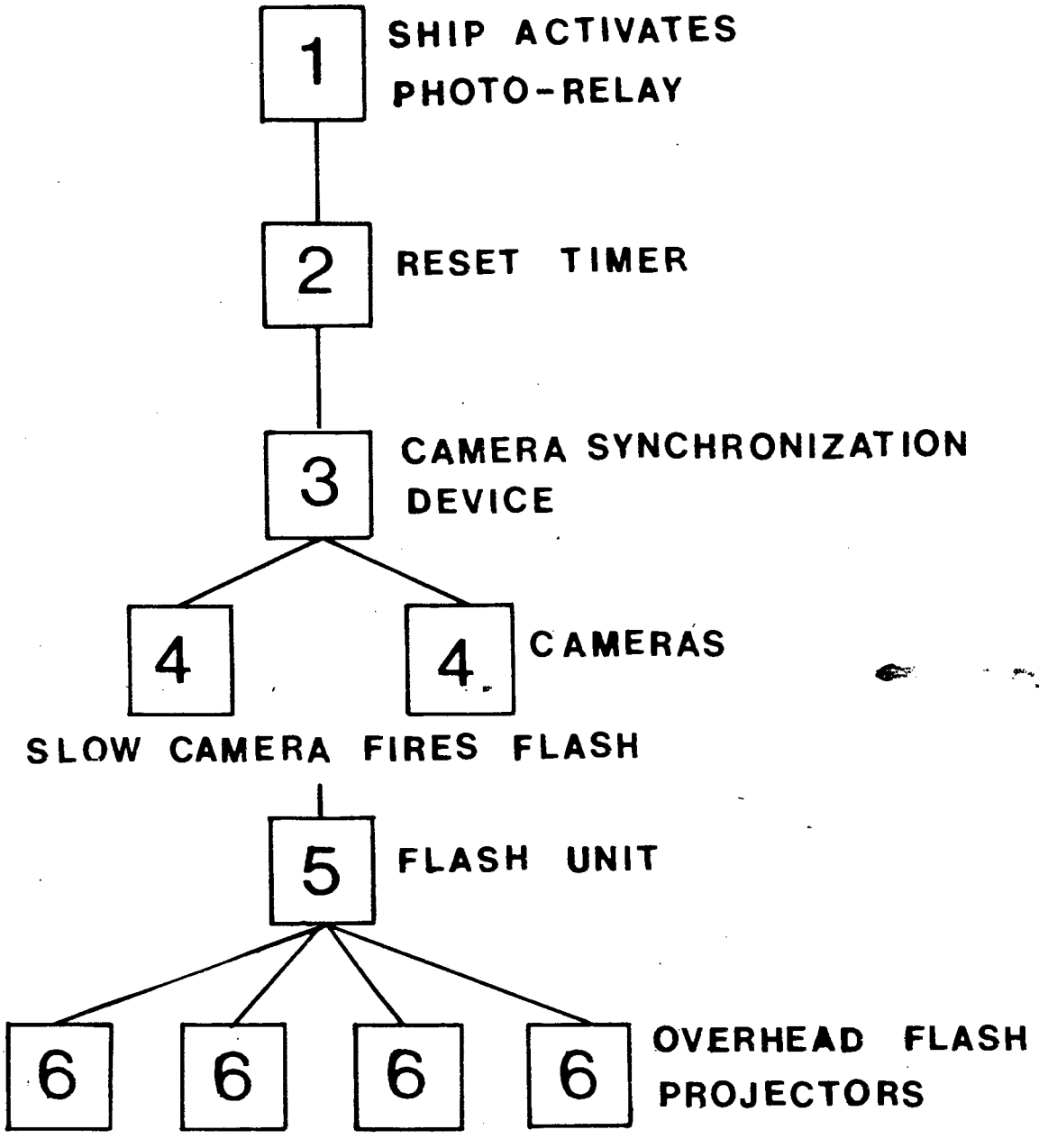

Fig. 5.5: Basic sequence of operation

5.5 Wave basin control point configuration

5.5.1 The 16 point wave basin control configuration

On the basis of Pos (1984) who utilised a 16 point control configuration, a similar configuration was used for this study. The number of control points used determines the measurement accuracy of the observations. Welham and Pos (1984) found that using less than 10 points in an adjustment would not produce a result, but between 16 and 20 points provided the most efficient number. Fig. 5.6 shows the trend of the relationship of the standard deviation to the number of control points used.

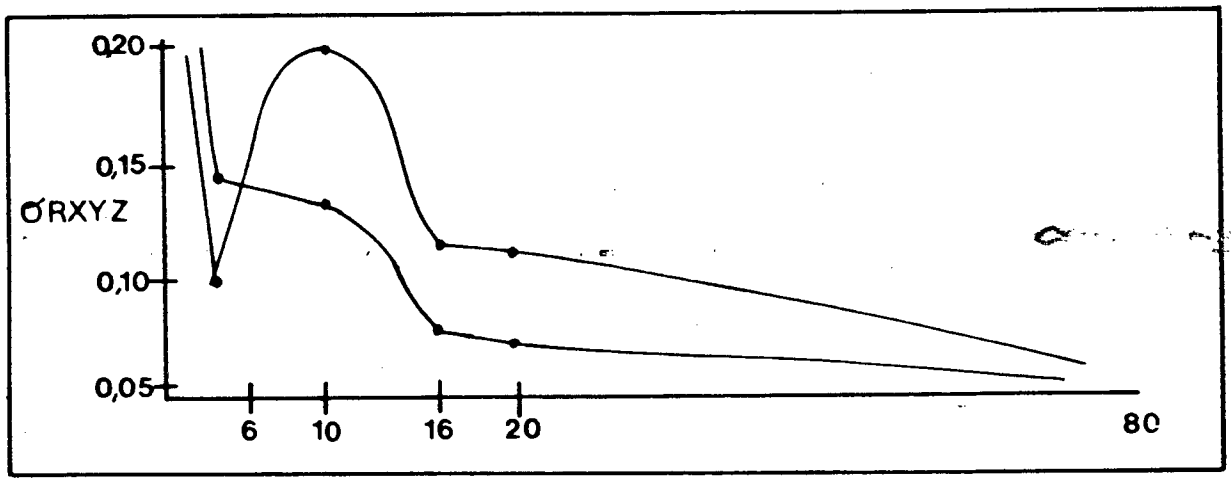

Fig. 5.6: Accuracy as a function of number of control points

The 16 point configuration adopted is shown in Fig. 5.7 and consists of 3 horizontal planes. If a water depth of 500 mm is assumed, the upper plane (points 1 - 14) is approximately 420 mm above the water surface, the targets' being supported on rigid wooden arms. The middle plane of 8 points (points 5 - 12) is approximately 200 mm above the water surface and is supported on steel brackets placed transversely across the wave basin. The lower plane (points 13 - 16) is situated approximately 65 mm below the water surface in metal canisters braced to the side walls (Fig. 5.8).

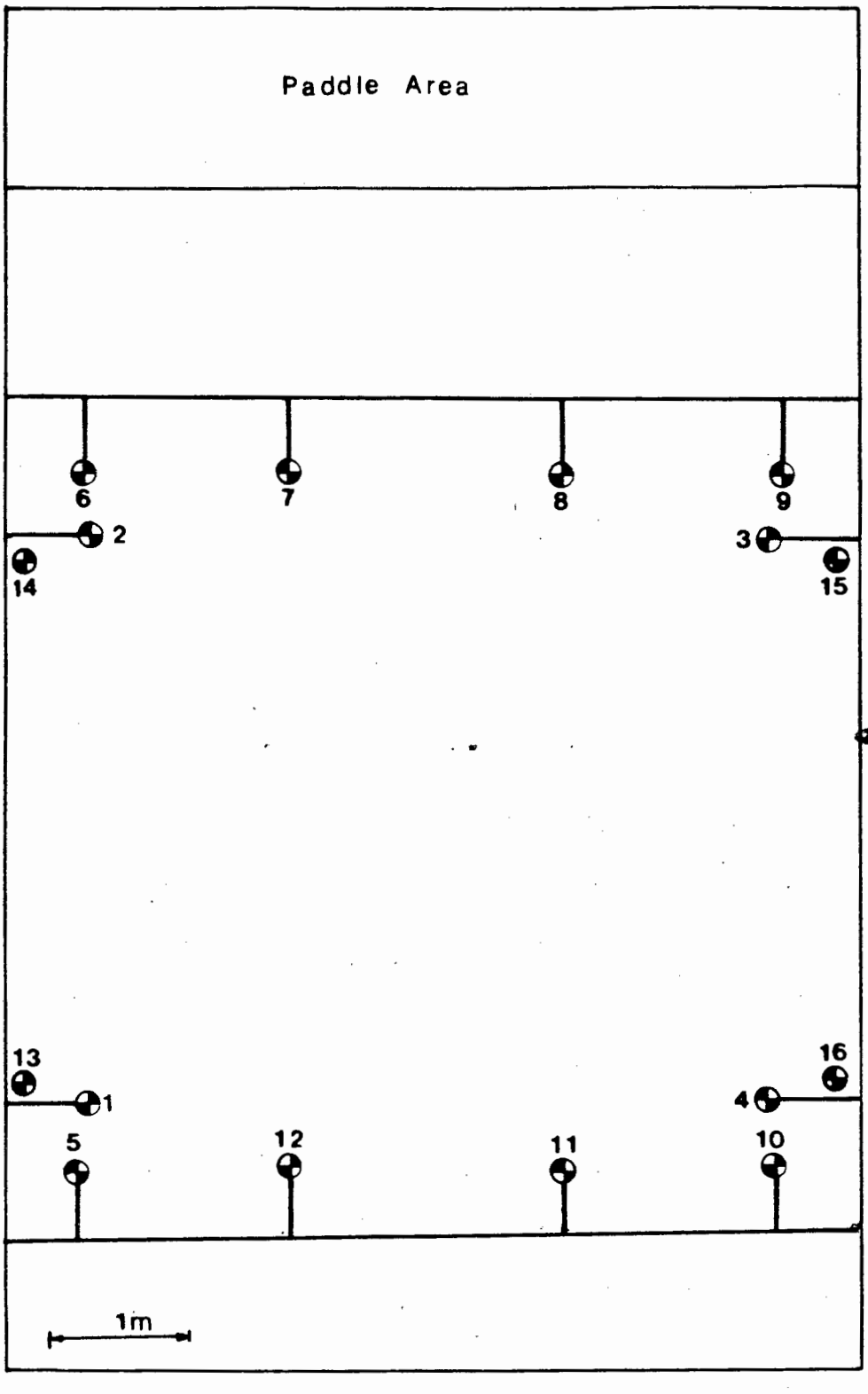

Fig. 5.7: 16 point wave basin configuration

Each target consists of an illuminated plastic cylinder onto which a quartered black and white circle is fixed in position.

To obtain the X, Y, Z ground co-ordinates of the control points, the following measurements were taken. The Z ordinates were calculated using the mean result of 3 levelling surveys. A Wild automatic level was used in conjunction with a steel ruler, and the position of the level was altered for each of the surveys. The plan (X, Y) co-ordinates were calculated using a least squares adjustment program written by Prof. H. Rüther of the Department of Surveying. Some 62 inter-control point distances were measured and reduced to equivalent plan distances using the Z elevations of the control points.

The X co-ordinates were calculated within a 68% probability of being within $\pm$ 1.039 mm of their true values, while the Y co-ordinates were located with a 68% probability of being within $\pm$ 1.13 mm of their true values. The Z co-ordinates were estimated to be within $\pm$ 0.3 mm of their true position, the results being more accurate than the plan co-ordinates. Thus the XYZ co-ordinates were estimated to within 1.13 mm. The determined ground control co-ordinates are given in Table 5.1. The plan positions are shown in Fig. 5.9.

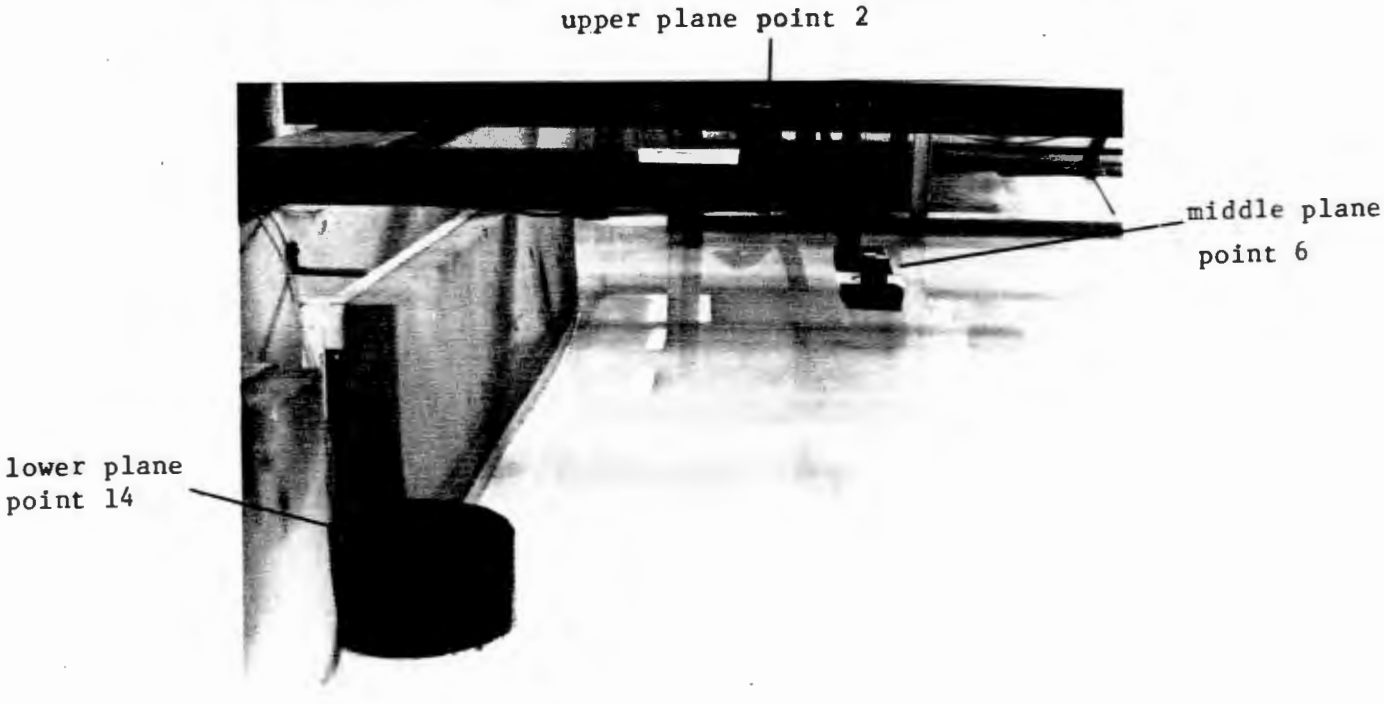

Fig. 5.8: 3 level control points

Table 5-1: Control point co-ordinates

Point No.	X	X	Z
1	0,527	0,670	0.485
2	0,521	4,683	0,488
3	5,577	4,680	0,484
4	5,581	0,654	0,498
5	0,740	0,108	0,260
6	0,670	5,252	0,265
7	2,105	5,198	0,274
8	4,028	5,264	0,278
9	5,406	5,238	0,281
10	5,427	0,089	0,281
11	3,901	0,085	0,271
12	2,075	0,149	0,264
13	0,175	0,765	0,000
14	0,176	4,578	0,003
15	5,917	4,576	0,010
16	5,915	0,780	0,000

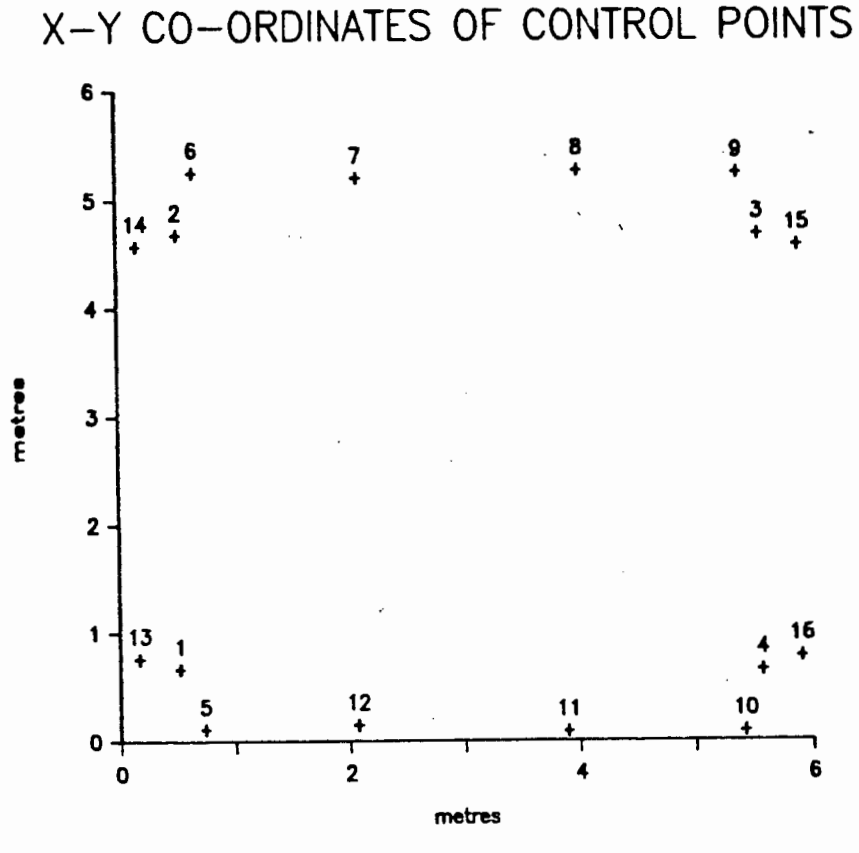

Fig. 5.9: X, Y plan co-ordinates

5.6 The technique for wave height and pattern measurement using the stereocomparator/micro-computer system

A brief description of the sequence of operations to obtain a final countour of the ship's generated wave pattern is given. A complete description is to be found in Pos (1984) and Pos and Kilner (1982) for the analysis of two pairs of stereophotographs.

A diagrammatic representation of the process is shown in Fig. 5.10. The stereopair is analysed on a Zeiss stereocomparator interfaced to an Hewlett Packard 9816. The computer stores all observed data on disk and calculates the XYZ co-ordinates of each observation point, using a program utilising the theory of projective transformations. The edited XYZ data is then sent to the mainframe UNIVAC 1100 for interpolation and processing to obtain a contour plot and a 3-dimensional perspective view of the wave basin water height distribution.

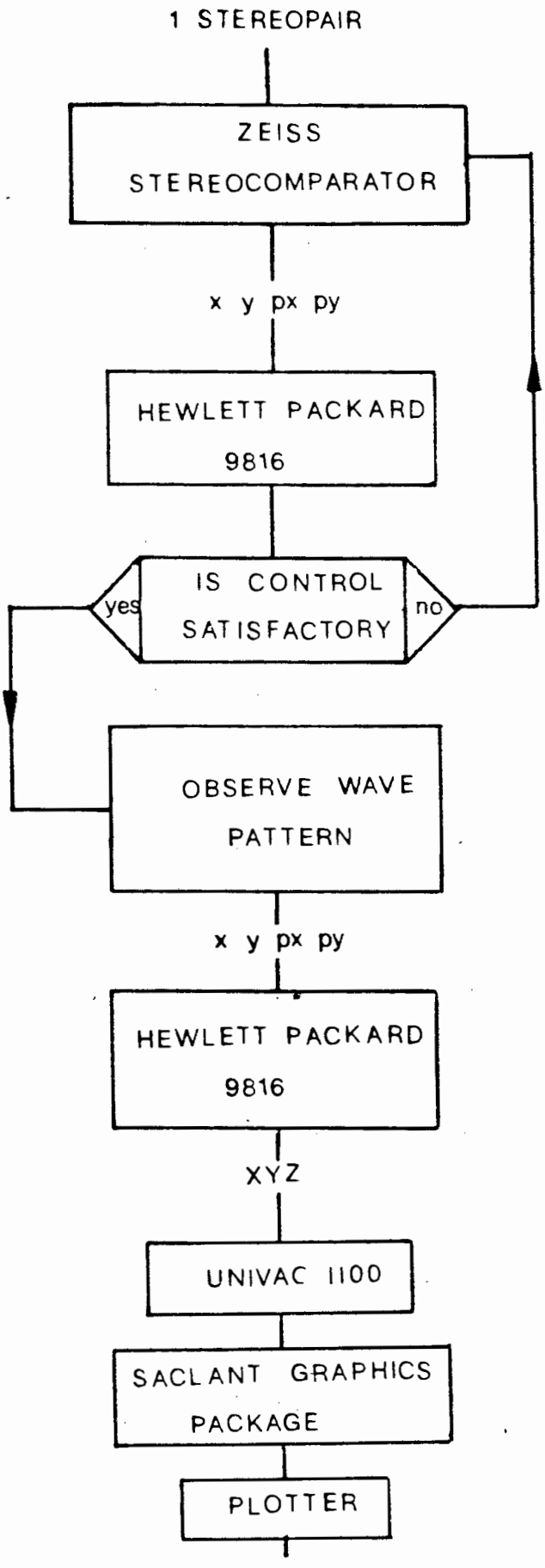

Fig. 5.10: Sequence of stereopair analysis

5.7 Close range photogrammetry versus conventional measurement techniques

The general advantages of using close range photogrammetry as a measurement technique are (Atkinson 1980):

(i) the object is not touched during the measurement;

(ii) data acquisition is rapid;

(iii) the photographs store semantic and metric data with high density;

(iv) rapid deformation and movement is measurable;

(v) parameters such as velocity and acceleration can be determined;

(vi) evaluation of the photographs can be done at any subsequent time and repetition and amendment are always possible;

(vi) photography and methods of evaluation are flexible and can be modified to meet specific requirements, e.g. accuracy;

(viii) complicated shapes are easily measured;

(ix) continuous contouring of irregular surfaces is possible;

(x) analytical methods of evaluation provide means of integration with succeeding calculations and data handling.

The major limitations of the photogrammetric procedure are:

(i) the need for specialised equipment and the cost of such facilities;

(ii) the result is not immediately available as time is needed for processing;

(iii) the object must be both suitable and in a position to be photographed;

(iv) the need for adequate ceiling height for positioning of the cameras.

These drawbacks can be limited by the use of non-metric cameras and less efficient analysis procedures, such as those evaluated by Pos (1984). However, all photogrammetric applications to a certain extent require data reduction equipment, the cost of which might only be considered by large Hydraulic Research Institutions.

Many institutions prefer to use the conventional method of wave height measurement, resistance or capacitance type wave probes. Limitations are as follows:

(i) These probes are mounted at fixed positions in the towing channel and record only the wave elevations at a pre-determined position for each ship run. The position of the probe can be moved and record further sailing profiles for additional ship runs. Yokoo (1976) adopted such a technique for the measurement of the wave pattern of a 23,5 m model.

(ii) The system is time consuming as several runs have to be made.

(iii) Regions of maximum wave heights and local disturbances may be overlooked, depending upon the position(s) of the probe(s). Sorenson (1968) used wave gauges to record sailing line profiles of ships manoeuvering in channels and restricted waterways.

These problems are largely overcome by the use of photogrammetry. Stereo photographs can be taken in a much shorter time period than several ship runs required for a complete wave pattern using probes. The negative plates contain all the relevant information and local areas of interest can be evaluated. Most importantly, the wave pattern is free of probes and measuring equipment allowing for a fully undisturbed surface.

6. EXPERIMENTAL WORK

6.1 Introduction

It was the author's primary intention to investigate the generated wave pattern of a moving vessel and from these observations to determine the wave resistance of the ship, using the proposed energy analysis procedure given in Section 4.6. This method was to be validated against other past experimental works over a range of Froude numbers.

The author was interested in finding the total model ship resistance curve. Further measurement of the squat, trim and hull wave profiles were also taken. These measurements necessitated the adaption of the existing 3-dimensional wave basin at UCT Civil Engineering laboratory to specific towing tank requirements for model ship testing.

The following chapter describes the adaption of the wave basin, choice of model ship, towing system employed and force measurement procedures. The wave energy analysis is discussed.

6.2 The wave basin

6.2.1 The wave absorption surround

The existing wave basin configuration had to be modified to accommodate the variations of water depth in the range 125 mm - 600 mm. The effective, undisturbed water area from basin wall to wall is 45,8 m^2. In order to prevent wave reflection off the walls there was a sloping gravel surround on the three walls opposite and adjacent to the wave paddle. This surround could only accommodate a water depth of 125 mm and reduced the effective water area of the basin to 32 m^2. If one were to utilise a similar surround for water depths of 500 mm - 600 mm, the surface area would reduce to approximately 16 m^2.

This surround is ideally suited to wave diffraction experiments at a fixed depth; however, because the water depth needs to be varied for ship modelling experiments, an alternative absorption surround had to be used. This surround would have to incorporate the following functions:

(1) It would not be required to absorb large amplitude waves generated by the wave paddle, but smaller oblique waves generated by the moving ship;

(2) there would have to be as large a water area as possible to accommodate the diverging wave patterns generated;

(3) be useable in all water depths in the 125 mm to 600 mm range;

(4) be as simply adjustable as possible.

Bearing these conditions in mind, the following alternatives were proposed:

(1) A sloping, perforated wooden beach at inclinations of 1:2 and 1:3 which could move vertically.

(2) A 50 mm foam rubber surround glued onto the wall.

(3) A 50 mm foam rubber surround mounted on a plastic mesh and spaced 50 mm away from the wall.

6.2.1.1. The **wave flume**

The wave flume (fig.6.1) used for testing these surrounds had a width of 300 mm and a length of 5,28 mm and was equipped with a variable speed wave generator. One end of the flume was blocked with a 10 mm plywood board to simulate the basin wall. In order to measure the wave amplitudes, a floating buoy was used which could move vertically only. The vertical movements were amplified by a factor of four and read off a mounted scale.

In order to evaluate the performance of each surround it was decided to test each in the following manner:

(1) Position the surround to be tested onto the vertical wall.

(2) Run the wave paddle at the same period and water depth for a set amount of time.

(3) Stop the wave paddle in the vertical position and record the time it takes for the marker buoy to oscillate within $\pm$1 mm of the mean water level.

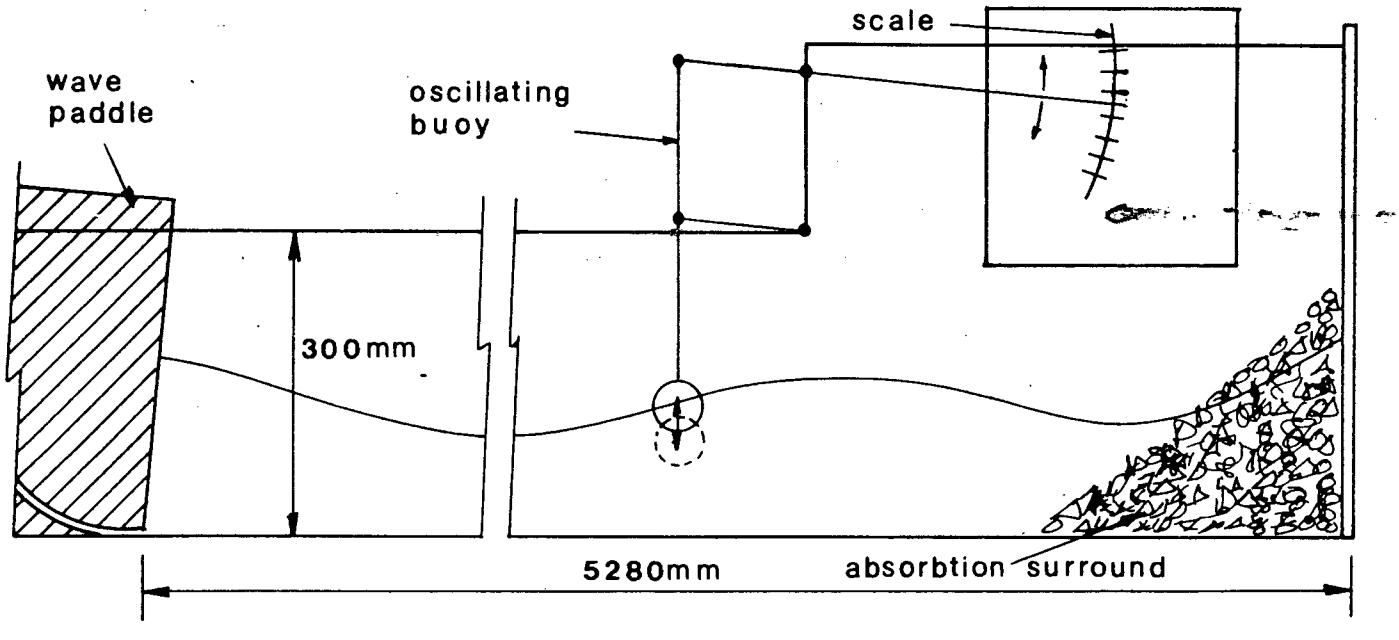

Fig.6.1: Wave flume

For each alternative surround the wave period, water depth and time of wave generation were constant. The only variation in the flume was the wave absorption beach and therefore the time it took for the marker bouy to oscillate within the range was a direct quantitative measure of the effectiveness of each surround. For each absorption surround a series of tests were performed.

As a measure of the effectiveness of each surround, the original gravel beach was tested for use as a relative frame of reference. From the results, the shoaling beach at 1:3 was the most efficient solution, and the 50 mm foam wall the least efficient. There was little difference between the 1:2 shoaling beach and the spaced foam surrounds. The gap between the wall and the foam improves upon the "foam only" surround as it allows the absorbed wave to decay by reverberating back and forth between the wall and the foam.

Quantitatively the shoaling beach was more efficient than the spaced foam by a margin of some seven percent. The beach could have been constructed to move vertically up and down the basin wall, but this would have involved a fairly heavy and awkward support frame which would have to be adjusted for each variation in water depth. The foam could be supported on a light frame and constructed the full height of the basin wall. Once in position the surround could then be used for any water depth without further re-adjustment.

Thus, although the shoaling wooden beach was more efficient, the practical difficulties in constructing such a surround are outweighed by the simplicity of construction of a foam surround spaced 50 mm from the wall. If there was a large improvement in wave absorption, say at least 25%, over the foam surround then the wooden beach would have been used. The foam surround satisfies the original objectives mentioned previously, viz:

(1) It is capable of absorbing the ship generated waves.

(2) It does not encroach on the available water surface area.

(3) It is usable in all water depths.

(4) It needs no adjustment once installed.

On the basis of the above results the wave absorption surround installed in the wave basin consists of a 50 mm layer of foam rubber mounted on a plastic mesh and spaced 50 mm away from the wall to cover the water depths from 125 mm to 600 mm.

6.2.2 Basin floor level

Previous experimental work by Pos (1984) required the water depth to be as consistent as possible throughout the entire basin floor area. Through an extensive levelling procedure, the basin floor was levelled to within $\pm$ 1 mm of the required level. The finished surface consisted of a layer of epoxy resin over the concrete base.

At the beginning of this experimental survey, there were several areas of epoxy resin that had separated from the concrete floor due to water seepage. This resulted in large epoxy 'bubbles' or rises forming at several positions across the basin floor. These areas were ground down using a hand held floor grinder, filled in and smoothed over with a cement grout mixture. Thus the basin floor was as consistently level as possible and therefore the water depth uniform throughout. This reduced or excluded any deviations in the ship generated wave pattern due to possible refraction or other interference with the seabed.

6.3 Appropriate hull form

6.3.1 Choice of ship

The 1979 Conference on Ship Wave Resistance Computations held at Bethesda, Maryland, USA in 1979, presented results for five different ship forms, namely:

(1) Wigley Parabolic Hull

(2) Inui Hull S201

(3) Series 60, C_B = 0,60

(4) HSVA Tanker

(5) Athena High Speed Hull

The Wigley and Inuid hulls are mathematically defined forms, thus allowing for direct computational analysis of wave resistance using the analytical theory. The Wigley hull is of the thin ship format, having a fairly low wave resistance and thus generating relatively small waves. The Inuid has a high wave resistance and operates at Froude Numbers of up to 0,65. The Series 60 operates at lower speeds and in terms of wave making resistance, lies somewhere between the Wigley and the Inuid hull. The HSVA tanker is a full ship form with high viscous pressure drag and probably a high degree of wave breaking. The wave resistance would thus be composed of both those resistances, derived from wave breaking and wave pattern measurement. The high speed hull, Athena, operates in the higher Froude number ranges and there is relatively little data available on the resistance components of this form.

Due to the available towing distance on the wave basin, it would be undesirable to operate at the very high speeds required for Athena and Inuid hulls. As mentioned, the Wigley generates relatively small amplitude waves and the HSVA Tanker has a large wave breaking

resistance component. The Series 60, C_B = 0,60 hull form has been widely used for many years as an alternative to a mathematical form, as it dimensionally resembles an operational vessel. The operating range generally varies between Froude numbers of 0,15 to 0,40. A large amount of data is available on the Series 60. This includes both the mathematical formulation of Gadd (1972), Noblesse (1984), Nakatake et al (1979) and the experimental results of Ward (1963), Tsai (1975) and Moran (1972) and others.

Owing to the experimental nature of this investigation, it was desirable to be able to compare results with findings previously published. The quantity of data available combined with the proposed method of evaluating wave resistance from the wave pattern, made the Series 60 the first choice of hull form to be used. This allowed for direct comparison with established results.

6.3.2 Appropriate ship dimensions

To evaluate wave resistance from the wave pattern it is desirable to have deep water conditions throughout. Effects due to shallowing water, such as changes of particle orbit velocities, profiles and surface profiles (sinusoidal to trochoidal) could interfere with the results, possibly causing an increase in wave resistance, due to additional squat in shallow water. For deep water conditions it is required that the depth of water must not be less than half the wavelength (section 3.4.3.1) ($^d/_L \geq 0,5$). Blevins (1984) states that the effective wavelength of a ship is 0,9LWL.

Within the confines of the wave basin, the water depth could be a maximum of 650 mm. At more than 450 mm the water level rises above the wave generator. The practicable deepest depth was found to be 500 mm, not flooding the wave generator, and allowing for sufficient clearance along the basin surrounding walls.

For a water depth of 500 mm the wetted length of the model could be determined. The maximum LWL for d/L = 0,5 is 1,111 (for L = 0,9LWL). On the basis of this result a length of 1,080 m was chosen allowing a small margin of confidence. This gives a d/L ratio of 0,514.

The model was based upon the specifications given in the 1979 conference on ship wave proceedings. The table of offsets for the Series 60, C_B = 0,60 and the body plan are given in Appendices 6A and 6B.

The dimensions and form coefficients of the model used are as follows:

LWL = 1,080 m
L_{pp} = 1,062 m
B = 0,148 m
H = 0,057 m
V = 5,393 x 10^{-3} m^3
C_B = 0,602
C_{PR} = 0,614
C_x = 0,977
C_s = 0,710

6.3.3. Construction of model

The model was constructed by the author in the civil engineering workshop at UCT. To accommodate instrumentation in the hull a hollow model was required. Various construction methods were initially considered, the final choice being the traditional ship cold moulded or planking technique. Body sections were shaped from 5 mm thick marine plywood for 20 sections between the FP and the AP. These were securely fixed onto a central stringer, 10 mm wide, giving longitudinal strength and rigidity. The bow and stern sections were shaped from solid vertically arranged Jelutong (a soft modelling wood) transverse body plans. These were hand sanded to accomodate the areas of tight curvature in these regions. Fig. 6.2 demonstrates the modelling technique used. Planks were cut and shaped 1,5 mm thick and 5 mm - 10 mm wide. These were glued onto the body sections and assumed the natural required curvature. Areas of tight curvature were steamed beforehand to accomodate a smoother fit. The hull was sanded down and coated with resin and four layers of hard lacquer based spray paint, each layer being finished to a high degree of smoothness using fine water paper.

The interior of the hull was coated with glassfibre matting for waterproofing and additional strength. Some 4 kg of paraffin wax was used to obtain the correct waterline and trim state. For photographic contrast purposes the hull and interior were painted matt black.

A brass towing attachment was positioned on the stern section to allow for several towing heights. The towing line was fed through a brass guide mounted on the bow, as in Fig. 6.3. Two white targets were positioned on the bow and stern sections 750 mm apart. These were used for various measurements taken off the photographic plates and for squat and trim determination. To trigger the photo electric camera firing circuit, a black perspex plate, Fig. 6.3, was mounted vertically on the stern. This broke the light beam when the model was approximately three quarters of the way across the wave basin.

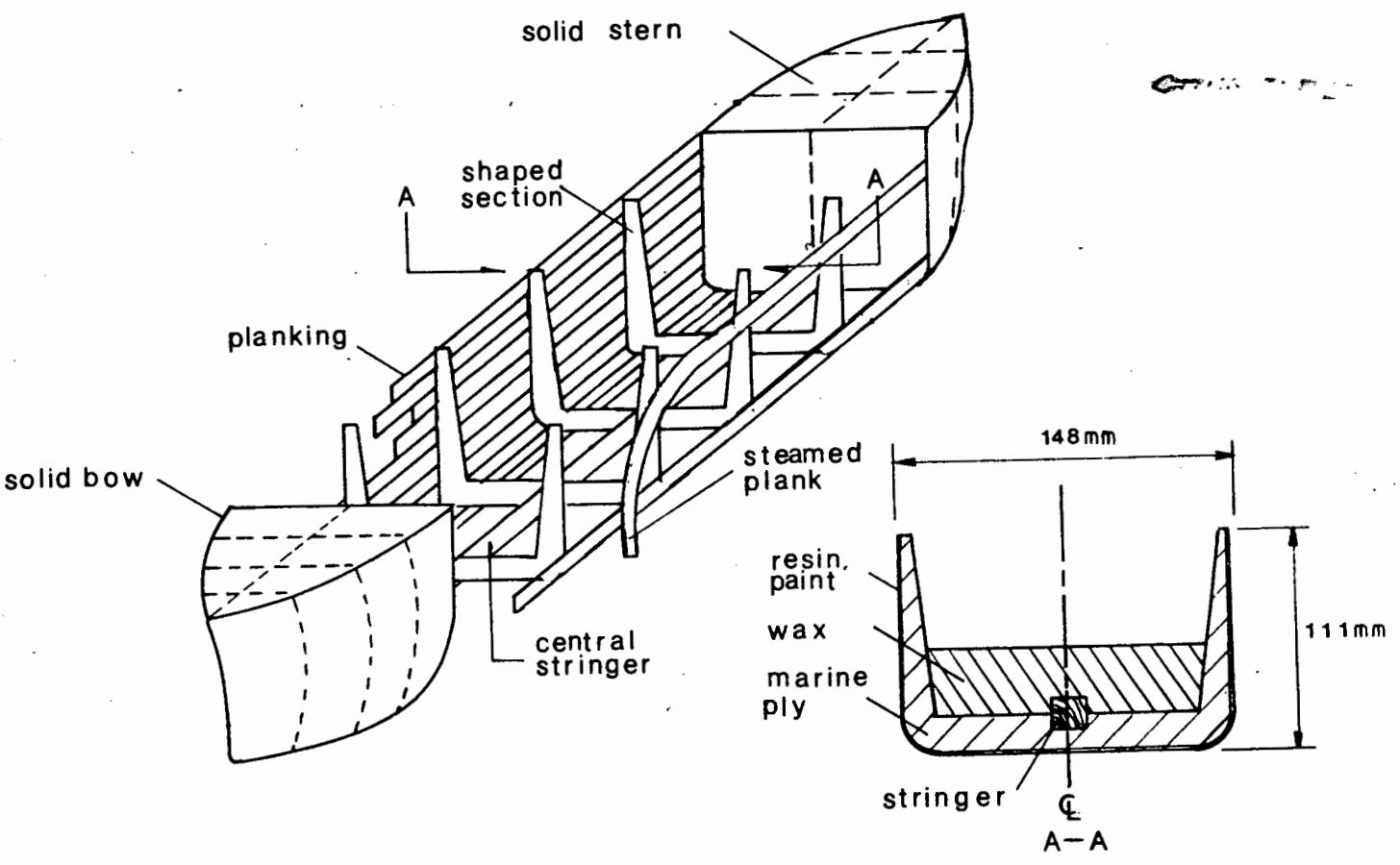

Fig. 6.2: Model construction technique

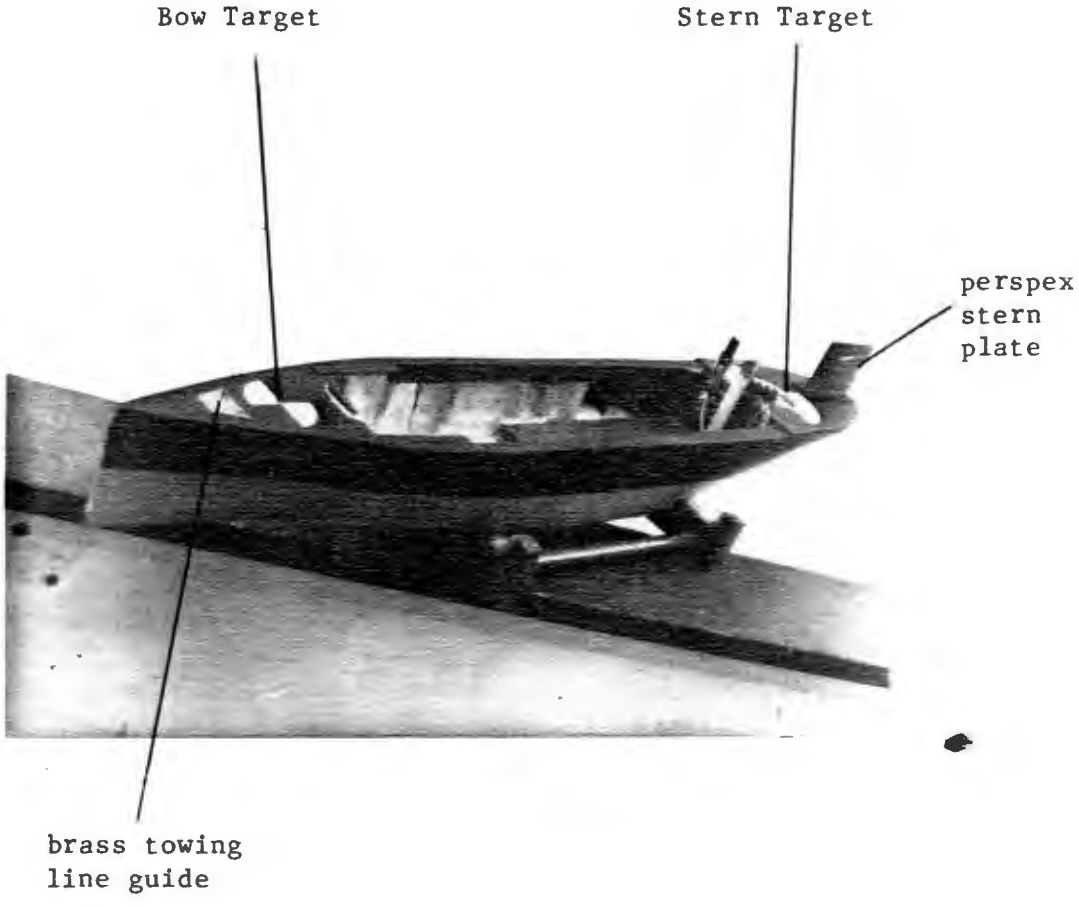

Fig. 6.3: Series 60, C_B = 0,60 model

6.4 Model towing system

The basin configuration in Fig. 6.4 gives the basic dimensions of the area and shows the illumination limits of the overhead projectors and flash system. If the model were to be towed straight across the wave basin, the length of run would be approximately 8 m. To increase the length, it was decided to tow the model diagonally across the basin from start (A) to end (B). This increased the distance to 10,5 m, allowing a longer steady state run.

As discussed in section 4.2, there are essentially two means of determining total resistance curves of a model in a towing tank, viz:

(i) falling weight principle;

(ii) towing trolley and dynamometer.

Due to the configuration of the basin, a trolley type apparatus was impracical, and for photographic requirements the model had to be visible from above. Various towing methods were considered, each involving some means of determining the total resistance of the model at the required range of Froude numbers.

6.4.1 Falling weight principle

This approach generally used in smaller towing tanks where no towing carriage exusts and rapid acceleration is required. Adapting this method to the wave basin has both advantages and disadvantages. The advantages are as follows:

(i) Force measurement inherent in the system. When acceleration is zero, then $R_t = W$.

(ii) Rapid acceleration promotes turbulence stimulation.

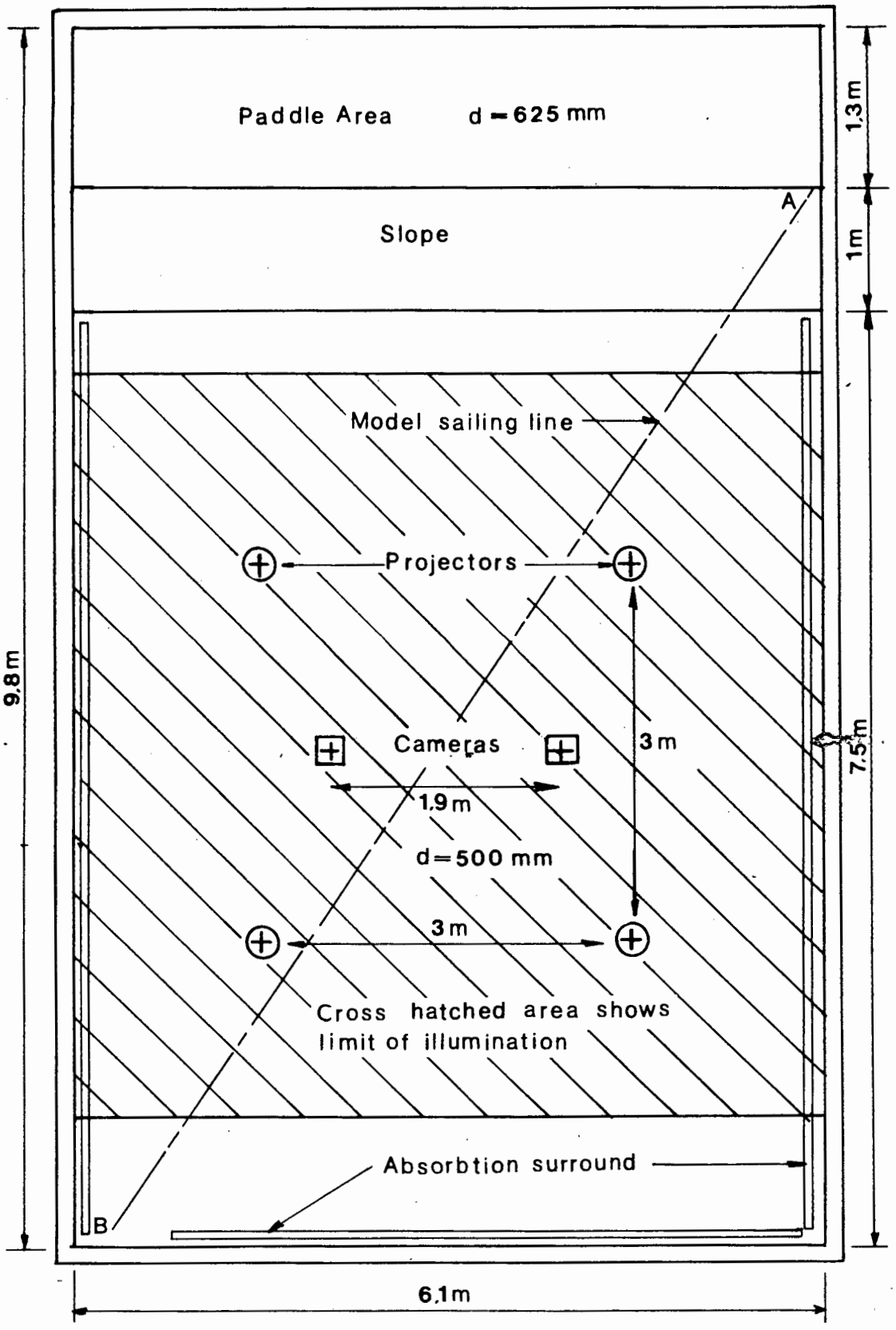

Fig. 6.4: Wave basin configuration

The disadvantages are:

(i) Velocity has to be determined independently.

(ii) Sufficient ceiling height is needed for the weight to fall freely.

(iii) A sufficient length of model run is needed to achieve the steady state required for advantage (i).

6.4.2 Motor driven systems

The concept of a motor driven towing system is similar to that of a towing trolley. The advantages of this concept are as follows:

(i) Velocity is pre-selected and measurable.

(ii) Steady state can be quickly achieved.

(iii) Frictional losses (such as over pulleys) can be kept to a minimum, depending on approach used.

The disadvantages are:

(i) Drag Force needs to be determined.

(ii) Suitable mechanised apparatus is necessary.

(iii) Instrumentation for force measurements is required.

Various motor driven systems were therefore considered.

6.4.2.1 Motor drive/contiuous line

This system involved a continuous line fixed to the model and circulating via a pulley system over a winding drum. A cantilever would be positioned at one of the pulleys, the force on the cantilever thus

representing the force on the model. This would have to be interpreted using a resistance strain gauge assembly and data acquisition unit. The model would reach a steady state almost immediately as the diameter of the winding drum would be fixed. To overcome violent variations in model speed at this stage, the pulley and continuous towing line would have to be extremely taut and thus the system would contain high frictional losses.

6.4.2.2 Motor drive/single line/spring balance

Utilising a single towing line attached to the model would reduce the frictional losses of a continuous line. A spring balance could be fixed in the model onto which the towing line could be attached. This would be a direct measure of the force in the towing line. The spring balance could be read off the stereophotographs, and a permanent force record is available. To uniformly accelerate the model from rest to a steady state could be achieved using a drum of slowly increasing diameter or 'snail-drive'. The model would have to be held at rest before the start of each run, necessitating the construction of a special 'mooring' facility.

6.4.2.3 In-line force measurement/load cell/data acquisition unit

Using either a single or continuous line, a load cell could be attached to the model at the point of towing. The force is a direct measure of the ship drag and neglects frictional losses associated with a continuous line. Problems arise in transferring the load cell readings from the model to a suitable data acquisition unit outside of the wave basin, either a micro-computer or X-Y plotter.

6.4.3 Choice of method

The falling weight system was rejected because of the extremely short towing distance available. It was uncertain whether a steady state could be achieved over this length and to determine at what point this occurred would necessitate several timing gates along

the ship sailing line. The pulley frictional losses would need to be taken into account, requiring additional measuring equipment.

The concept of a motor driven system was adopted due to the direct velocity determination and the possibility of reaching a steady state fairly rapidly. The motor drive/continuous line system has the advantage of forward and reverse capabilities, but the frictional losses due to the tension in the towing line are dificult to determine. This system was rejected because of the high frictional losses involved.

The spring balance method was used for ease of measurement and the permanent record concept. The resolution of the scale on the photographic plates was not a problem, as the stereocomparator enlarged the image sufficiently. Only at those speeds for which stereopairs were taken could the force be measured so an alternative system was needed. A load cell/data acquisition unit system was used to obtain data for a longer speed range. Section 6.3.3.2 gives more details on the force measurement.

6.4.3.1 Construction of towing system

Both methods chosen needed a single towing line and smooth acceleration phase to achieve a steady state. A variable speed 3-phase motor was used as the main driving mechanism. This had an adjustable gearbox allowing for a range of 20 - 100 r/min. The speeds required for the model ranged from 0,651 m/s to 1,627 m/s corresponding to a range of Froude numbers from 0,2 to 0,5. Using these speeds the size of the required winding drum can be calculated from the relationship between r/min and ship velocity, given by Eq. 6.1.

$$\text{r/min} = \frac{\text{Velocity} \times 60}{\pi \times \text{diameter of winding drum}} \qquad \text{(Eq 6.1)}$$

Therefore at the maximum operating speed of the motor, the required drum diameter to achieve the higher Froude number range is of the order of 300 mm. This would be impractical to construct so the

motor speed range had to be increased. The replacement of the gearbox was found to be too expensive so an alternative belt driven system was used.

A 150 mm alloy belt driven pulley was fixed on the spindle of the motor (Fig.6.5). This could be connected to a choice of smaller pulleys ranging from 50 mm to 125 mm. These were connected to an axle mounted on roller bearings onto which the winding drum could be placed. The speed of this axle could be altered to vary from 24 to 300 r/min depending upon the pulley combination and motor speed selected.

Using a speed of 300 r/min the winding drum diameter could be as small as 100 mm. A diameter of 130 mm was used, thus increasing the range if necessary.

The winding drum was constructed by shaping on the lathe and using a vernier scale to obtain an accuracy of 0,2 mm. The drum was 230 mm in length, the end 140 mm being conical-shaped, the total angle of the apex being 50°. The cone was grooved using a special cutting tool to accelerate the model from rest to a steady state over a distance of 1,5 m.

Figs 6.5 (overleaf) represents the motor drive and towing system. The motor was bolted onto a specially designed steel support rig and was capable of moving 80 mm in the X-X direction. The winding drum and variable speed pulley axle system was mounted on a rigid steel channel section anchored to the basin side wall. The axle could move some 80mm in the Y-Y direction. This combination of movements meant that either pulley could be used, each utilising a single belt drive.

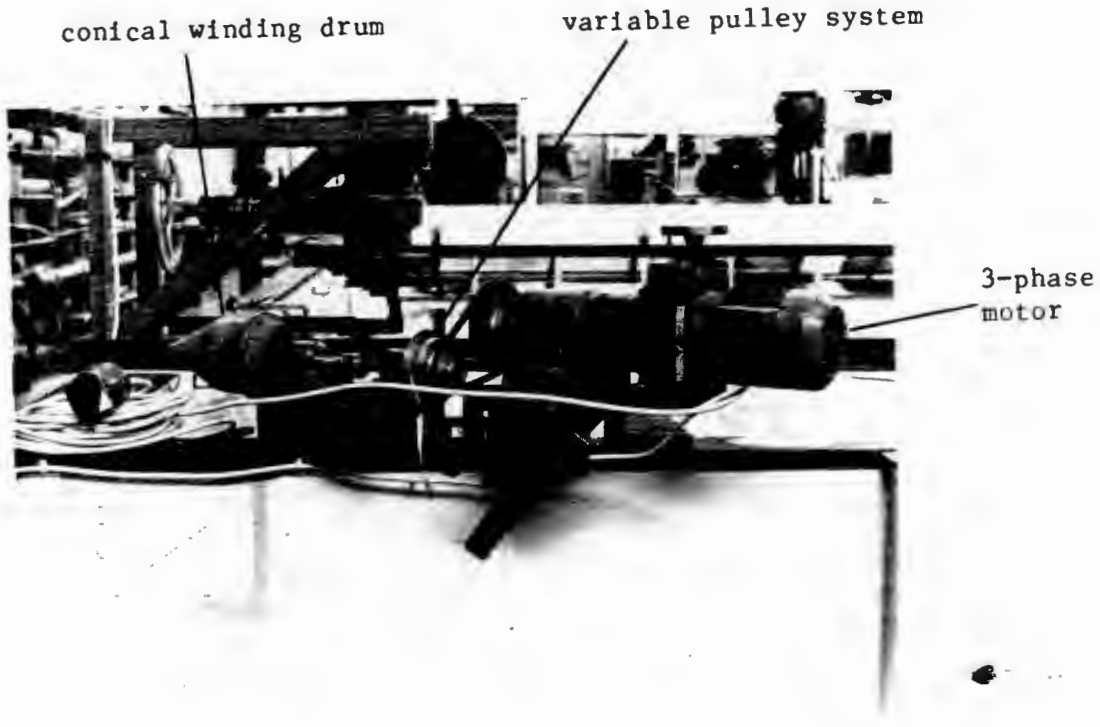

Fig. 6.5: Motor driven towing system

6.4.3.1.1 Determination of velocity

The revolutions of the winding drum and axle were measured using a manual counter placed at the midsection of the two bearings. An offset camshaft was shaped so as to activate the counter once every axle revolution. Using a stopwatch the number of revolutions over a time period of 4 - 6 minutes could be recorded. The r/min calculated in this manner is extremely accurate. A maximum error of one revolution is possible due to the starting and finishing positions of the camshaft. An error of one revolution over a 5 minute period results in a 0,2 r/min error. This represents less than a 0,5% error when determining the velocity of the ship.

6.4.3.2 Force measurement

The total resistance of the model was estimated beforehand based upon the results of the wave resistance coefficient as found by Tsutsumi (1979) and using the Schoenherr friction line. A Salter Geo spring balance capable of reading up to 10 N was used. The scale was graduated at 0,1 N intervals. When using the stereocomparator, the scale was large enough to be able to read the drag force.

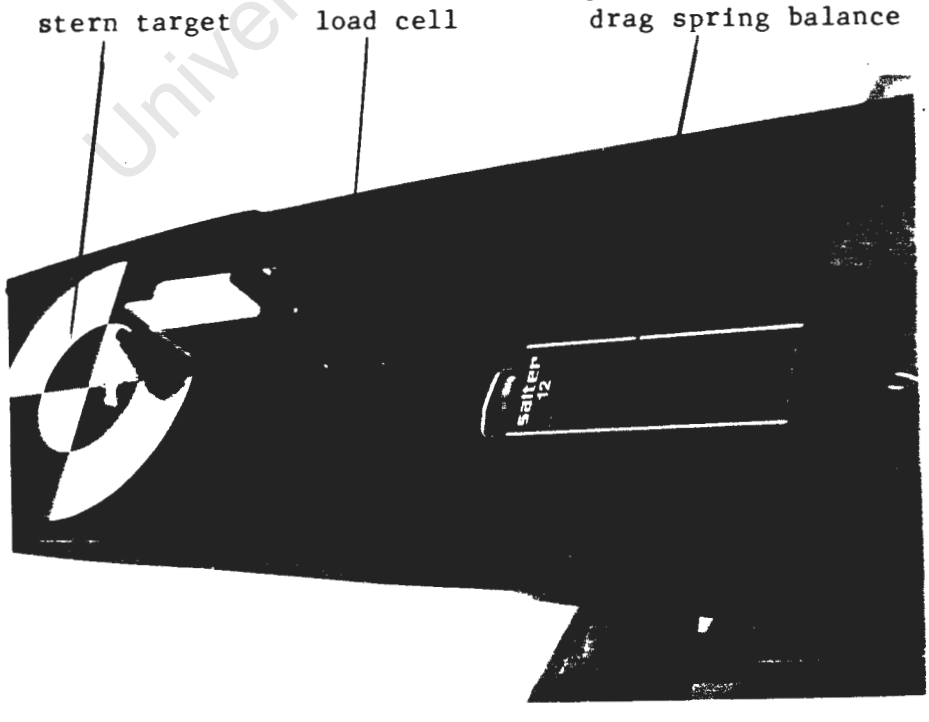

Fig. 6.6: Force measurement using spring balance or strain gauge type load cell

The alternative force measurements were done independently of the photographic runs. A load cell consisting of a spring steel cantilever was mounted on an aluminium support bracket at the rear of the hull. The strain gauges were placed as near as possible to the fixed end of the cantilever, the region of highest bending. Fig. 6.6 illustrates the strain gauge and spring balance used.

The resistance strain gauge bridge was connected to an X-Y plotter which recorded the variations in voltage across the load cell. The X scale was time dependent, the carriage moving at a constant rate across the board. The Y scale recorded the voltage variations. Before each test run the load cell had to be calibrated. A known weight was attached to the load cell and the curve plotted on the chart recorder. This was repeated for several weights, although this is not essential as the strain vs applied load is linear. The resultant plot of the towing force could thus be measured relative to the calibrated curves, as in Fig. 6.8.

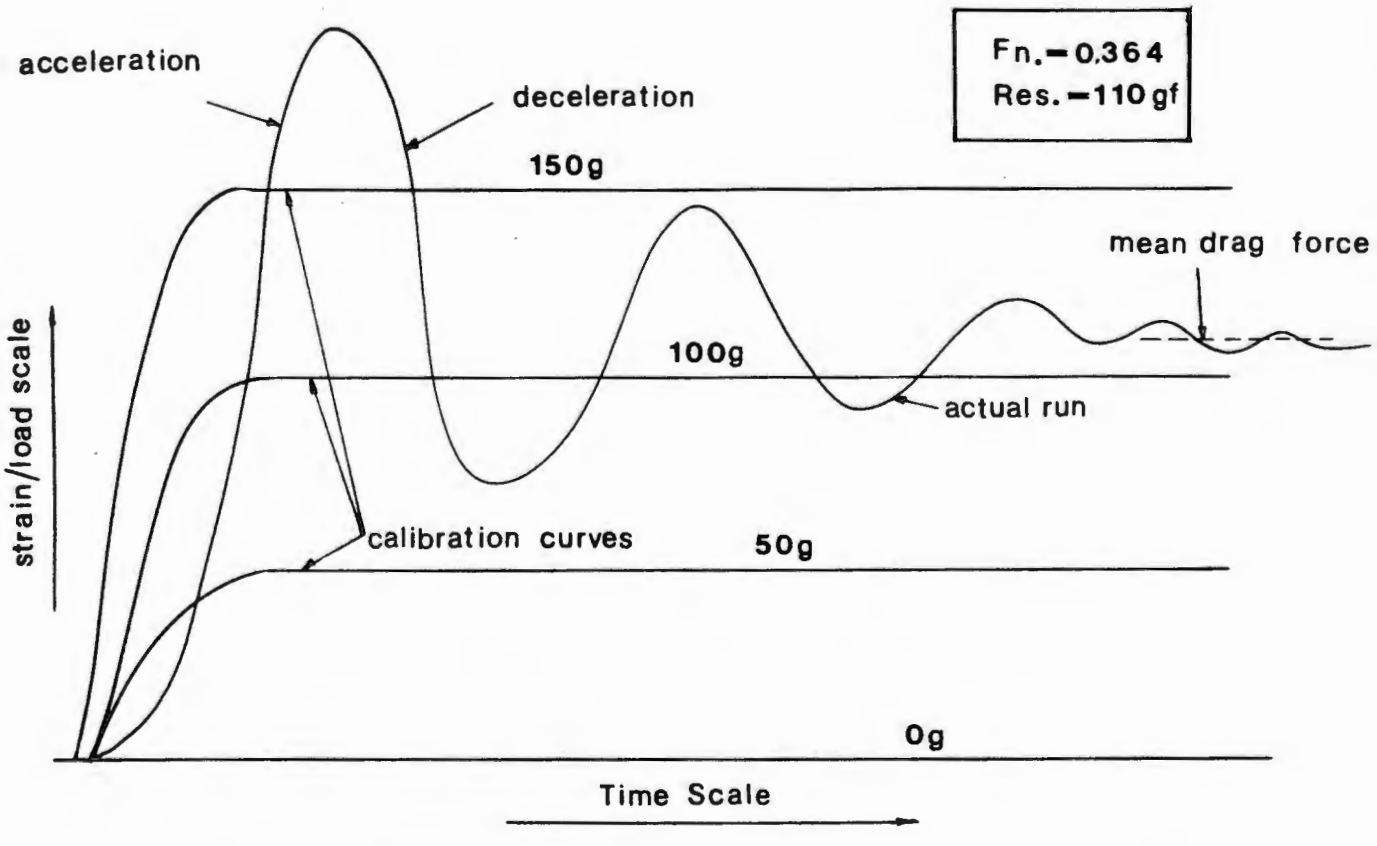

Fig. 6.7: Typical resistance vs time output curve

The connecting 4-core cable from the load cell to the data acquisition unit was fixed to a Teflon runner. This could slide freely on a taut nylon coated stainless steel wire 1 m above the line of ship travel. The cable was suspended from the ceiling above the centre of the basin and then linked to the plotter. Fig. 6.8 illustrates the cable linked to model via the Teflon runner. No interference with the model is observed.

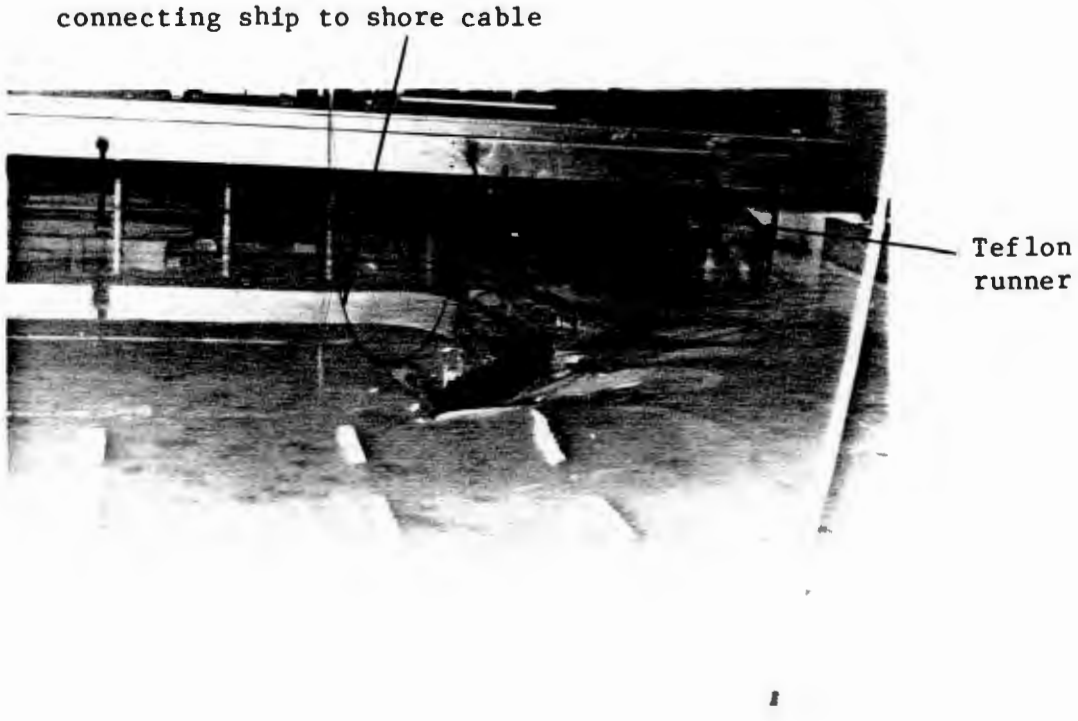

Fig. 6.8: Single line towing system with suspended cable from load cell to data acquisition unit

The total towing force for the model was measured using this method for the range of Froude numbers 0,280 - 0,500. 62 runs representing 22 speeds were recorded. Where results for the same speed were taken, the final resistance was taken as the mean value.

The measured resistance for each run was taken as the mean value of the oscillations shown in Fig. 6.7. The oscillations are due to the damping of the acceleration-deceleration initial curve. If the basin were a longer length the oscillating nature would diminish to the mean value as the load cell stabilised. The analysis of these results is fully discussed in Chapter 7.

6.5 Photogrammetric work

6.5.1 Experimental procedure

The experimental photographic work can be split into a daytime and night-time preparation and experimentation procedure.

A. Daytime procedure

The daytime preparation procedure was as follows:

(1) The wave basin was initially filled to a depth of 500 mm. To obtain the correct oil/water concentration to achieve the photographic contrast specified in Section 5.4.4.2, 220 litres of Shell Dromus B cutting oil were added to the water. Before each series of test runs the water depth was checked and topped up if necessary.

(2) The model and towing apparatus were carefully checked several times at the chosen speeds to be analysed that night.

(3) The camera firing unit, flash system and control lights were tested for any faults. The cameras were levelled using a precise spirit level to ensure that the glass negatives would lie parallel to the water surface to reduce orientation and parallax photogrammetric errors.

B. Night-time procedure

(1) The water temperature was measured to be used for Reynolds scaling if large temperature variations were present over the test period.

(2) The model speed was checked as described in Section 6.3.3.1.1 and several runs were performed.

(3) The control point lights, photo electric camera firing circuit and flash circuitry were switched on. The cameras were loaded and the correct plate numbers selected. These numbers are imaged on the negatives and identify the steropairs taken.

(4) All lights in the laboratory were switched off to ensure maximum darkness.

(5) The model was started using the remote hand held motor switch. As the stern plate passed the photo electric beam, the camera system activated the flash circuitry and the stereopairs were taken.

The stereopairs were than analysed using the stereocomparator/ microcomputer/projective transformation theory system described by Pos (1984) and, briefly, in Section 5.6.

6.5.2 **Froude number range**

Stereopairs were taken at 23 different Froude numbers ranging from 0,22 to 0,50. Due to either camera misfiring or incorrect flash-lighting, 3 sets of plates were incorrectly exposed and unusable. 20 pairs were analysed on the stereocomparator to varying degrees of completeness. Measurements of the bow and stern target levels were obtained for all cases, allowing for the determination of squat and trim. The readings of the ship drag were recorded in most instances, except for those where the spring balance scale was obscured by possibly a chemical stain from the plate development or an excessive shadow caused by the orientation of the vessel or overhead random projected patterns. This occurred for only 3 of the 20 speeds. The wave pattern in the near field was observed for all speeds except for those where the entire wave pattern was analysed (Table 6.1). Due to the symmetry of a ship generated wave pattern only half of the wave field is plotted, in line with other research and publications of this nature. One case (Fn = 0,389), was observed in the near field on both sides of the hull and was found to be suitably symmetrical.

Table 6.1: Stereopairs analysed

Froude number	Observed total wave field	Observed near field only	Wave Energy Analysis
0,497	*	-	-
0,478	-	*	-
0,461	-	*	-
0,441	*	-	*
0,431	-	*	-
0,422	-	*	-
0,407	*	-	*
0,399	*	-	-
0,389	-	*	-
0,378	-	*	-
0,368	-	*	-
0,360	*	-	*
0,345	-	*	-
0,340	*	-	*
0,316	*	-	-
0,298	*	-	*
0,281	-	*	-
0,258	-	*	-
0,239	-	*	-
0,222	-	*	-

6.5.3 Analysis of contour plots to determine wave resistance

The contour plots for those speed ranges indicated in Table 6.1 were analysed to obtain the wave resistance of the model using the author's energy analysis procedure described in Section 4.6.

All contour plots analysed were on a 1:10 scale. The analysis is described as follows:

(i) The sailing line of the model is marked on the plot. Transverse lines at 0,250 LWL intervals are constructed. The furthest transverse section is 3,5 waterlines aft of the midsection of the model.

(ii) Surface profiles are drawn by hand for each of these sections and plotted on graph paper using a 5 times vertically exaggerated scale.

(iii) The transverse profile is subdivided into intervals of 50 mm and the heights at these points recorded.

(iv) The water surface elevations for each section are entered into the micro-computer and stored in separate files using a file managing program "EDIT".

(v) The data is carefully checked and then the integration program loaded and run. The program numerically evaluates the energy in the wave profile, using Eq. 4.9.

(vi) The energy for all the transverse profiles is calculated and plotted as an energy versus distance along sailing line graph. The area under this graph is numerically integrated to yield the energy contained in the wave pattern.

(vii) The wave resistance is then calculated as determined in Section 4.6.

A flow chart of the analysis procedure is given in Fig. 6.9. A sample of the program "ENERGY.SIM" output is given in Fig. 6.10.

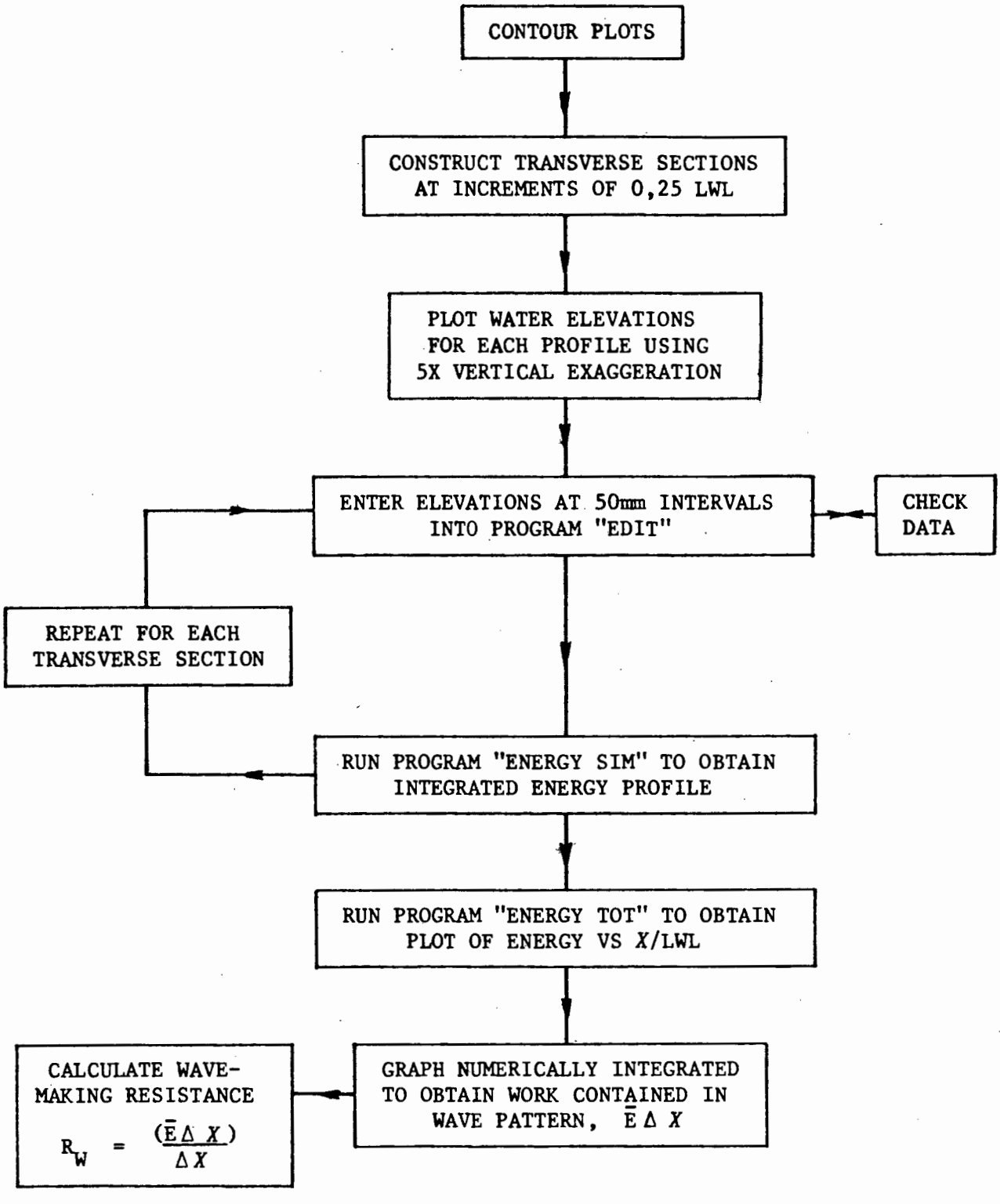

Fig. 6.9: Analysis of contour plots

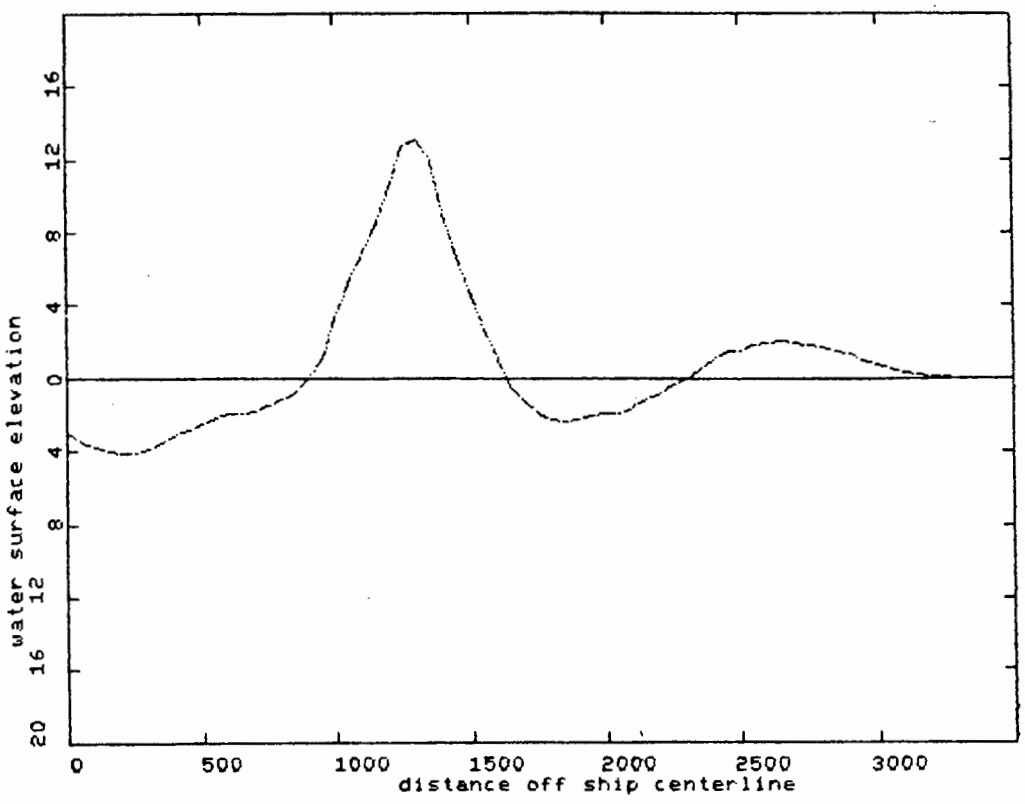

FROUDE NUMBER = 0.407

TRANSVERSE CUT ALONG X/L = 3.250

WAVE ENERGY ALONG CUT = 0.546819 Newtons
LENGTH OF INTEGRAND = 3300
NUMBER OF INTERVALS = 66
INTERVAL WIDTH (mm) = 50

Fig. 6.11: Sample output of energy integration program illustrating the surface water elevations and the integral results

7. ANALYSIS AND DISCUSSION OF RESULTS

7.1 Introduction

In this chapter the experimental results for total resistance, squat, trim and wave resistance calculations are presented.

All the resistance curves are represented in dimensionless coefficient form, except where otherwise stated. In the experimental wave pattern diagrams the dimensionless x/LWL and y/LWL axes are shown, along with the positions of the model. The zero or datum line of mean water level is indicated by a solid continuous line. All elevations above or below this line are represented by a thin continuous line and are marked as either positive (above) or negative (below).

All the stereopairs were analysed with great care to ensure accurate representation. Regions of certain anomalies were re-observed. The photographic stereopairs for each case are given for interest and can be observed using a stereoscopic viewer.

7.2 Total resistance results

The total resistance curves were determined using both the spring balance and load cell readings. Fig. 7.1 represents the readings for the total measured drag using both methods. A linear regression routine was used to obtain a curve of best fit, but the results were not satisfactory, and needed a sixth order or higher polynomial, thus an visual best fit was used.

It can be seen from Fig. 7.1(a) that there is a reasonable spread of data on either side of the curve, especially in the lower speed ranges. The spread of data is exaggerated in Fig. 7.1(b), the dimensionless coefficient representation having a velocity squared term in the denominator. Both curves represent the same data and either can be referred to in the discussion.

The readings recorded by the spring balance are consistently greater than the fitted curve in the higher speed ranges and consistently less in the intermediate range. Below values of Froude number of $\pm$0,28, the readings tend to become more scattered, as seen from the spread of data points. These differences in readings are due to the oscillatory behaviour of the spring balance and the short towing distance. At high speeds the acceleration is consequently more rapid and the balance is thus very rapidly extended. The high acceleration results in a high accelerated force. Due to the sudden steady state of the model, there is a rapid deceleration and the spring is thus reducing from the high accelerated drag force to the steady state drag (Fig. 7.2). At these speeds the time to complete the run is of the order of 6 to 7 seconds. The stereo photograph is taken at approximately three quarters of the way across the wave basin, thus the model has been at steady state for about 3 seconds, the first 1 to 1,5 seconds being the acceleration phase. The spring is thus opposing both the forces of the ship drag and its own extended force due to the acceleration. As the model is moving forward at the winding drum speed, there is an additional forward component due to the spring releasing itself to reach steady state. The higher speeds were thus photographed at ship steady state but not at the spring balance steady state.

The spring balance will achieve a constant force with time, but due to the length of the basin this could not be achieved it at the higher speeds.

The oscillatory nature is seen throughout the curve and at F_n = 0,42 the values are lower than the mean curve. The spring balance is thus beginning to converge to steady state. The inherent problem of a spring balance is the distance of spring extension to record the drag. This distance affects the time taken for both model and ship to achieve the steady state. At lower speeds the acceleration/deceleration curve is extended and the balance oscillates more freely as the drag force is less. Fig. 7.2 represents schematically the force versus time to achieve steady state. Region A can be seen for the high speeds and regions B and C for the lower ranges,

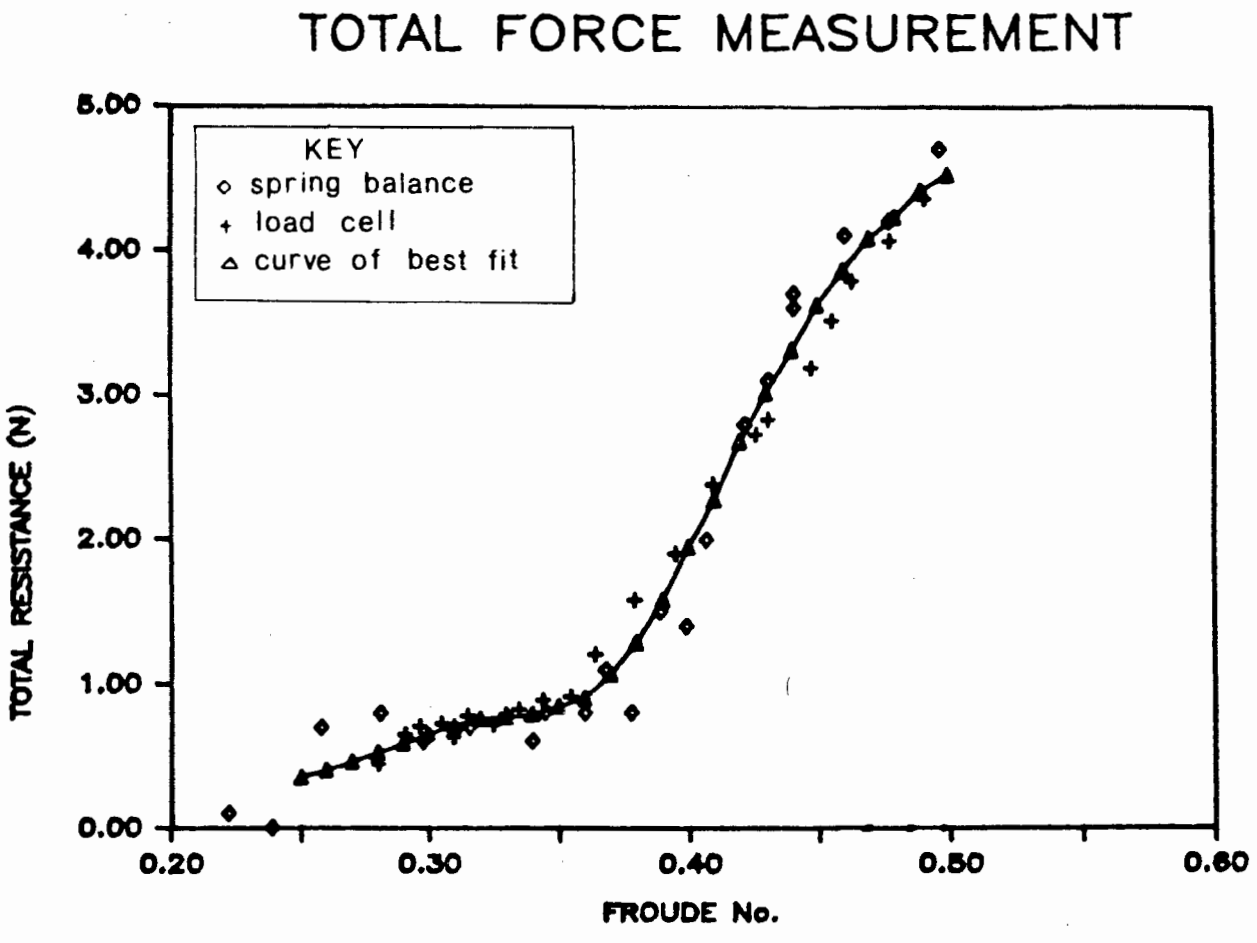

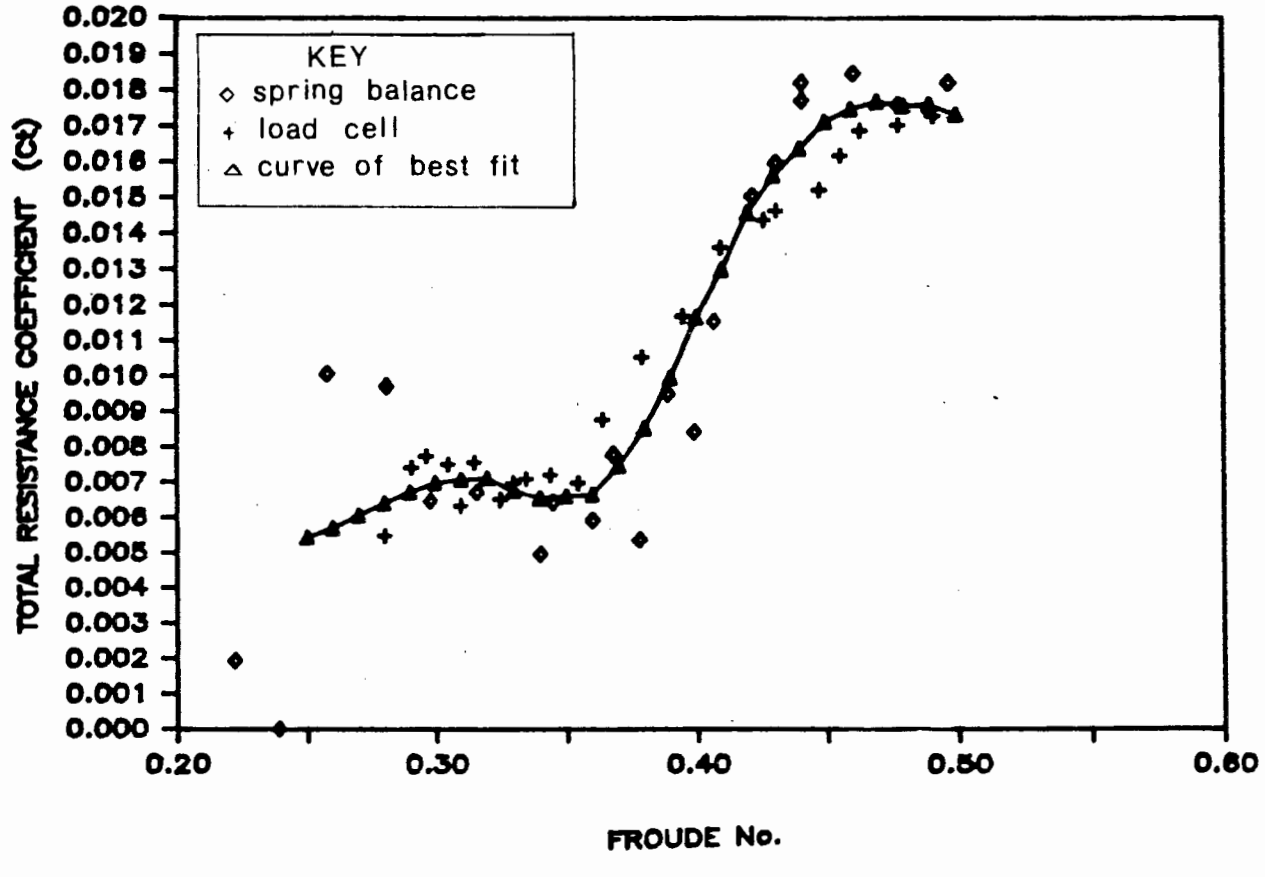

Figs 7.1(a) and & 1(b): Total resistance and total coefficient curves

the oscillatory nature diminishing with time. On occasions it was noted that the towing cord slackened completely due to the spring balance extension. The drag readings at these instances approaches zero. This only occurred in the lower speed ranges and thus data below 0,25 is suspect. The spring balance was calibrated horizontally.

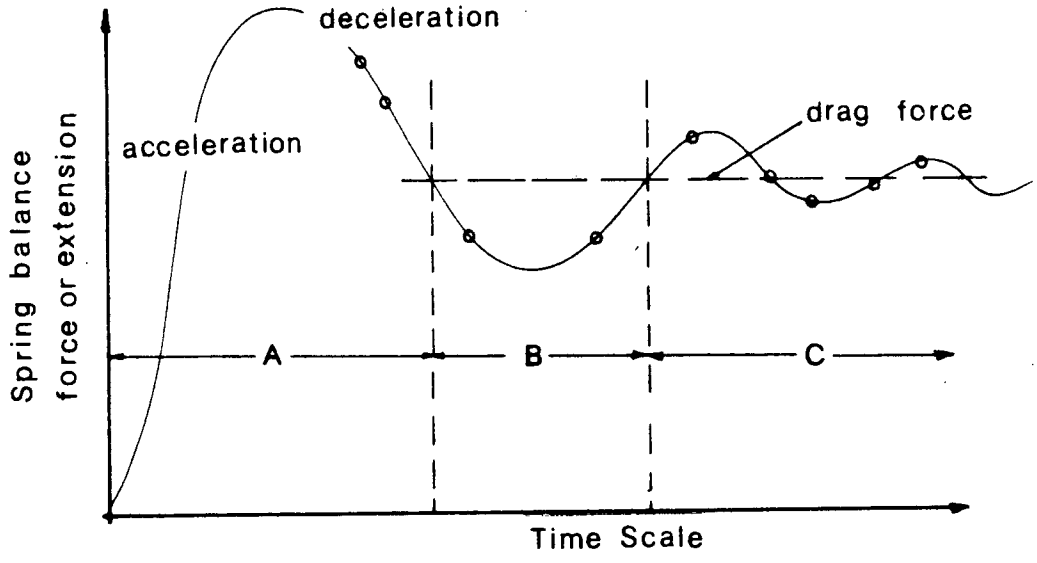

Fig. 7.2: Schematic representation of spring balance balance recorded force vs time

The results of the cantilever/strain gauge system were more consistent than those of the spring balance. The load cell has a similar oscillatory nature to the balance, but the displacements are reduced considerably to the order of less than 5 mm. This deflection still produces oscillatory results but of a much smaller magnitude and stabilising more rapidly. The suspended cable from load cell to data acquisition unit did not interfere with results, although it could be the reason for slightly higher values in the low speed ranges, due to the friction and vertical weight of the cable.

Slight discrepancies along the curve could be due to the interpretation from the mean results of the drag curve (Section 6.4.3.2, Fig. 6.8) although the interpretation was done as carefully as possible.

Neither force measurement methods give representative values in the lower speed ranges due to the small forces involved of order 0,4 N. The spring balance method has the advantage of a permanent record, but due to the large extensions required to record the drag it is only applicable to those speeds where the drag force is large enough to offset the spring extension force. This occurs above values of F_n = 0,34. The load cell can be used for speeds above F_n = 0,25. The major problem for both approaches is the short towing distance of the model as the towing time does not allow for complete stabilisation of the drag curve, but on the whole the towing distance is enough to detect where the steady state drag occurs.

Fig. 7.3 represents the faired values for this model compared with the results of Tsai (1975) who presented data for three Series 60 model geosims, the parent form being the same as the model used. Two models of 1,80 m and 3 m are compared with the present model. Both models were free to squat and trim and vertical bow turbulence stimulators were used. The normal operating speeds of the Series 60 is generally up to Fn = 0,40, but the present study extended this to 0,50 to obtain a larger spread of results. The observed hollows and humps occur on the resistance curves at Fn = 0,24 and 0,30 respectively. Below values of Fn = 0,10 the total resistance becomes more or less constant. The discrepancies of results in Fig. 7.3 are particularly interesing as it is seen that the resistance coefficient differs according to model scale, the smaller model having higher values in the region of Fn = 0,25 to 0,35. No turbulence stimulation was used on the present model and the flow could have been laminar throughout due to the short length. The observed resistance curve hump is considerably higher possibly because of the sensitivity of the towing system, the model being totally unrestrained, and enhancing the effects of the phase shifts of the bow and stern waves.

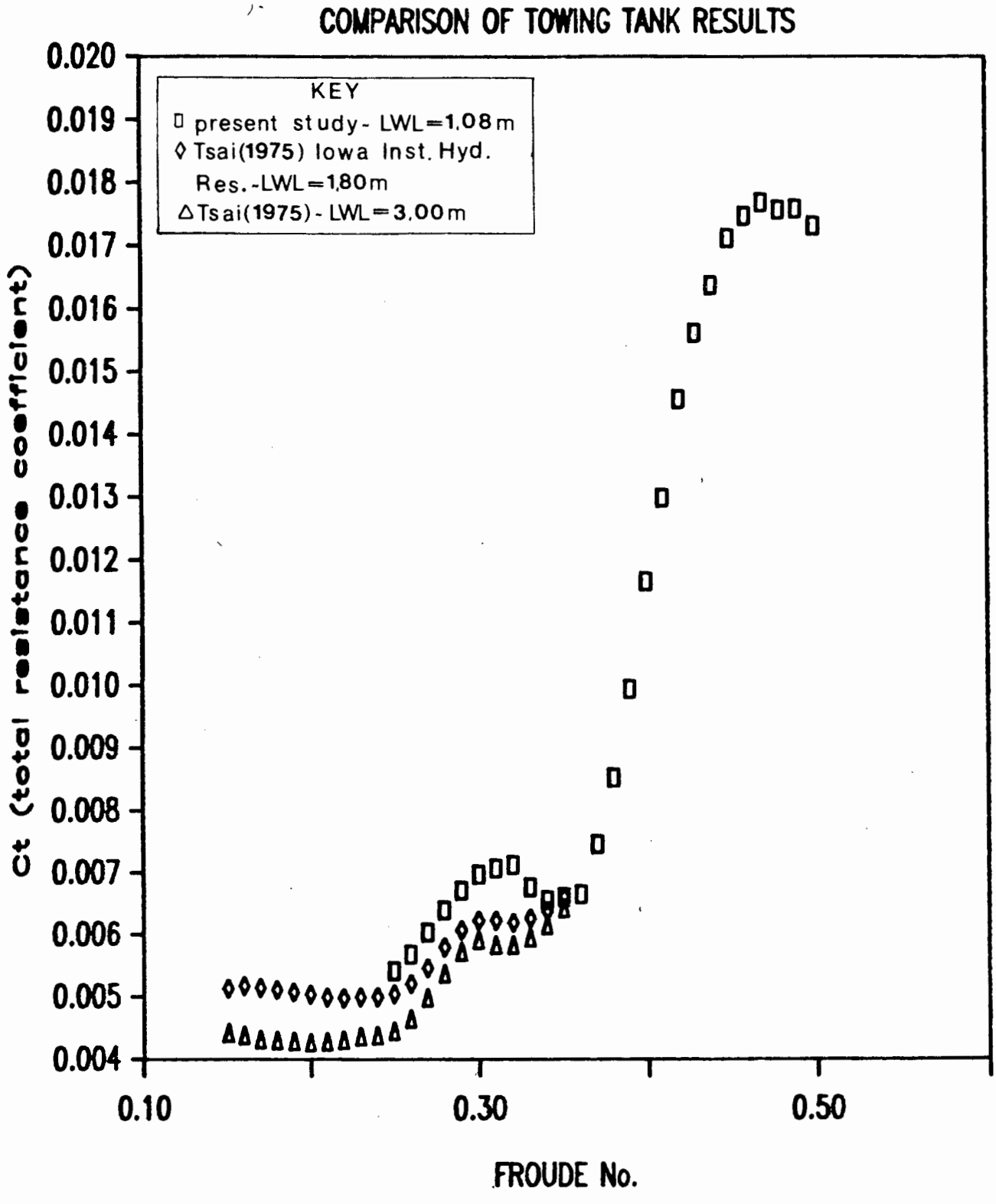

Figs 7.3: Comparison of Total Resistance results with Tsai (1975)

The three curves converge at F_n = 0,35, no data being available above this value for the two larger models, but they indicate a similar tendency to steepen.

Fig. 7.4 illustrates the set of resistance curves obtained for the present model. The curve of residual resistance of Froude is shown as $C_t - C_f$. The skin friction coefficient is that of the C_{ITTC} friction line. At lower values the skin friction curve is approaching the total resistance curve. The C_t curves become reasonably constant apart from minor undulations to the wave system phases. Skin friction is thus completely dominant at these speeds, accounting for virtually all the resistance. Residual resistance tends to zero as the wave making decreases markedly. At F_n = 0,38 the contributions of residual and frictional resistance are the same. Above this speed the residual resistance becomes dominant as the wave making increases, contributing to 75 - 80% of the total drag at the high speed ranges.

As discussed in Section 3, the skin friction, C_{ITTC}, curve is only empirical and C_f would undulate if it was experimentally determined using a momentum wake traverse.

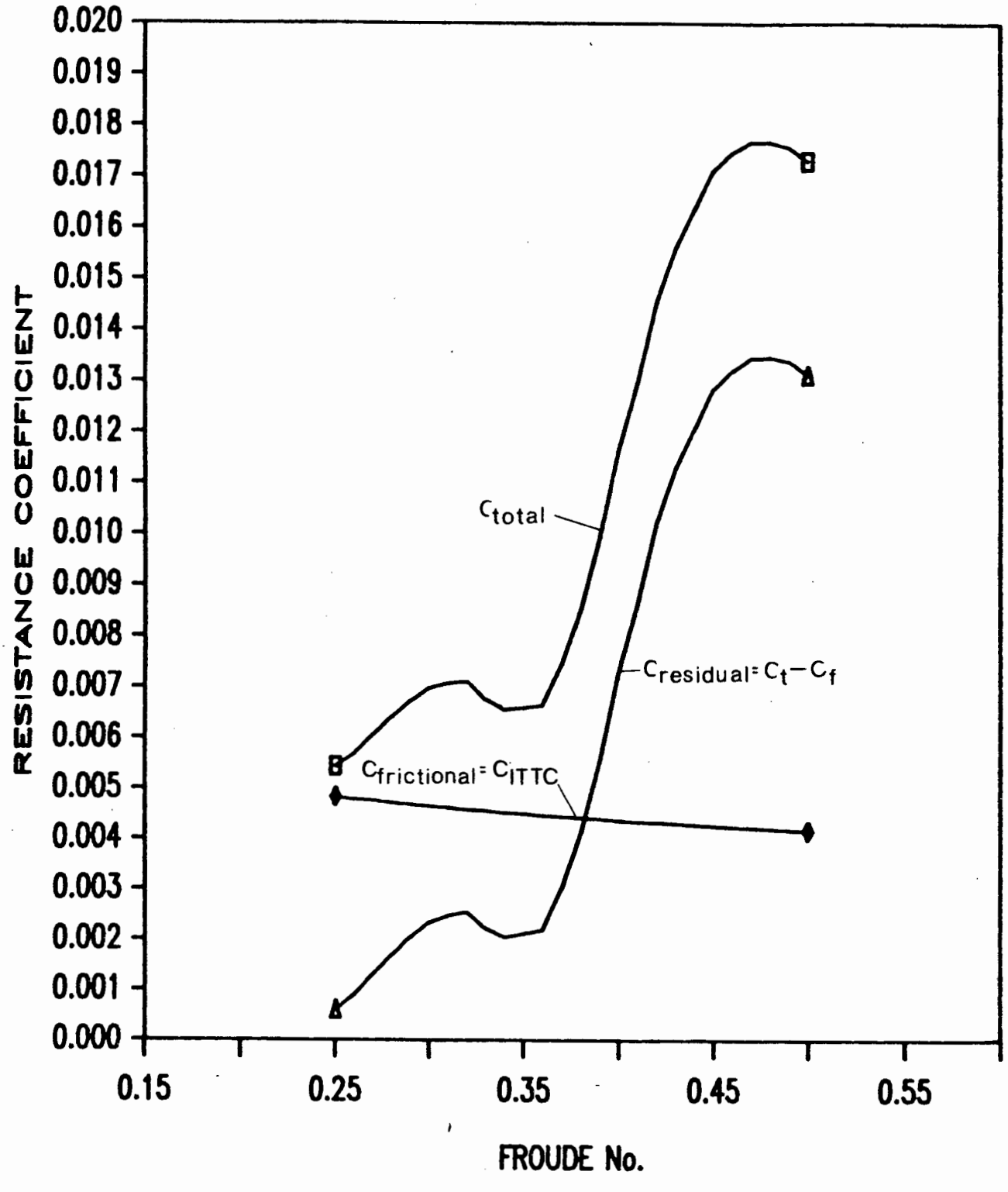

Fig 7.4: Resistance curves for Series 60, C_B = 0,60

7.3 Squat and trim results

Measurements of the bow and stern levels were taken for all photographed Froude number speed ranges. The squat and trim were calculated using equations 3.1 and 3.2. The trim was changed to represent a horizontal angle and is thus, in a sense, dimensionless. The squat is non-dimensionalized by $U^2/2g$.

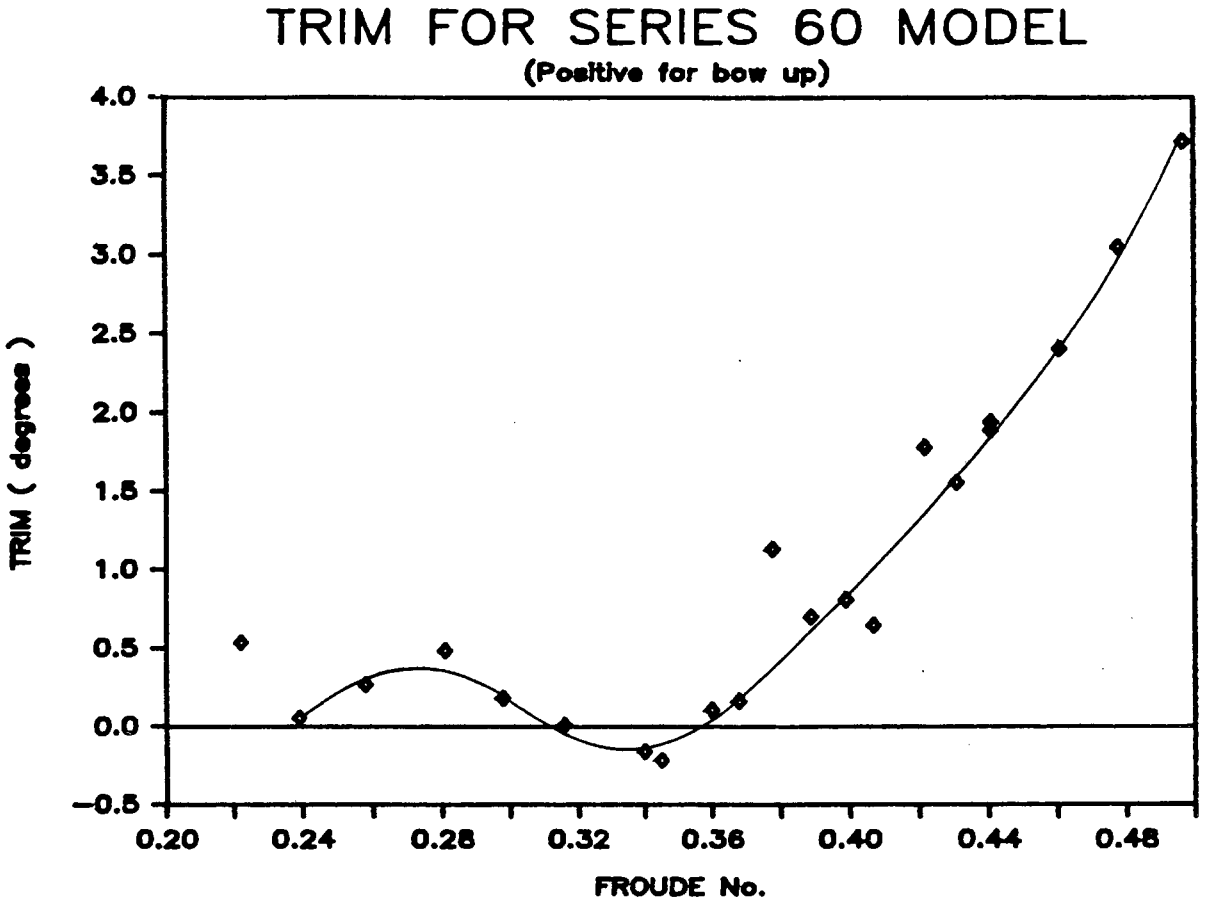

Fig. 7.5: Trim for Series 60 Model

Fig. 7.5 represents the trim angle versus Froude number relationship. Analysis of the results show a very definite trend and undulatory nature as did the total resistance curve. Certain data points are definite outliers and relating these to the spring balance drag curves, it can be seen that the same values are in error. At F_n = 0,222 both values are obviously wrong. This means that at the time of taking the stereopair, the towing line was either slack or

instantaneously tautened, changing the bow and stern levels. This was possibly also the case for F_n = 0,378, the force and trim measurements both deviating from the mean curve. Comparing these results with the resistance data, the curves corroborate one another extremely well. Both results are taken from independent analyses. The hump of total resistance at F_n = 0,32 corresponds to the change in trim angle at this point. The model is level and beyond F_n = 0,32 the trim angle becomes negative, thus the bow is lower than stern. The stern is riding the crest of a wave and thus the model is being aided by the forward motion of its own stern wave, and there is therefore a decrease in the total resistance as shown in Fig. 7.3.

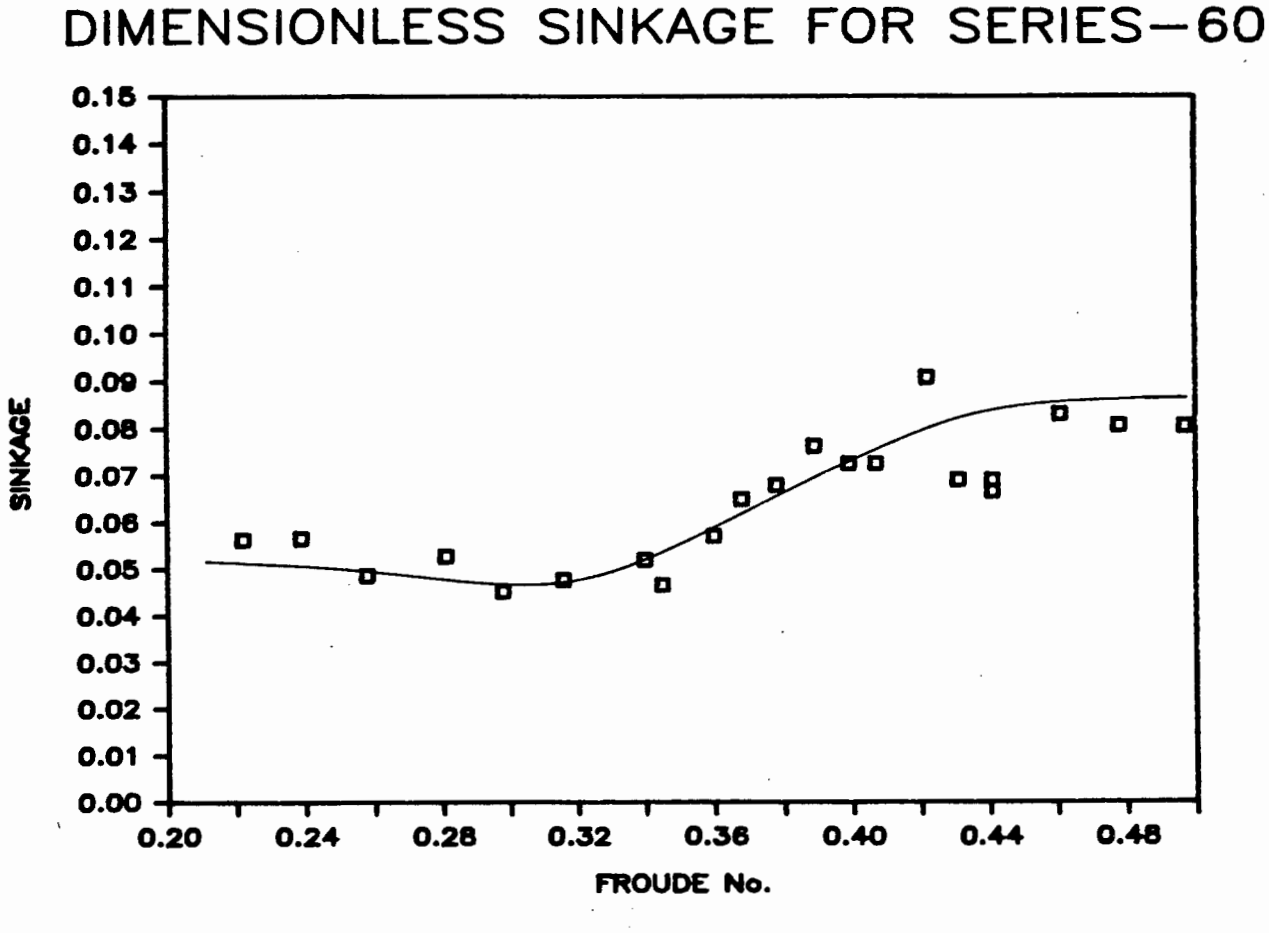

Fig. 7.6: Dimensionless sinkage for Series 60 model

The greatest negative trim angle of 0.3° occurs at F_n = 0,345. Between F_n = 0,345 and 0,360 the negative trim is decreasing and

becomes positive above a F_n = 0,360. This trend follows that of the total resistance which reaches a local minimum at F_n = 0,353 and at F_n = 0,37 reaches its previous local maxima. There is thus a lag of total resistance in picking up the effects of trim changes over a range of F_n = 0,01. Above values of F_n = 0,360 the trim increases rapidly as the size of the bow wave increases. It is difficult to say when this peaks, but from the graph of total resistance it appears the trim would begin to decrease at above values of F_n = 0,50.

The graph of sinkage or squat versus Froude number is shown in Fig. 7.6. The sinkage is gradually increasing as the hull settles into the water. At the lower speeds the squat is fairly constant and increases above F_n = 0,35, the same speed range where the trim began its upward trend. The squat is very sensitive to small fluctuations of bow and stern levels and on a model of this size are very small, the effect of deep water not showing too much of a sinkage variation. If the water depth were decreased to shallow water condition the sinkage would increase accordingly. The non-dimensionalised factor of $U^2/2g$ serves to increase the spread of data points as was observed in Fig. 7.1(b)

7.4 Wave pattern measurements

7.4.1 Wave resistance results

The contour plots analysed for wave making resistance are presented. The five speeds were selected as being representative of the range of Froude numbers. Two speeds of close proximity F_n = 0,340 and 0,360 were chosen due to the nature of the curves of trim and total drag, representing the region in which resistance decreased. The five Froude numbers analysed are 0,298; 0,340; 0,360; 0,407 and 0,441.

In all cases the stereopair and contour plot is given. The first and highest speed, F_n = 0,441 is fully discussed and analysed giving complete results of the energy analysis and energy distribution within the wave pattern. All the other speeds are analysed only between x/LWL = 1,5 to 3,5, a distance of 2 ship waterlines. This is the region of the far field and wake which is unaffected by the interaction of the wave pattern with the hull and necessary for the determinatin of wave resistance. 3-dimensional representations are given for F_n = 0,441 and 0,407.

7.4.1.1 Froude number = 0,441

The contour plot for this speed is shown in Fig. 7.7. The wave system is well developed throughout, the bow wave peaks at 20 mm, some 270 mm aft of the forward perpendicular. There is then a substantial trough of 28 mm below MSL occurring 540 mm aft of the bow wave peak. Thus the wave height is of the order of 50 mm (H = 2a). The transverse system of waves is well developed. showing a regular spacing of crests and troughs aft of the stern. Three major crests are evident, including the bow wave. The stern wave has a peak of 24 mm, 520 mm beyond the major trough. The wavelength from crest to crest is of the order of the waterline length of the hull, being 1,060 m. The d/L ratio is thus 0,472, lower than that required for deep water. This does not correspond to Blevins (1984) who stated that the effective wavelength is of the order of 90% of

the LWL and on which the water depth/model size was calculated. Due to this finding no energy analysis was done for contour plots above F_n = 0,441.

Beyond x/LWL = 3,5 the surface is generally irregular and confused as this is the starting acceleration region and is affected by the wave and reflection off the basin walls. This region is evident on the 1:10 scale contour plots.

Fig. 7.8 presents the results of the energy transverse cut analysis procedure for this case. The energy forward of the bow is zero increasing sharply to a maximum at the stern and then decreasing and tending to become undulatory in nature. The maximum stern value is due to the fact that there are no intermediate diverging waves, the bow wave creating a deep trough. This trough extends outwards and the point of maximum depression (28 mm below MSL) is in line with the ship stern. Thus in this region of transverse profiles we have both the combination of the stern wave crest and the bow wave trough. The extent of the trough is to about 2,5y/LWL abeam of the vessel tending to zero at the extreme borders. The decrease of energy aft is due to the slowly decreasing water surface elevations as the waves move away from the stern. The undulatory nature is due to the transverse wave system. The high energy values around the model are probably due to the combination of both the near field and free wave patterns, whereas beyond x/LWL values of 1 to 1,5 the contribution is due to the free wave pattern alone. The region used to calculate the wave resistance is therefore beyond x/LWL = 1,5.

The calculation procedure is as follows. The distance between x/LWL = 1,5 to 3,5 equals 2,016 m. The area under the curve in this region is found to be 1,353 N.m, representing the increase of E x and is the additional energy contained within this region of the wave pattern.

Thus the wave resistance, R_w is found as follows:

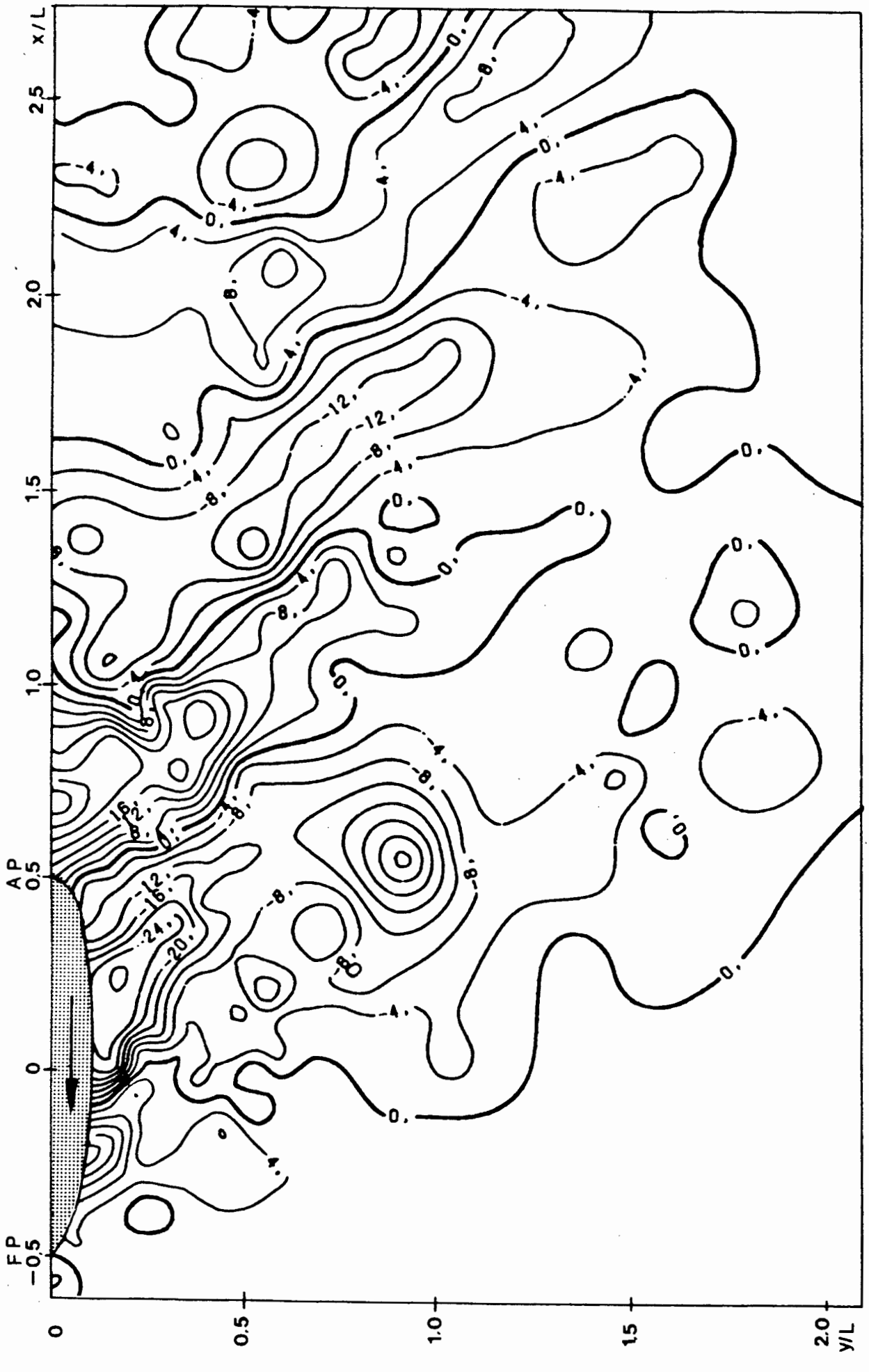

Fig 7.7: Contour map. Froude number = 0,441

$$-R'_w = \frac{(E\Delta x)}{x} = \frac{1,353}{2,016} = 0,671 \text{ N}$$

This is only half the wave pattern energy so thus total R_w = 1,252 N.

Fig. 7.9 is the stereopair analysed. The deep trough between bow and stern waves is clearly evident. The crests of the transverse waves are well defined. The large angle of trim is evident as the bow surges up the forward wave. Fig. 7.10 represents the three dimensional presentation of the water surface showing the large bow and stern wave system and the transverse waves.

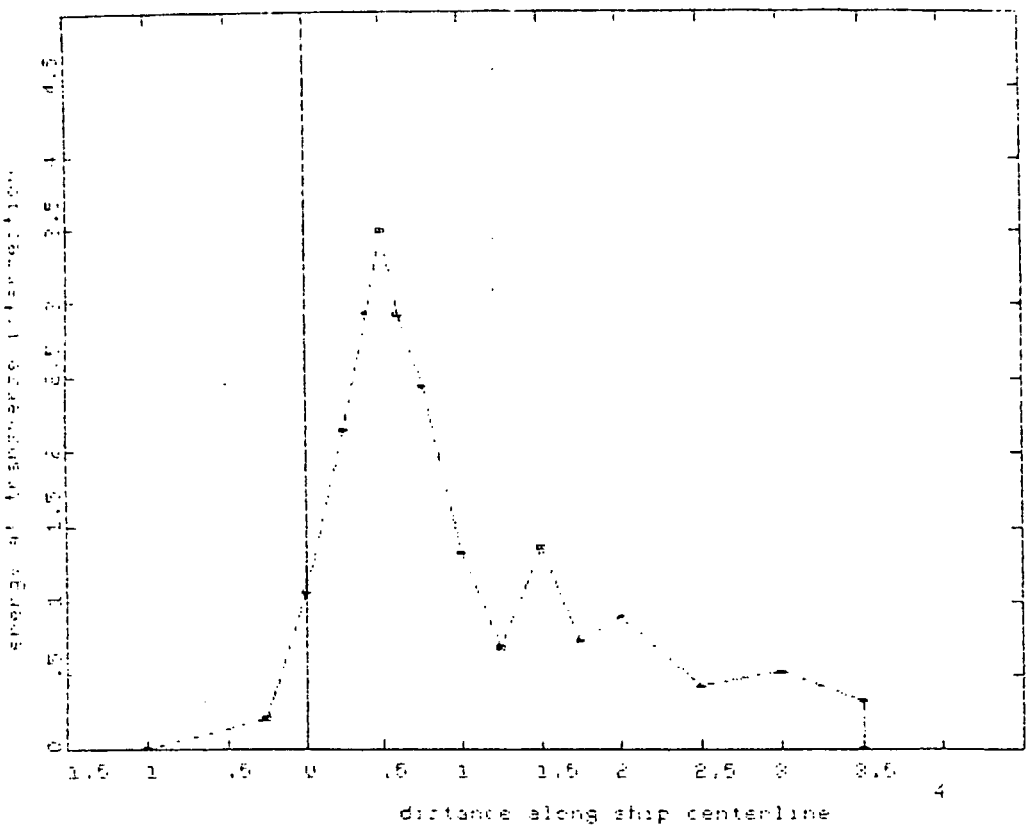

ENERGY STORED IN WAVE PATTERN=4.6507N.m
Froude Number = .441

Fig. 7.8: Transverse energy analysis

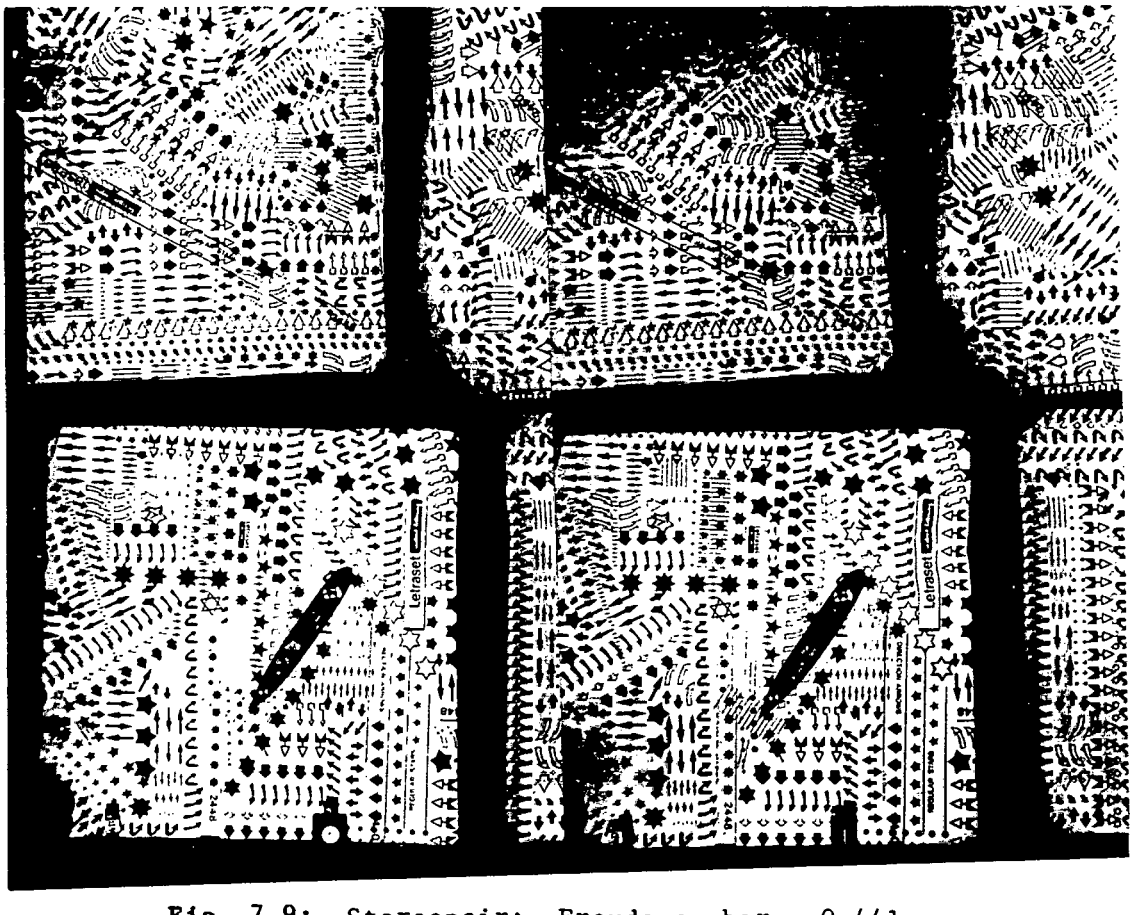

Fig. 7.9: Stereopair: Froude number = 0,441

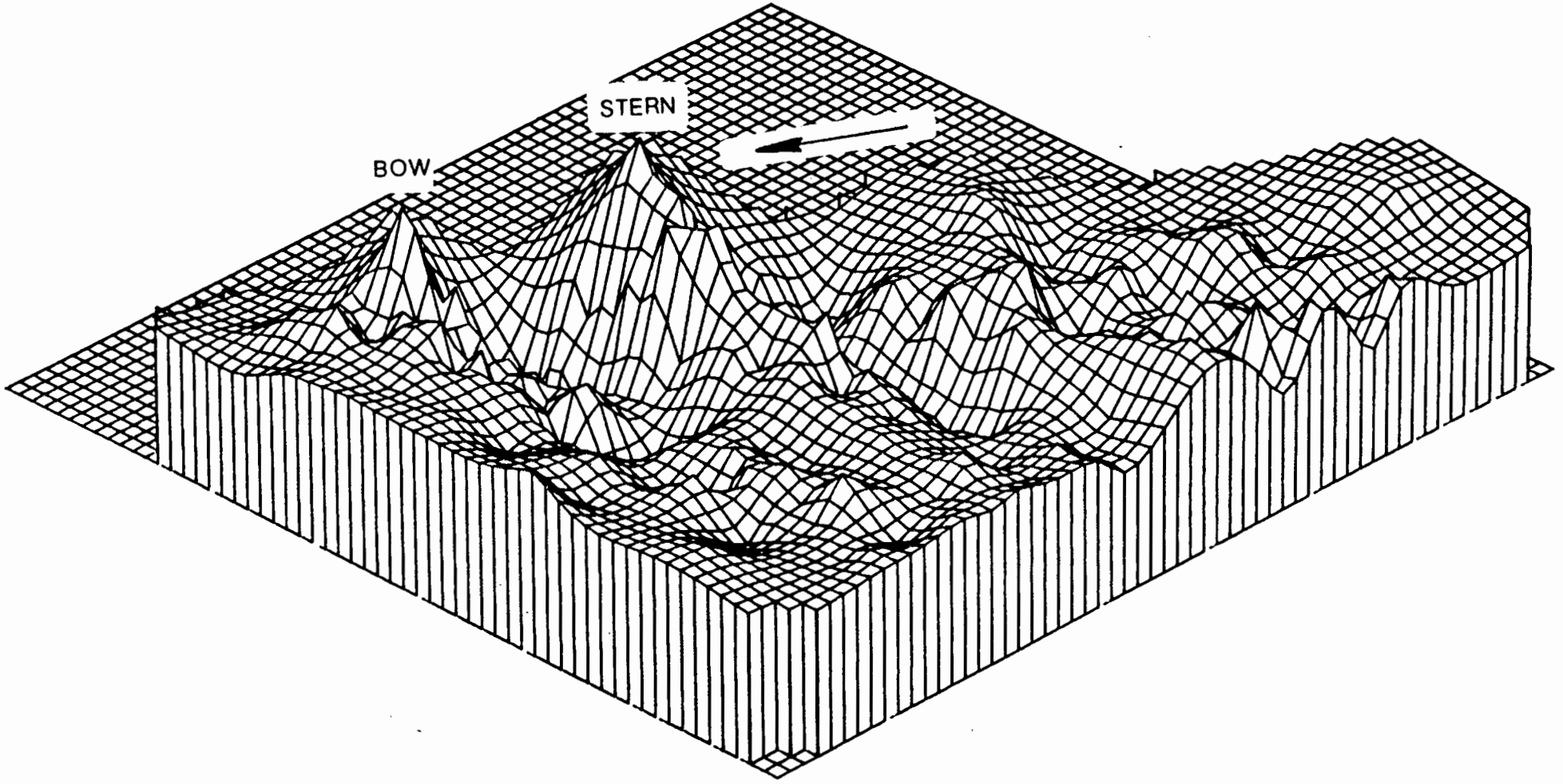

Fig. 7.10: Dimensional representation of the wave pattern

7.4.1.2 **Froude number = 0,407**

Fig. 7.11 represents the contour plot obtained at F_n = 0,407. The wave pattern is very regular and well formed, indicating that at this speed the ship has attained a steady state fairly rapidly and smoothly, as the regions aft of x/LWL = 2,5 show the continuing trend of the transverse system gradually diminishing.

The cusp-like curvature of the transverse waves is well represented, demonstrating the effects of diffraction on the wave system. Intersections of the transverse and diverging waves are clearly evident, forming an angle of 20° to the sailing line. The bow wave crest is 160 mm aft of the FP and has an elevation of 30 mm. This falls away fairly rapidly over a distance of 300 mm. An intermediate step can be observed in the hull wave profile occurring 350 mm aft of the crest, the trough having an elevation of -22 mm. Beyond the trough the profile is uniformly increasing to peak just beyond the stern at 26 mm. The wave height is thus 56 mm and the wavelength 950 mm. Thus for this speed the d/L ratio is greater than 0,5. Two major troughs are seen at x/LWL = 1,25 and 2,25 showing the repetitive wavelength occurring uniformly aft. The major transverse wave radiates outwards to y/LWL = 1,25 and has a second minor peak at this point.

The stereopair is presented in Fig. 7.12. The wave system along the hull is clearly visible, the intermediate diverging wave seen to form just beyond the major trough. The remaining pattern is well observed in the wake region, the transverse cusps being well defined.

A three-dimensional representation is shown in Fig. 7.13, illustrating the large bow and peak crests and the generally decreasing nature of the wave system aft of the model.

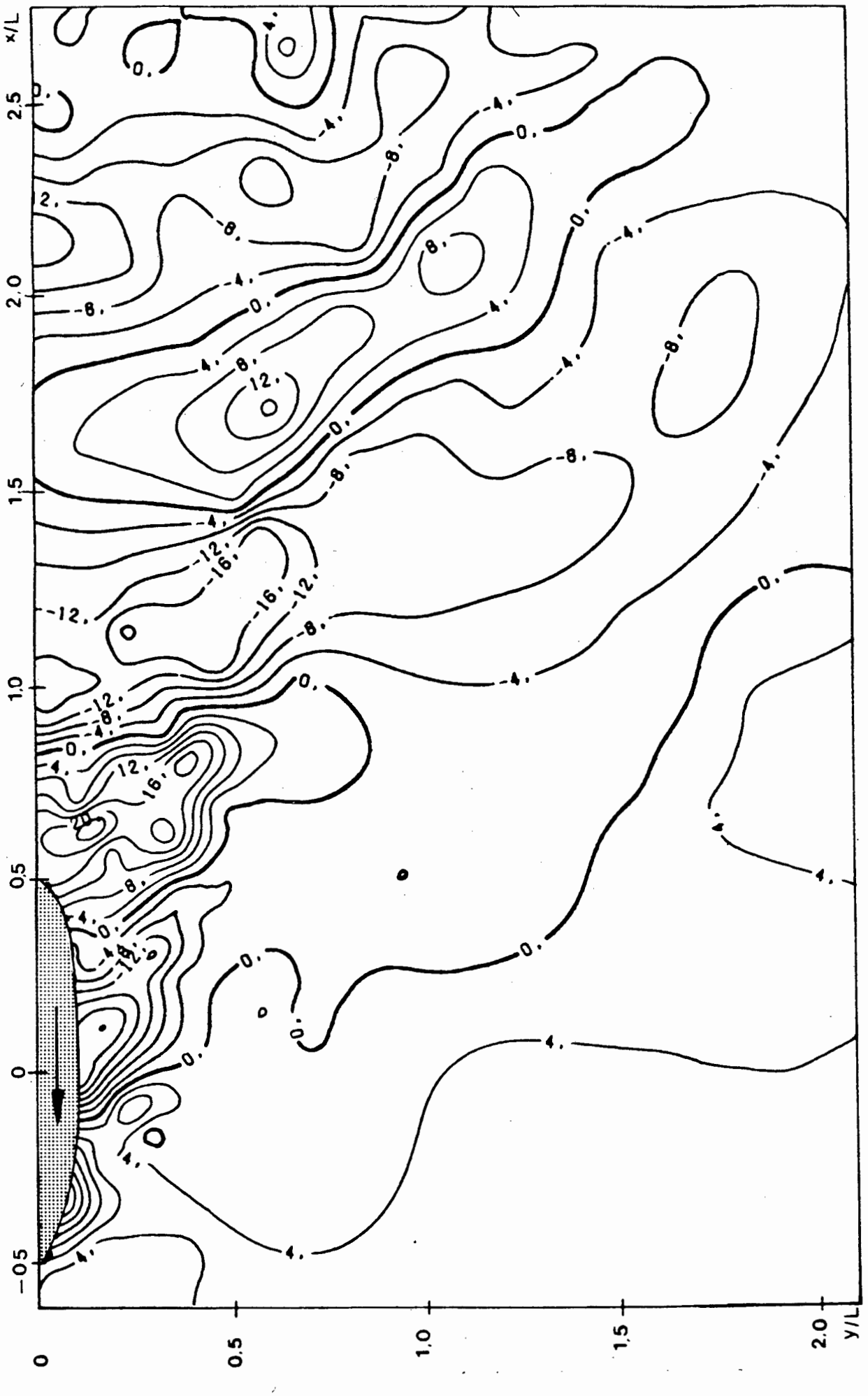

Fig 7.11: Contour map. Froude number = 0,407

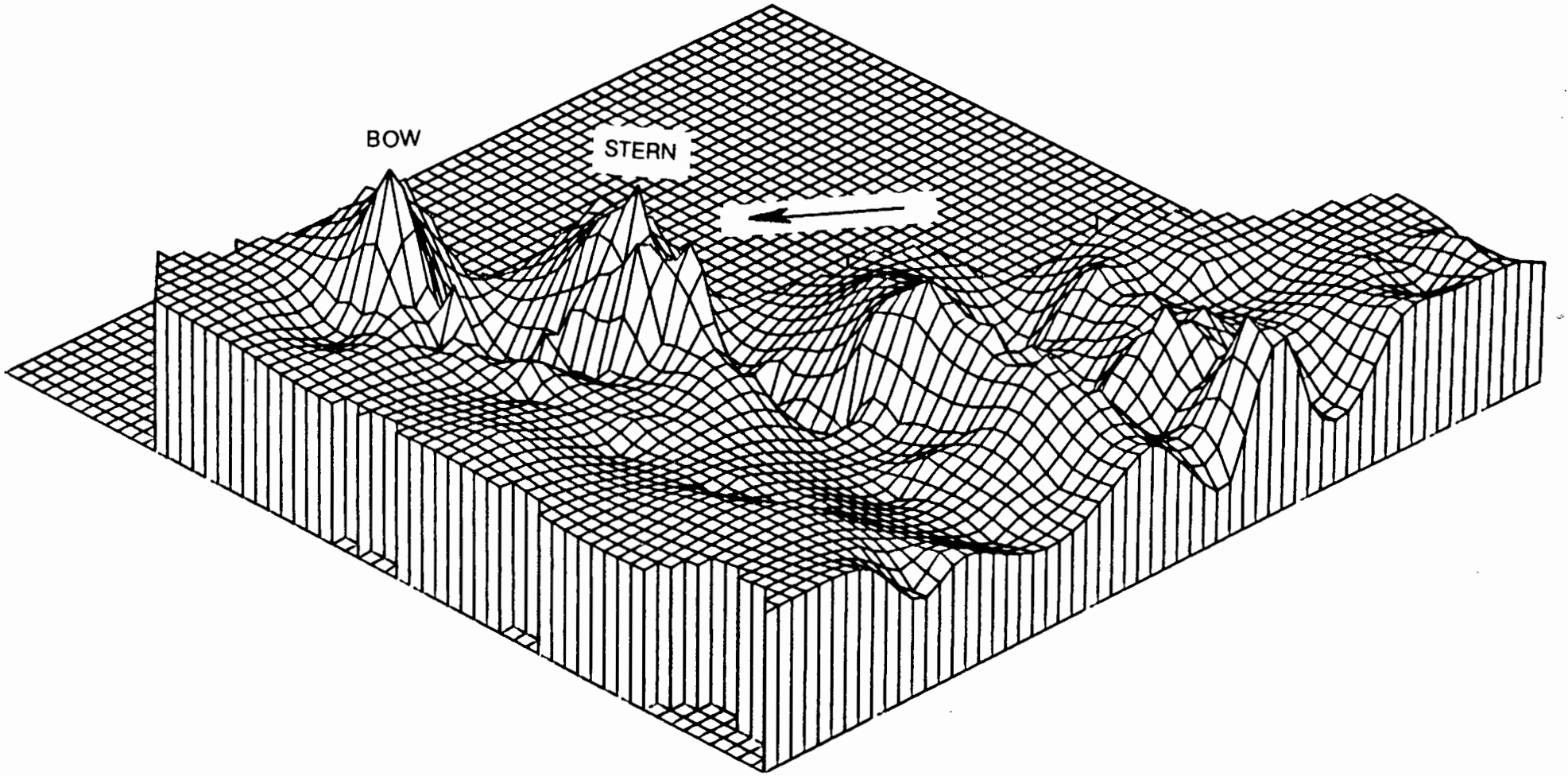

Fig. 7.13: Dimensional representation of the wave pattern

7.4.1.3 Froude number = 0,360

Fig. 7.14 shows the contour plot obtained at Fn = 0,360. The chosen contour interval of 2 mm is too low for the region surrounding the ship but represents the transverse wake section very well. A larger interval would result in too little detail being detected in the far field wave pattern. This interval was well suited to the 1:10 scale plot from which the transverse profiles were taken.

The bow wave peaks at 14 mm, about 120 mm aft of the forward perpendicular. A trough of -8 mm occurs 530 m aft of the crest and reaches a peak of 20 mm near the stern. The waveheight is thus 34 mm in the hull region. The wavelength is approximately 720 mm or two thirds of the LWL. Areas of intersection of the wave systems can be clearly seen as local peaks or troughs, indicated on the contour map when the contours are very close together forming steep crests. When measured the cusp line forms an angle of $\pm 19°$ with the sailing line in accordance with Kelvin's theory. The transverse wave system is evident, with a major translatory wave occurring at x/LWL = 1,5.

Analysis of the stereopair in Fig. 7-15 shows clearly the local intersections as crests or troughs. The intermediate wave alongside the hull can be seen as indicated on the contour plot, along with the transverse stern wave. Forward of the bow there is a sudden fairly steep decrease in wave height and then shallowing gradualllly to mean water level.

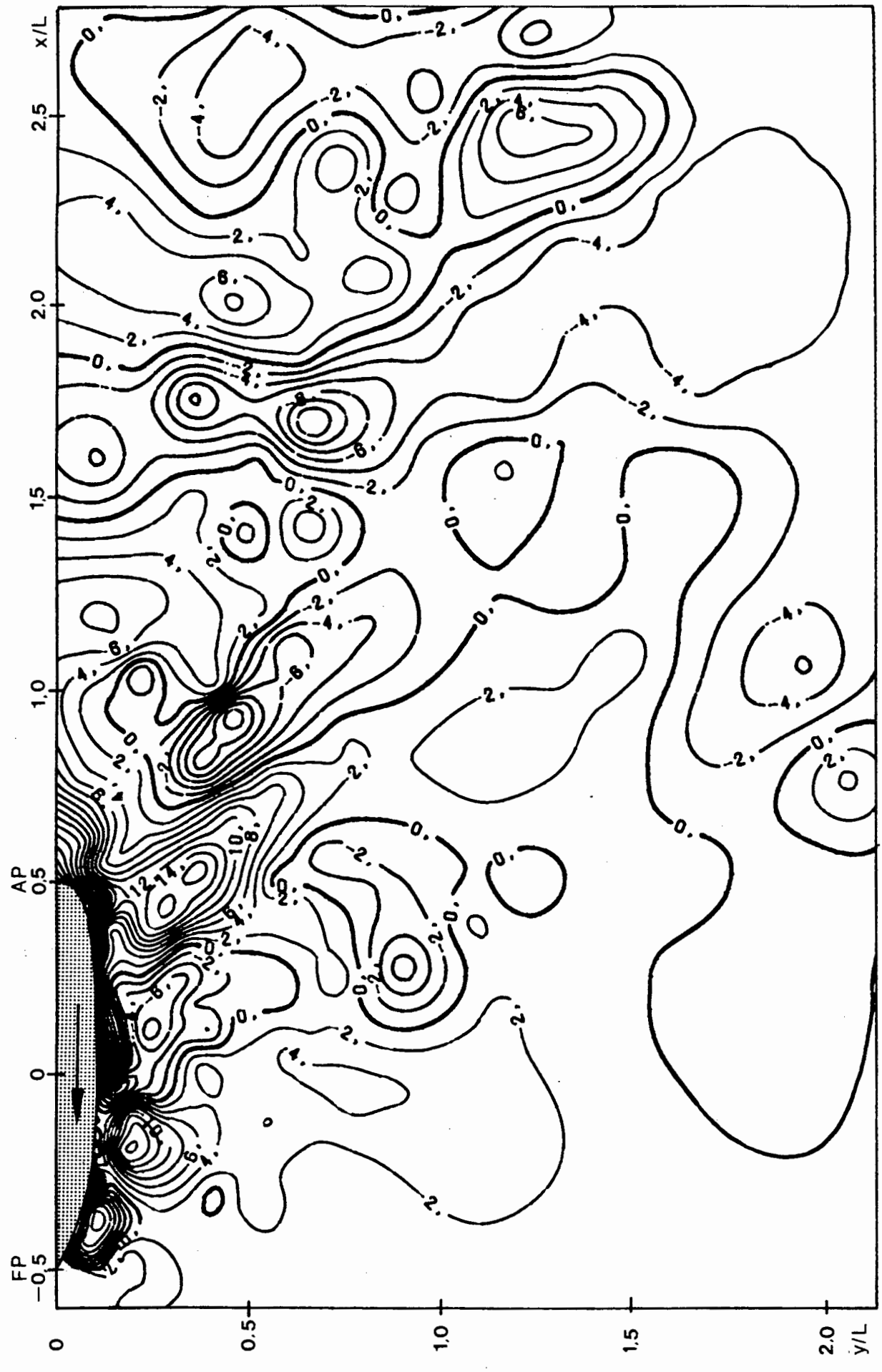

Fig 7.14: Contour map. Froude number = 0,360

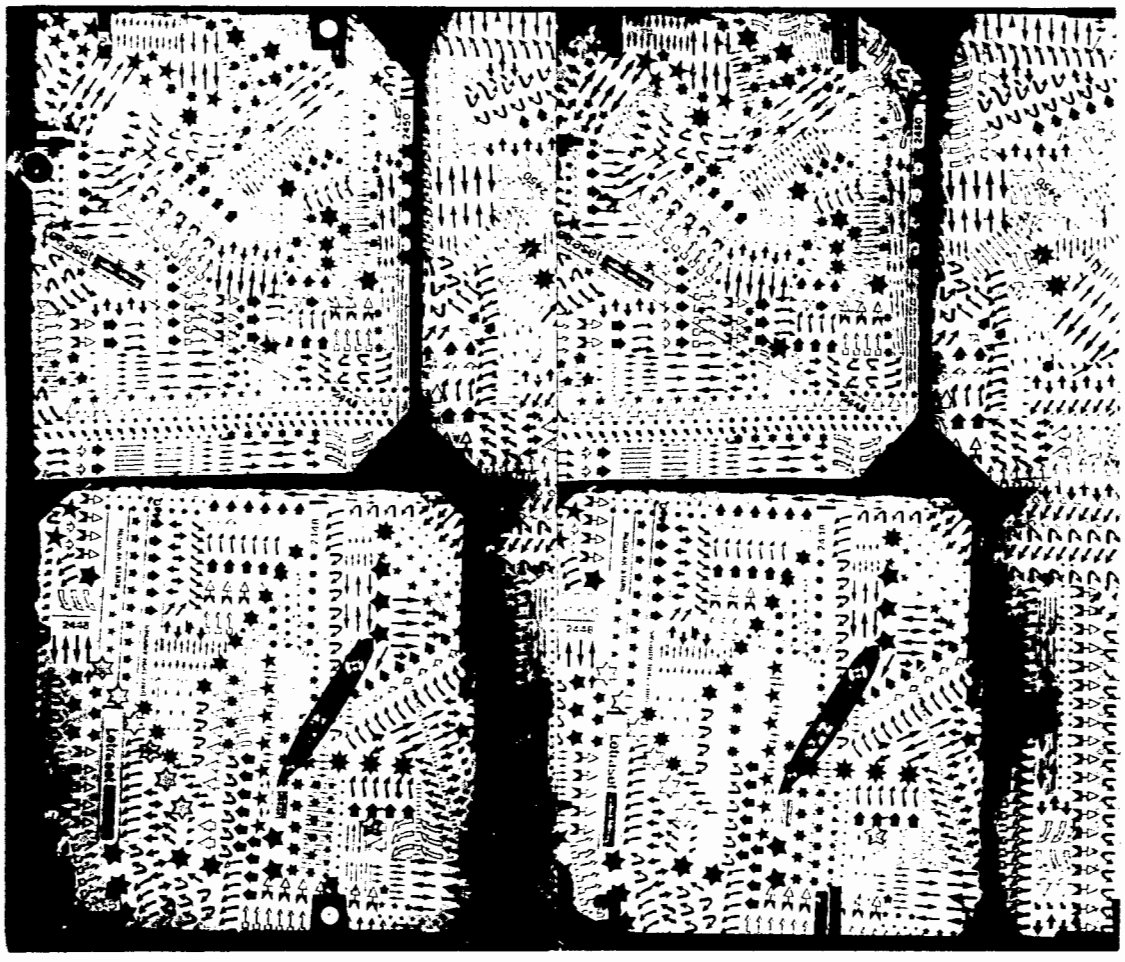

Fig. 7.15: Stereopair: Froude number = 0,360

7.4.1.4 Froude number = 0,340

This Froude number is the speed at which the trim is the most negative. The bow and stern waterline levels are of the order of 30 mm below mean water level, indicating the strong effect of the stern being carried along on the crest of a wave. Examining the wave contour plot in Fig. 7.16, this is clearly seen. The trough is 34 mm below mean water level occurring just forward of amidships. There is a steep drop from the FP to this trough, the elevation at the FP being 10 mm below mean water level. The forward section is being thrust forward by the stern wave, resulting in the forward shift of the bow wave, actually surging ahead of the bow. The stern or AP is nearly at mean water level, thus some 9,5 mm above the bow. This corresponds to the trim angle of -0,5°.

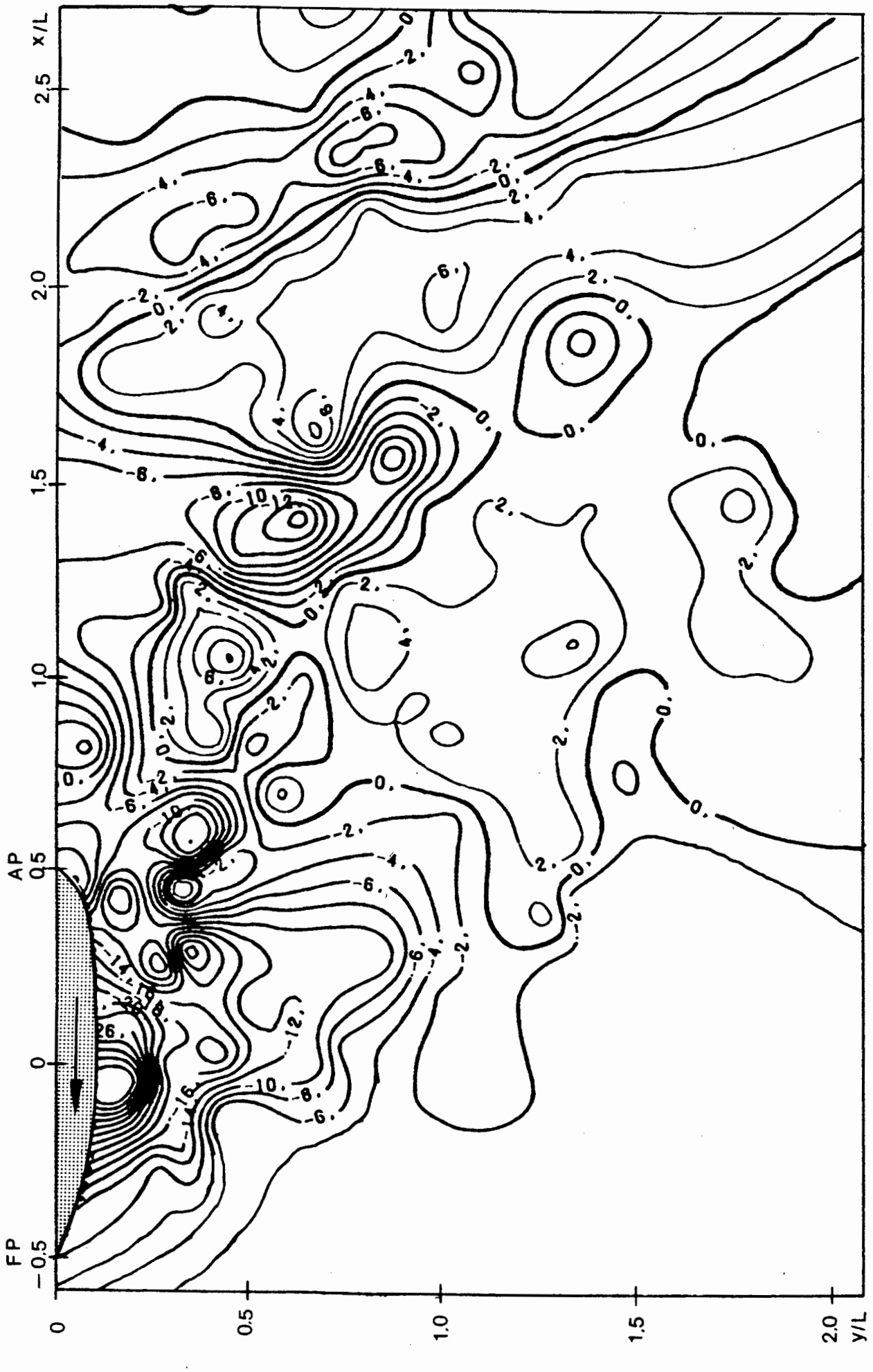

Fig 7.16: Contour map. Froude number = 0,340

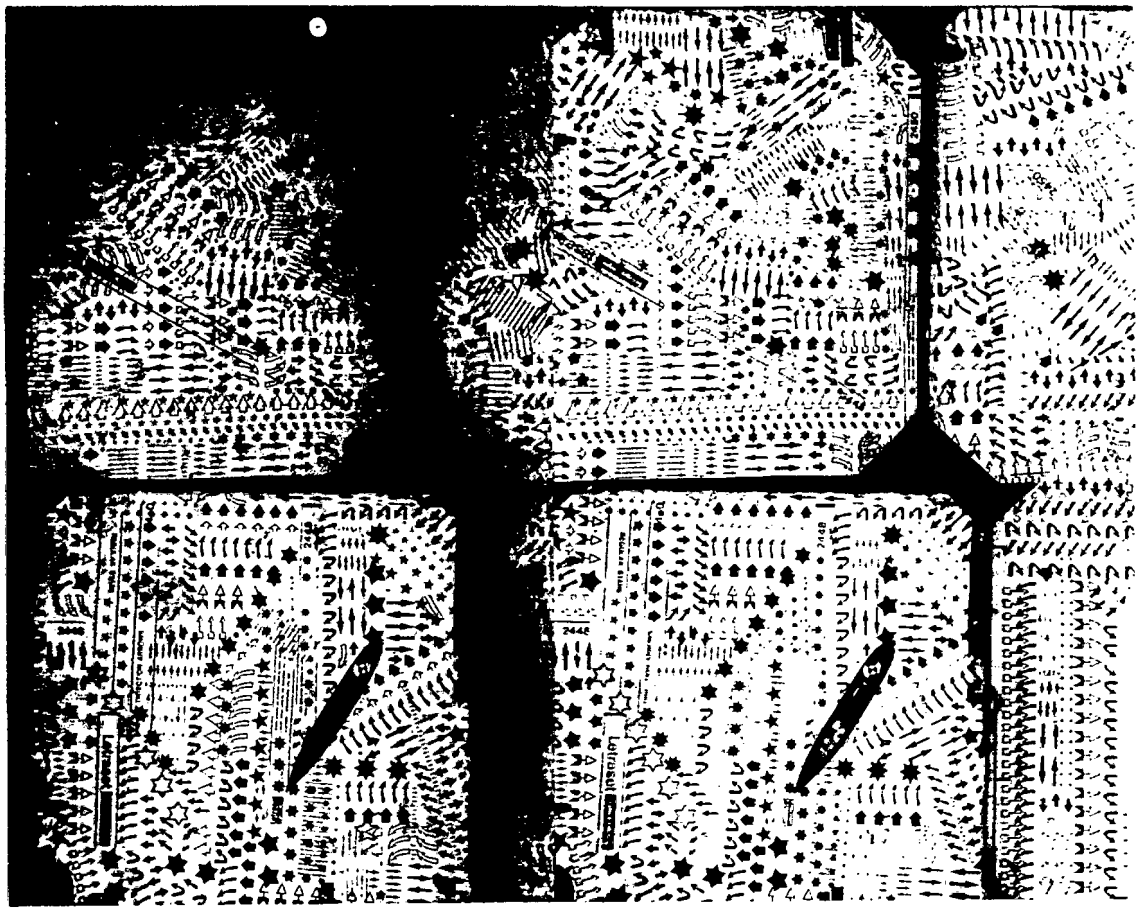

Fig. 7.17: Stereopair: Froude number = 0.340

The stern wave is seen radiating a short distance aft of the AP and is not as well developed as the stern wave at Fn = 0,360. The second transverse wave is well developed occurring at x/LWL = 1,75 and extends aft uniformly, showing the curvature and outward movement at the extremes. The steep intersections of the wave systems are evident as a line of darker regions where there is a steep wave slope. An intersection of these peaks with the sailing line forms the predicted angle of 20°.

The stereopair given in 7.17 depicts the negative angle of trim, the bow surging forward and the stern riding the crest of its own wave.

7.4.1.5 Froude number = 0,298

At these speeds the generated wave pattern is of extremely small amplitude as demonstrated in Fig. 7.18. The largest amplitude is 16 mm occurring at the bow wave with a minimum of -8 mm amidships. The wavelength is considerably reduced and several short intermediate diverging waves occur along the hull. The wavelength between the bow wave and the intermediate crest is 580 mm or approximately 0,5LWL. A series of local regions of maxima or minima occur at the intersections of the divergent and transverse waves, the angles of these to the sailing line again corresponding to the predicted theoretical value of 19°28'.

When observing the stereopair, Fig. 7.19, the small amplitude waves can be seen. At these amplitudes, accurate determination of the water surface is extremely difficult. The errors involved are thus considerably larger when translated into percentage of recorded wave height. Below these speeds the contour plots were not analysed in their entirety on the stereocomparator due to the small surface elevations.

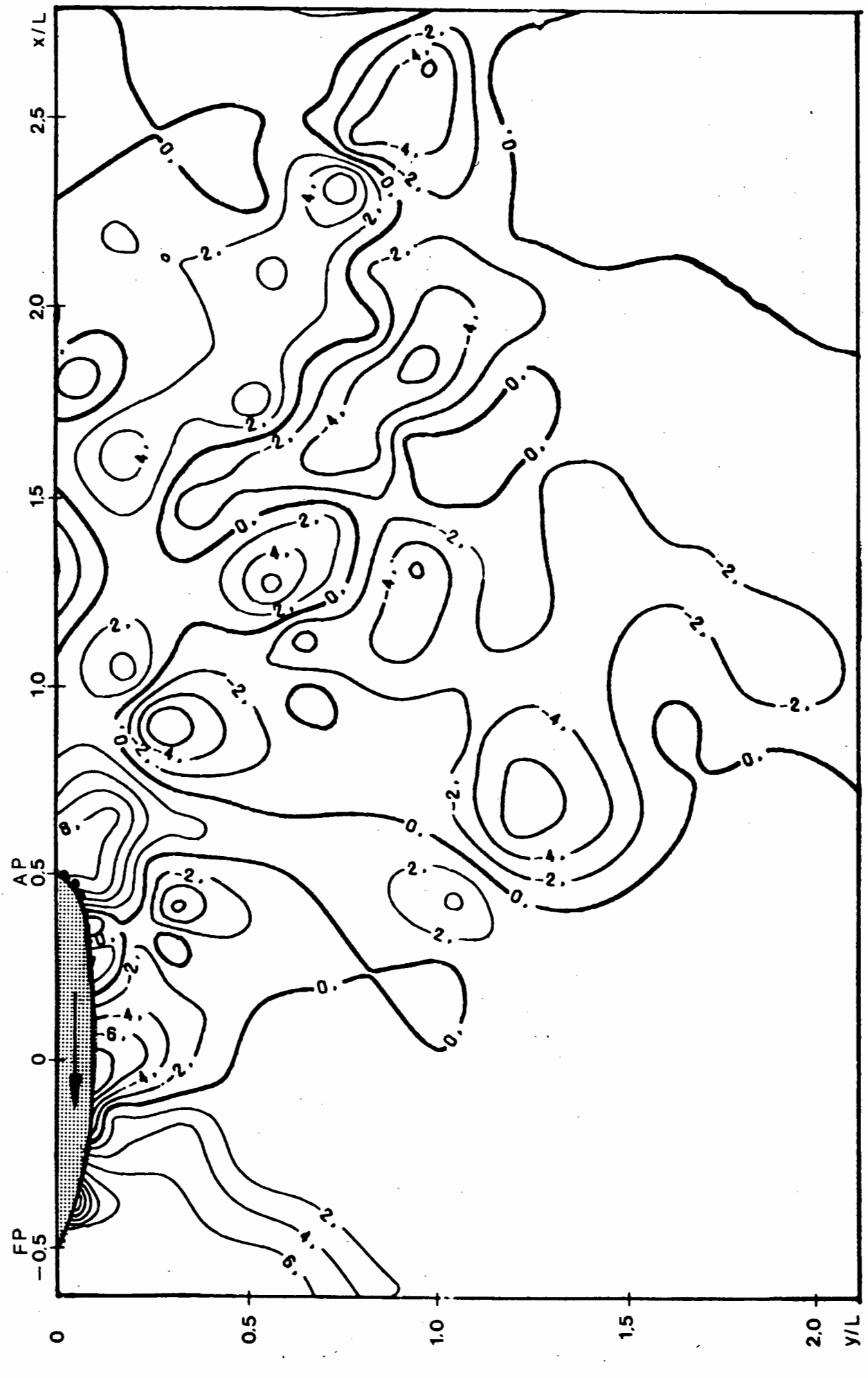

Figs 7.18: Contour map. Froude number = 0,298

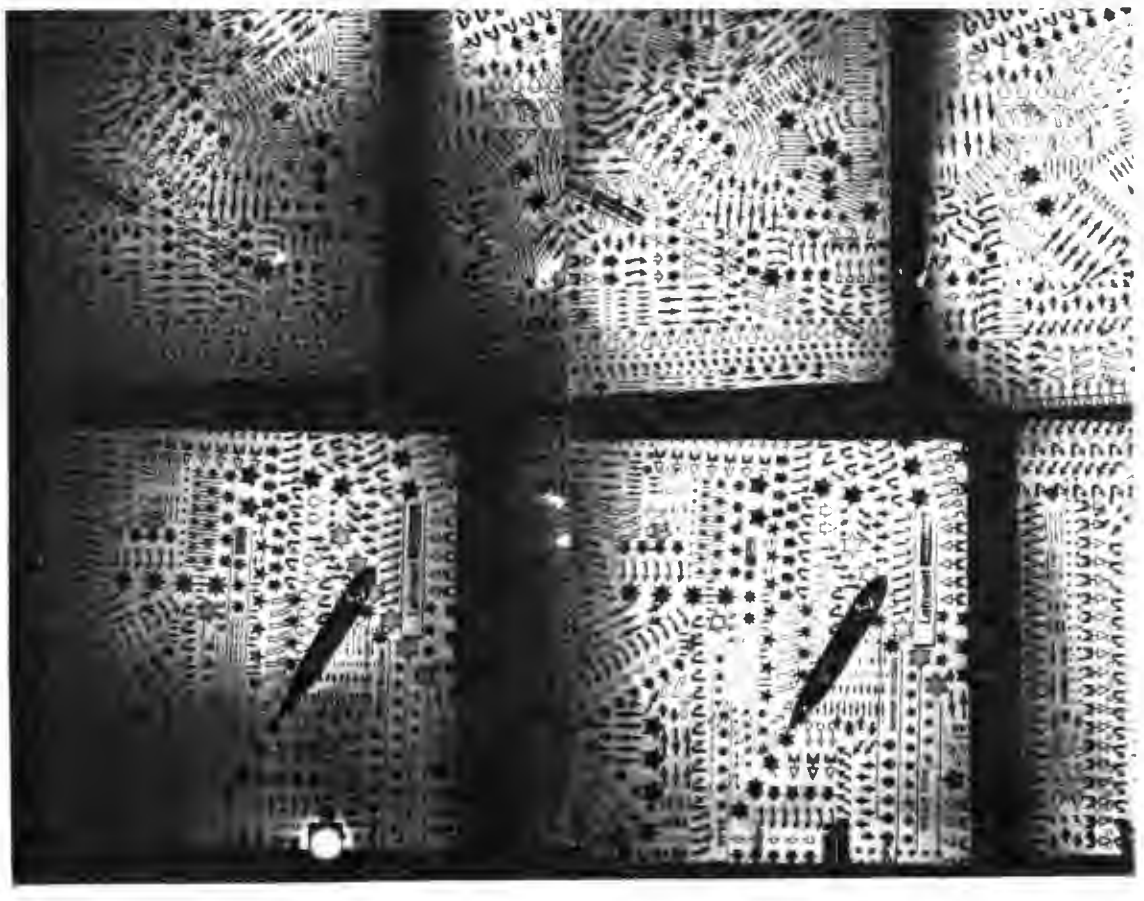

Fig. 7.19: Stereopair: Froude number = 0.298

7.4.1.6 Discussion on wave pattern analysis

The photogrammetric technique employed to determine the wave pattern contour maps proved to be extremely accurate and versatile. Above Froude values of 0,360, the wave heights are of a reasonable, easily measurable magnitude (±30 mm). Below these values the stereocomparator analysis becomes increasingly difficult and less accurate, as found for the plot of Fn = 0,298. It was observed that the spacing of the wave systems increased as the ship speed increased, reaching a maximum value of the LWL. This meant that at these speeds the wave systems were beginning to feel the effects of the seabed. Comparing the wavelengths of Fn = 0,407 and Fn = 0,441 it can be estimated that at Fn = 0,42 the wave system is no longer a fully deep water pattern. This can be translated into a depth Froude number as follows:

$$F_d = \frac{(\text{critical velocity for } d/L = 0,5)}{gd}$$

$$= 0,620$$

Therefore at depth Froude number of greater than 0,62 the wave system will become increasingly shallow in nature. This is an interesting result and shows that the wavelength to be used when determining the onset of shallow/deep water conditions is not the 0,9LWL as given by Blevins (1984) but the transverse wavelength, L, of the generated wave system.

The cusp line or intersection of transverse and divergent waves all remained constant over the speed range, although being less evident at the high speeds due to the further spacing of the wave systems.

7.4.2 Analysis of wave resistance results

The five results obtained for the wave energy analysis are presented in Fig. 7.20. The values are compared with past results obtained by Ward (1964) using the X-Y method and Tsai (1978) using a longitudinal cut approach for two different size models. All the results are for the Series 60, C_B = 0,60 parent ship form. The results are as indicated on the graph key, the solid line representing the residual resistance curve of Fig. 7.4.

The published values of C_w all lie below the residual resistance coefficient, thus validating the division of residual resistance into components of wavemaking and form drag. The Froude number can be divided into 3 ranges: (1) below 0,25; (2) between 0,25 and 0,35; and (3) above 0,35.

For Froude numbers below 0,25, the total resistance curve is very flat, the viscous resistance being some 80% of the total. Therefore in this range the viscous effects on wave resistance are very important and large discrepancies would result between C_w and $C_t - C_v$ (C_r). No data exists in this range for the wave energy analysis procedure due to the small amplitude waves generated at these speeds.

In the second Froude number range, the curves of total and wave resistance show a steeper slope up until Fn = 0,32 where the curve dips due to phase shifts of the wave system. The relative contribution of wave resistance is increasing, amounting to 20% - 40% of the total. Values obtained for Fn = 0,298 agree well with past results, lying in the same range as those of Tsai (1975) using a larger model of 3 m. At Fn = 0,34 the calculated coefficient is larger than the residual resistance curve, a result which appears to be in error as C_r is composed of $C_w + C_{form}$. If however, at this point the actual C_v, not the idealised C_f, has a corresponding local maxima, then $C_t - C_v$ will be greater than C_r.

Above Froude numbers of 0,350 the curves of wave resistance appear to have a flatter slope than the previous region, although C_r steepens due to the steepening of C_t. The results of Ward are consistently less than the present calculated values so the values for Fn = 0,407 and 0,441 appear to follow the same trend as previous speed ranges. Fn = 0,360 is above the C_r curve as Fn = 0,340 and this could be due to similar errors. The values of Fn = 0,407 and 0,441 are 40 and 15 percent higher than Ward's values. It was found that for depth Froude numbers of greater than 0,6 the basin floor interferes with the wave pattern. This could be the reason for the marked change of curvature for Fn = 0,441, the wave system losing energy due to its interaction with the seabed.

The general trends of the results are slightly higher than those reflected in past researches, the deviation increasing as the ship speed increases. There are two main possible regions of error reflected by the different results, these may be explained by differences associated with the experimental procedures and analyses and by those associated with the theoretical formulation.

Possible experimental errors could be those associated with the wave basin and thus inherent in the procedure, viz:

(i) Due to the short towing distance and rapid accelerations, the wave pattern could not have stabilised sufficiently. There

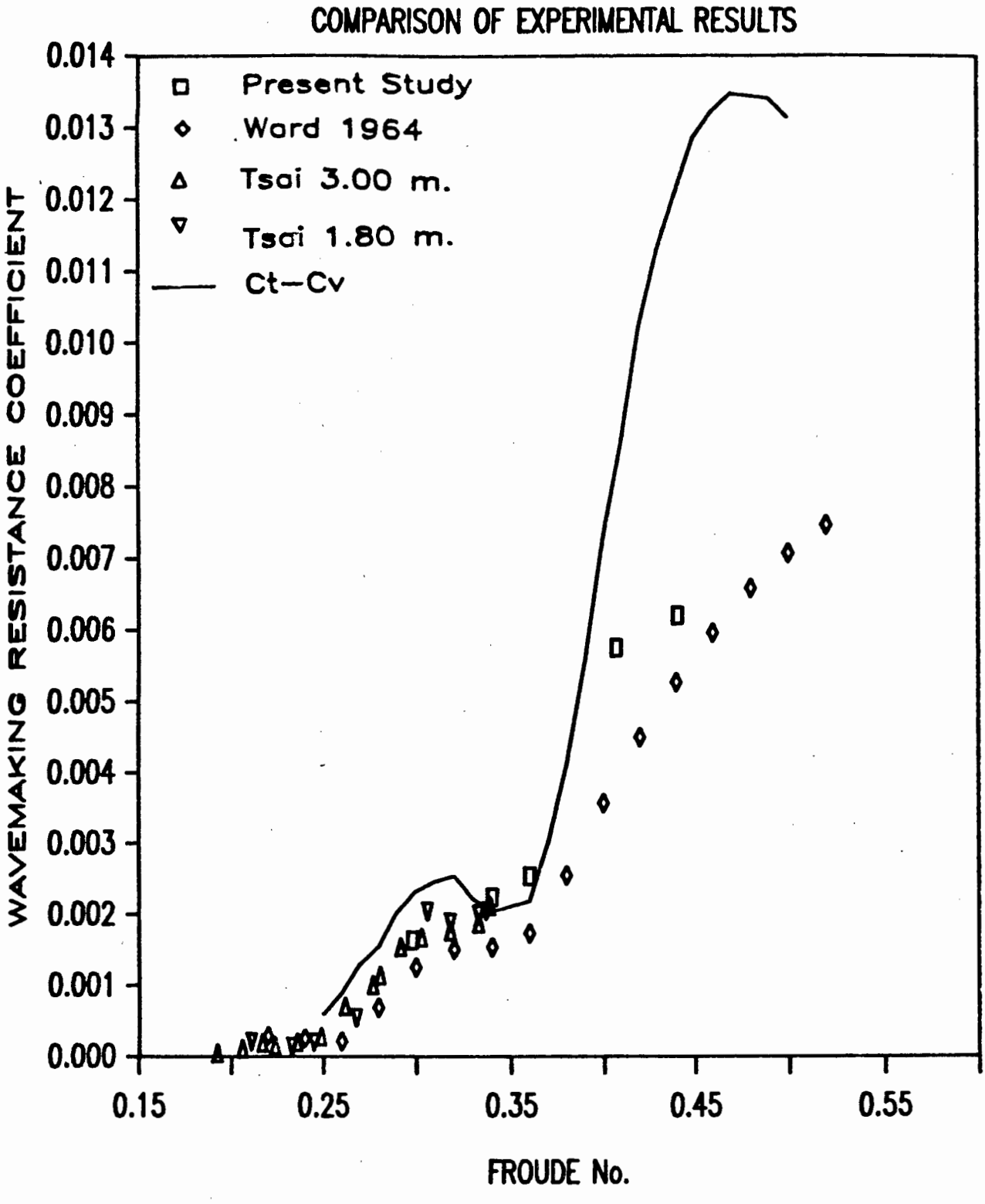

Fig. 7.20: Wave resistance of Series 60, C_B = 0,60 – comparison of experimental results

could be possible interference of the wave system resulting from the initial accelerated waves causing interferences with the wave phases of the free wave pattern in the wake of the ship.

(ii) The region of wave pattern analysed could still include near field wave pattern contributions. The energy region could only be analysed over a distance of two waterlines, starting at x/LWL = 1,5. If the wave pattern could be analysed over a greater distance astern of the model the average energy increase would be stabilised, thus giving more uniform results.

These possible errors are due to the limitations of the wave basin and therefore could not be avoided. The experimental analysis and numerical integration approach used would possibly yield lower results due to the numerical approximations made when evaluating the energy integral. Assuming the theory correct, the results are then reasonably good regarding the above possible interference factors.

Considering the theory as it stands, the question should be asked whether we are evaluating all the work done by the ship as it moves against wave making resistance? The method was derived from a purely phenomenological standpoint, the generated waves causing the wave resistance. The integral technique evaluates the wave energy being put into the fluid by the ship as it advances against wave making resistance, Rw, but does not include any energy transfer due to wave motion across the vertical plane aft of the ship, represented in Fig. 4.7 as plane II. If the wave pattern could be analysed sufficiently far astern of the ship, the energy distributions of $\bar{E}$ across the sailing line would gradually decrease to zero as the wave system dissipated. Including the additional energy contributions moving further aft, would result in successively converging values of R_w to the exact value R_w, illustrated in Fig. 7.21.

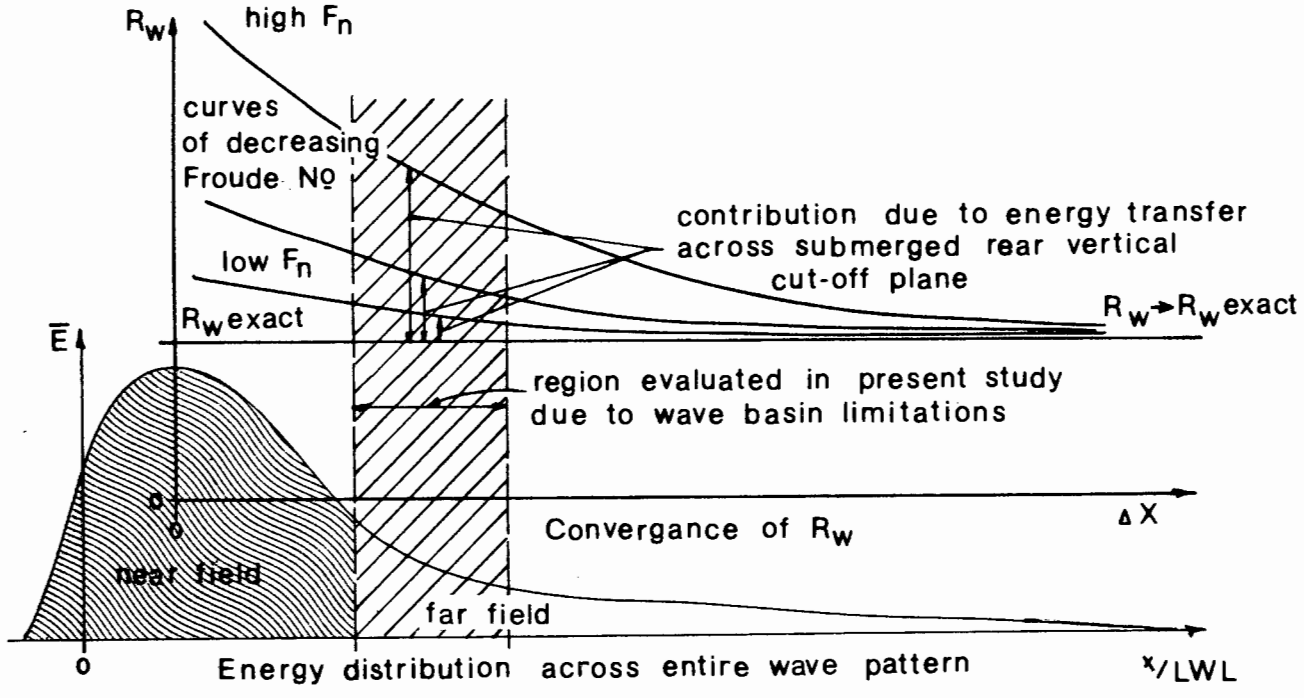

Fig. 7.21: Convergence of R_w with increasing Δx

The contribution due to the energy transfer across the vertical boundaries would correspondingly decrease due to diminishing wave amplitudes. Regarding the total wave energy denoted E_{total} as being composed of both the work done by the ship as it advances against wave resistance, R_w, denoted by W_w and additionally the work done across the rear vertical cut off plane of the fluid denoted W_v, we get the total wave energy increase over a distance Δx as:

$$E_{total}\ \Delta x = W_w\ \Delta t + W_v\ \Delta t$$
$$= R_w\ \Delta x + W_v\ \Delta t$$

Rewriting results as,

$$R_w = E_{total} - \frac{W_v}{\Delta v}$$

The present approach neglects the second term. Assuming this work component W_v is small or negligible, then the proposed method is essentially correct. If the term is significant then it can be

seen that it is dependent on the velocity of the ship, and describes the previously noted deviation from historic data. It is possible that this term includes the work done on the rear vertical plane of the fluid. If this were the case, it could not be determined experimentally as it would involve the measurement of the wave orbit kinematics throughout the water depth along this plane.

7.4.3 Hull profile measurements

Additional measurements were taken off the contour map, those of the wave profiles along the hull. These are represented in Figs. 7.22 to 7.24.

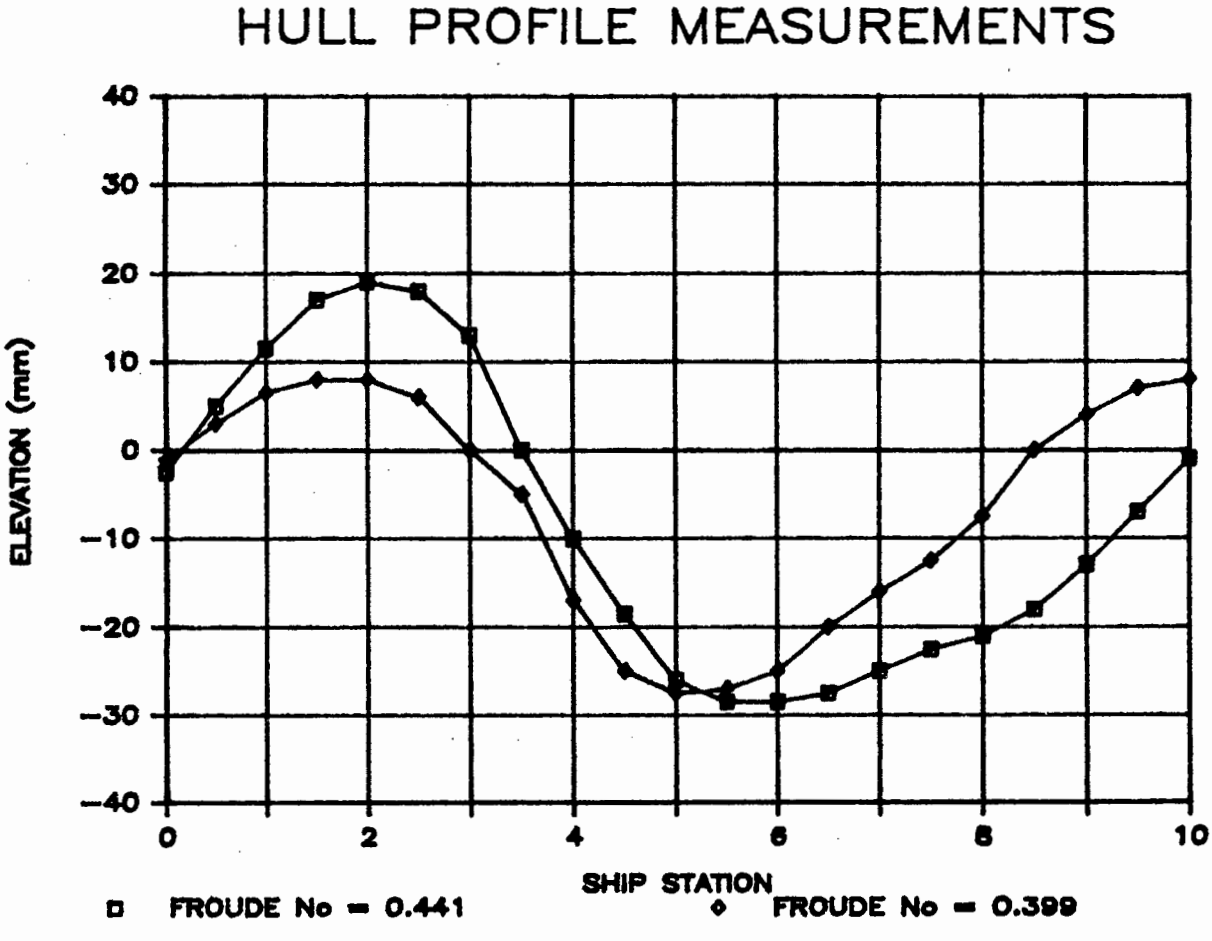

Fig. 7.22: Hull profile measurements

Fig. 7.22 represents the higher speed range above Fn = 0,35. The shift of the bow waves and increasing steepness aft of the stern can be seen on the differences between the crest positions at Froude numbers of 0,441 and 0,399. The crest has shifted approximately 55 mm aft at the higher speed. The position of the trough has similarly shifted and the stern crest is aft of the model. There is a slight step in the wave profile at station 8, demonstrating

the combined nature of the generated wave. This step is also seen at the lower speed and is more pronounced. This indicates the presence of an intermediate wave that shifts aft and disappears as the wavelength and speed increase. The wavelengths are easily seen at the lower speed, L = 903 mm, if compared with the approximated 950 mm at Fn = 0,407. For Fn = 0,441 the stern peak is beyond the hull boundary, but the half wavelength is from stations 2 - 6 or 432 mm.

The increase of the wave height and steepness with speed verifies the increase of trim in this region.

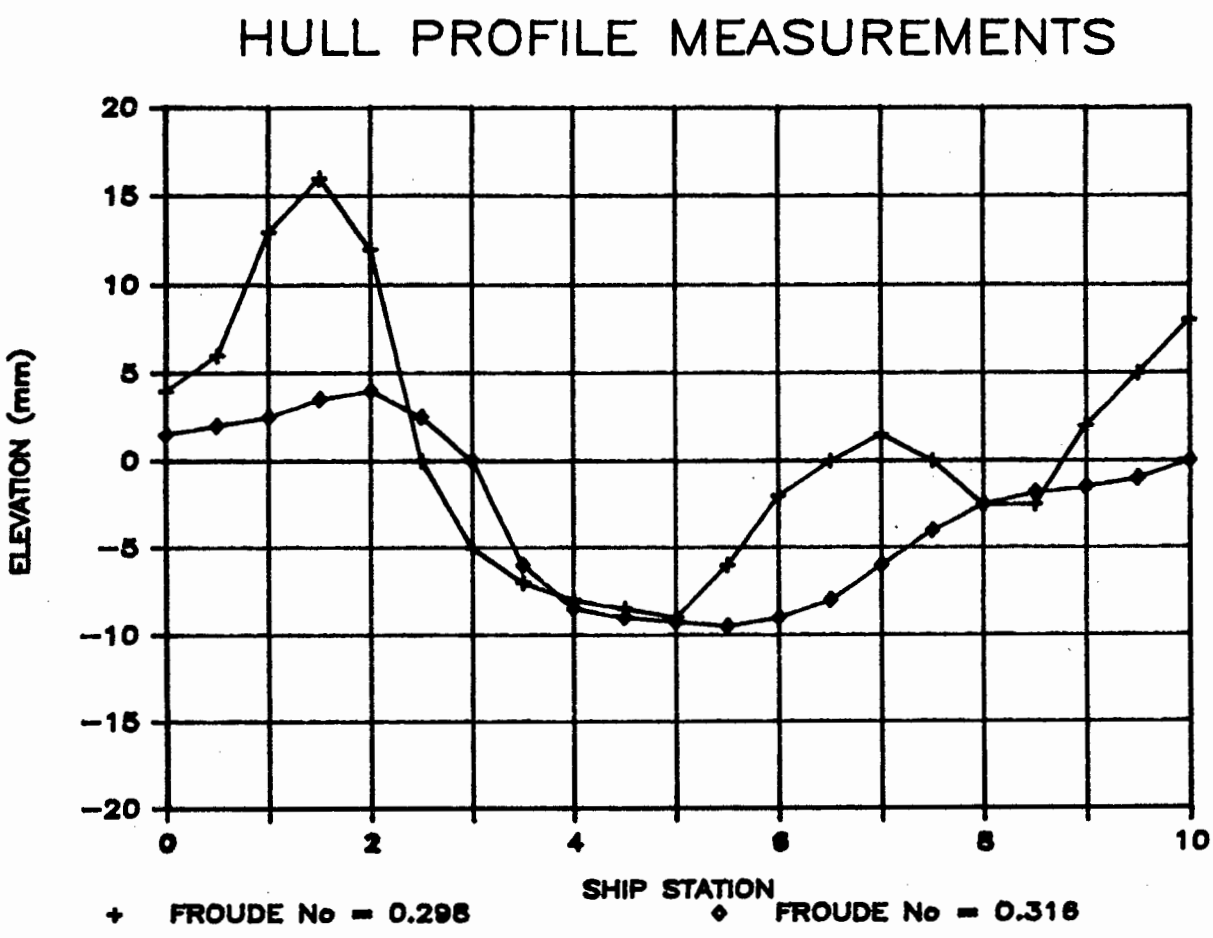

Fig. 7.23: Hull profile measurements

The Froude range between 0,30 and 0,35 is represented by Fn = 0,298 and 0,316, the hull profiles shown in Fig. 7.23. The vertical scale has been reduced to half the scale of the previous figure due to the considerably smaller amplitudes. It is interesting to note the change of profile in such a small speed interval, but this corresponds to the changes of trim and total resistance results, the trim at Fn = 0,32 being zero. The wavelength is increased as the speed increases to Fn = 0,316, the phase shift being evident and the reduction of the well developed intermediate wave at Fn = 0,298 to a step profile at Fn = 0,316. The intermediate crest shift from station 7 to 8, the bow crest shifting only 0,5 of a station. Thus the wavelength is lengthening sternwards. The steep bow wave at Fn = 0,298 corresponds to the total resistance at this point reaching a local peak. The decrease of the size of the wave at Fn = 0,316 is also evident on the total resistance curve.

Two relatively low speeds are analysed in Fig. 7.24. At Fn = 0,281 several divergent wave crests are seen along the hull. The elevations reduce considerably at Fn = 0,222, the range being only 8 mm. The maximum bow wave at Fn = 0,281 is 8 mm decreasing to a short crest 2,5 stations aft. At these elevations the results can not be considered to be truly representative due to such effects as surface tension and laminar flow conditions over the entire wetted surface.

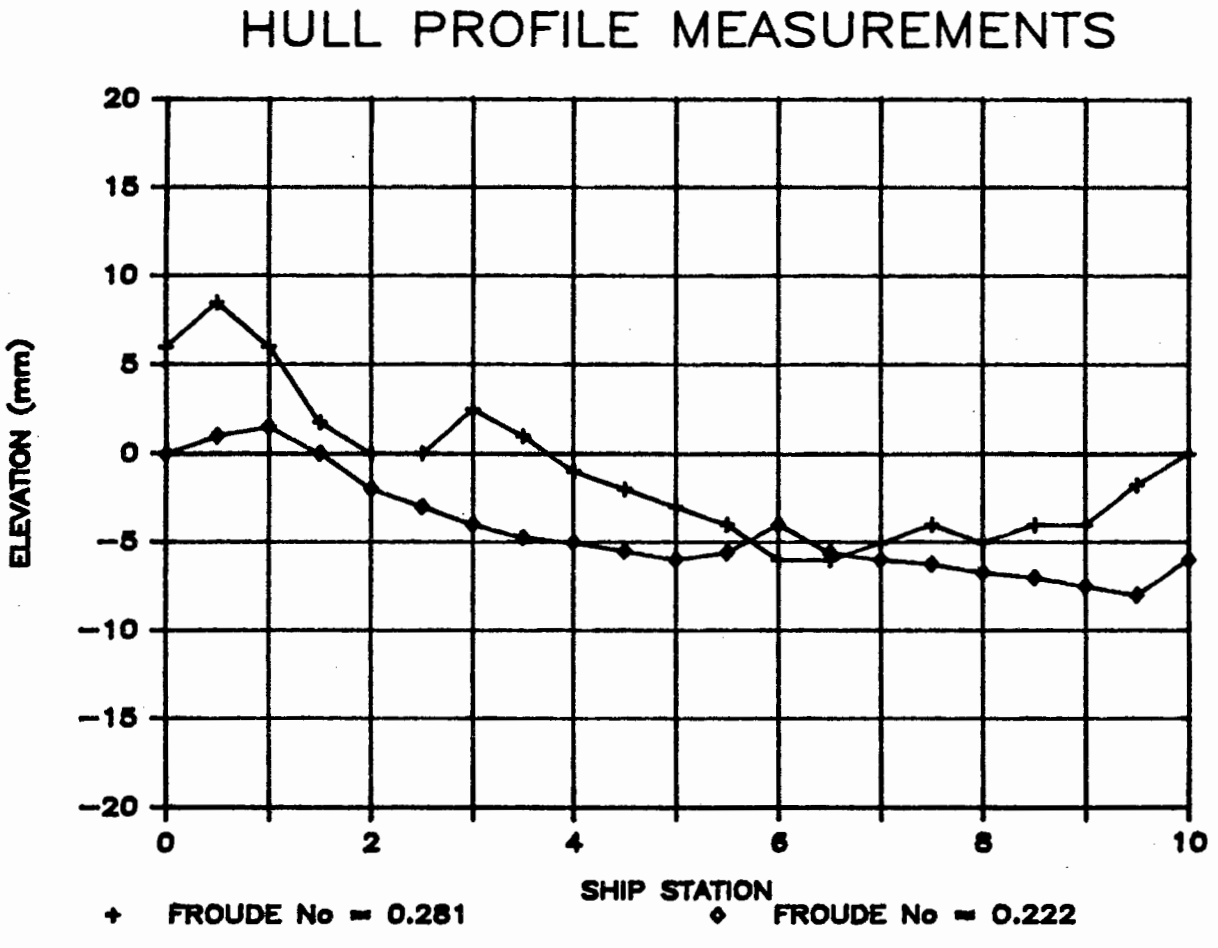

Fig. 7.24: Hull profile measurements

7.5 Descriptive wave pattern analysis

This is a brief descriptive section illustrating the observed wave patterns for 3 different ship speeds. The photographs were taken using a series of spotlights mounted along the basin wall to highlight the wave pattern by providing low angle illumination.

At lower speeds the small wave pattern surface elevations can be well studied in this manner. Figs 7.24 and 7.25 represent the wave patterns and flow conditions at Fn = 0,25. The wave pattern is remarkably similar to that of Kelvin's theory, the intersections of the cusp lines clearly seen. There are several divergent waves present along the hull, particularly in the forward region. The spacing increases further aft until the wavelength is 30% of the LWL. The small angle of trim (Fig. 7.25) is seen along with the extremely small wave profiles. There is no wave breaking and a frictional wake can be seen aft of the point of sudden curvature near the stern, being evident as slight surface turbulence. This is the beginning of the separation of the boundary layer.

Fig. 7.25: Low speed wave pattern

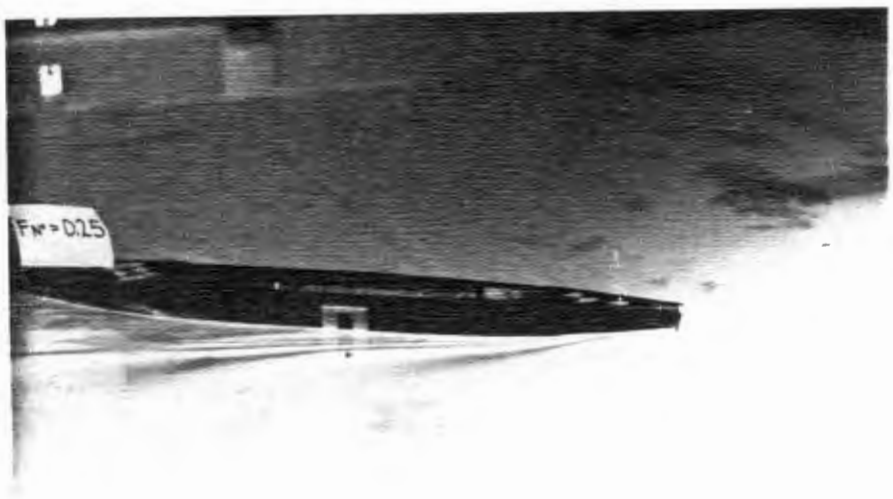

Fig. 7.26: Wave profile at Fn = 0,25

As the speed increases the amplitudes increase, as shown in Figs 7.27 and 7.28. At Fn = 0,35, the turbulence in the wake is becoming evident. The angle of the bow waves is wider than the stern wave angle, in agreement with observations by Peregrine (1971). The stern wave must pass through the boundary layer and wake to the far field, the interference of the wake possibly changing the resistance characteristics. The wavelength has increased to about 50% of the LWL, and the large intermediate diverging wave is clearly visible. The major transverse wave is evident aft of the stern. The bow wave peak has shifted aft of the stern and has steepened considerably compared with Fn = 0,25. The wave is just breaking at the crest. Turbulence has increased considerably in the wake region and the boundary layer has shifted further forward. The ship trim seems to be fairly level, both bow and stern levels being similar.

Figs 7.29 and 7.30 represent the high speed range of Fn = 0,45. Fig. 7.29 indicates the major bow and stern wave development with very small intermediate divergent waves. The wavelength has increased to more than the hull waterline length. The extent of the frictional wake has increased considerably and there is a large degree of turbulence along the hull. At the stern excessive turbu-

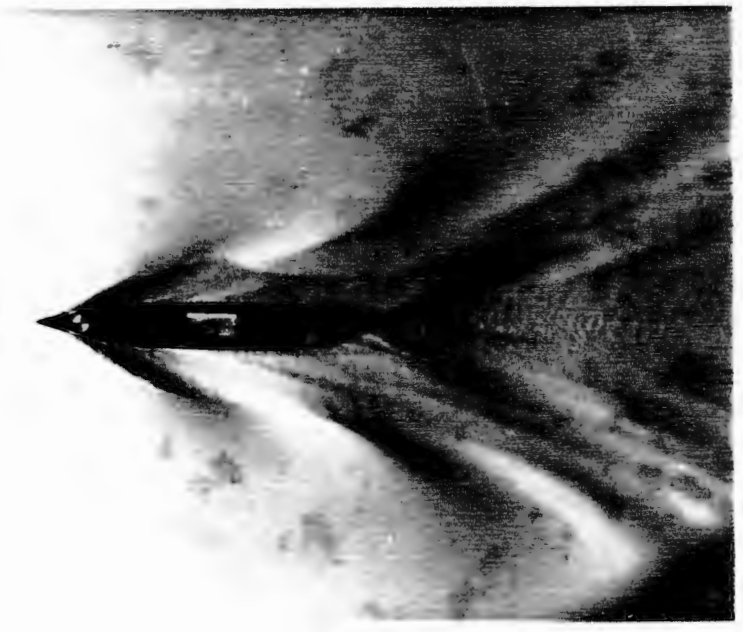

Fig. 7.27: Intermediate speed wave pattern

Fig. 7.28: Wave profile at Fn = 0,35

lence is present indicating possible separation. The trim can be clearly seen, the effect of the bow wave lifting the nose of the model, and the stern being considerably lowered into the water. Wave breaking is present all along the bow wave, thus at these speeds wave breaking resistance becomes an important consideration.

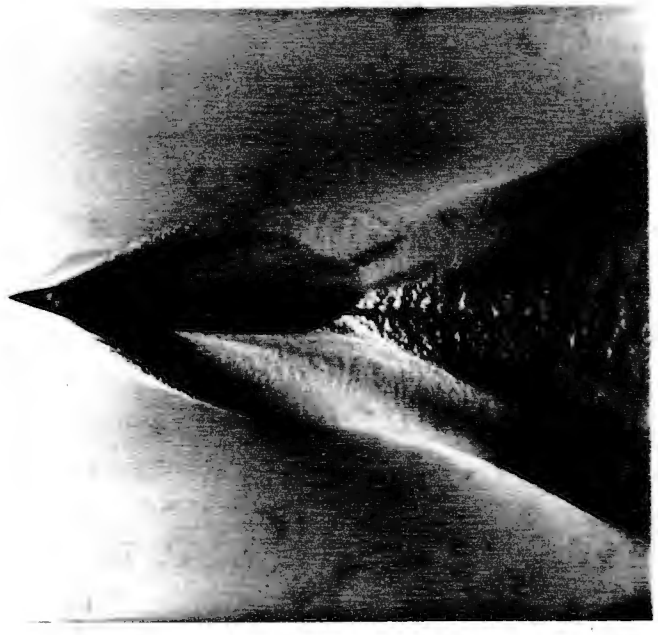

Fig. 7.29: High speed wave pattern

Fig. 7.30: Wave profile at Fn = 0,45

The model being towed across the wave basin is shown in Fig. 7.31. The familiar wave pattern composed of the divergent and transverse systems is clearly seen. This wave pattern is representative of those for all surface displacement vessels and through its analysis a better understanding of the forces involved will eventually result.

A better fundamental understanding implies an improved design philosophy which will ultimately benefit all those associated with coastal engineering and marine design problems.

Fig. 7.31: Ship generated waves

8. CONCLUSIONS

In this investigation every attempt was made to achieve results which were as precise possible. An accurate wave height measurement technique was used to obtain precise water surface elevations of ship generated wave patterns.

The results of the total resistance determination using two separate methods correspond closely to past measured data. These curve characteristics were justified by additional measurements of squat and trim, and hull wave profiles. The wave pattern and wave profiles were compared photographically and found to conform to the theoretical predictions.

The proposed energy analysis precedure was used to determine the wave resistance at five different speeds representing the full range of Froude numbers. The results are generally in good agreement with available data, but tend to be consistently higher, the deviation increasing as the speed increases. This possibly suggests a shortcoming in the theoretical proposal, neglecting a term to include the work done on the sectioned boundaries of the fluid.

Due to the confines and restrictions of the wave basin, certain discrepancies in the results are expected, but generally the measured results are fairly representative throughout.

REFERENCES

Adams, L.P. 1978 The use of photogrammetry in the study of the sea. Proceedings of the 6th Conference of South African Surveyors 6 - 10 Feb. 1978

Allan, J.F. and Conn, J.F.C. 1950 Effects of Laminar Flow on Ship Models, Trans. Roy. Inst. Naval Arch. Vol. 92 pp. 107 - 137

Atkinson, K.B. 1976 A review of close-range engineering photogrammetry. Photogrammetric Engineering and Remote Sensing Vol. 42, No. 1 pp. 57 - 69

Baba, E. 1976 Wave Breaking Resistance of Ships. Int. Seminar in Wave Resistance, Tokyo; The Society of Naval Architects of Japan Vol. 1, pp. 75 - 93

Barass, C.B. 1978 The Phenomena of Ship Squat. Lorne and MacLean Marine Publications, England

Barnaby, K.C. 1969 Basic Naval Architecture. Hutchinson & Co., London

Blevins, R.D. 1984 Applied Fluid Dynamics Handbook. Van Nostrand Reinhold and Company

Bober, W. and Kenyon, R.A. 1980 Fluid Mechanics John Wiley and Sons, Inc.

Chan, R.K.C. and Chan, W.K. 1979 Non Linear calculations of a three dimensional potential flow about a ship, Proc. of the Workshop on Ship Wave Resistance Computation, DTNSRDC, U.S.A. pp 420 - 434

Cooke, R. 1986 An Experimental Investigation into Ship Resistance Components. University of Cape Town, M.Sc.

Dagan, G. 1975 Waves and Wave resistance of thin bodies movings at low speed; the free surface non-linear effect. Journal of Fluid Mechanics Vol. 69, part 3, pp. 405 - 416

Eggers, K.W.H., Sharma, S.D. and Ward, L.W. 1967 An assessment of Some Experimental methods for determining the Wavemaking Characteristics of a form. Trans. Society of Naval Architects and Marine Engineers; Vol. 79 pp 112 - 158

Eggers, K.W.H. 1976 "Wave analysis, state of the art, 1975" Int. Seminar in Wave Resistance, Tokyo; The Society of Naval Architects of Japan, pp 93 - 107

Froude, W. 1874-1900 The papers of William Froude. The Institution of Naval Architects, London.

Gadd, G.E. 1973 "Wave resistance calculations by Guilloton's Method." Trans. Roy. Inst. Naval Arch., Vol. 115, pp. 377 - 384

Gadd, G.E. 1975 "A method of computing the flow and surface wave pattern around full forms." Trans. Roy. Inst. Naval Arch., Vol. 117 pp.207 - 219

Gillmer, T. 1975 Modern Ship Design, Naval Institute Press, U.S.A. pp. 95 - 185

Grigson, C.W.B. 1983 "On predicting the performance of ships from models." Trans. Roy. Inst. Naval Arch., Vol. 125 pp. 125 - 139

Hong, Y.S. 1983 Computation of Non Linear Wave Resistance. Proceedings of the second DTNSRDC on Ship Wave Resistance computations, U.S.A., pp. 104 - 127

Inui, T. 1962 Wave making resistance of ships. Trans. Society of Naval Architects and Marine Engineers, Vol. 70 pp. 283 - 354

Kawamura, N., Kajitani, H., and Tsuchiya, Y. 1980 Experimental Investigation on the Resistance Component due to Free Surface Shock Waves on Series Ship Models. Journal of Kansai Society of Naval Architects, Vol. 179, pp. 45 - 55

Kilner, F.A. 1984 Wave Motion and Transformation. Lecture notes, Department of Civil Engineering, U.C.T.

Kobus, H.E. 1967 Examination of Eggers relationship between transverse wave profiles and wave resistance. Journal of Ship Research Vol. 11 pp. 240 - 256

Kreyzig, E. 1979 Advanced Engineering Mathematics Fourth Edition, John Wiley and Sons

Lackenby, H. 1962 Resistance of Ships, with special reference to skin friction and hull surface condition. The Institution of Mechanical Engineers, Vol. 176 pp. 981 - 1014

Lackenby, H. 1965 An investigation into the nature and interdependence of the components of ship resistance. Trans. Roy. Inst. Naval Arch. Vol. 107 pp. 474 - 496

Landweber, L. and Tzou, K.T.S. 1968 Study of Eggers Method for determination of wave making resistance. Journal of Ship Research Vol. 12 pp. 213 - 230

Landweber, L. and Patel, V.C. 1979 Ship Boundary Layers. Annual Review of Fluid Mechanics Vol. 11 pp. 173 - 207

Matheson, N. and Joubert 1973 Experimental Determination of the Components of Resistance of a small 0,80C_B Tanker Model. Journal of Ship Research Vol. 17, No. 3, pp 162 - 180

Miyata, H. and Inui, T. 1984 Non Linear Ship Waves, Advances in Applied Mechanics, Vol. 24 pp. 214 - 288

Moffitt, F.H. 1968 Wave Surface Configuration, Photogrammetry Engineering, Vol. 34 pp. 179 - 188

Moran, D.D. 1971 Experimental Procedure for the determination of Wave Resistance in a towing tank. Iowa Institute of Hydraulic Research pp. 1 - 88

Moran, D.D. and Landweber, L. 1972 A longitudinal cut method for determining wave making resistance. Journal of Ship Research Vol. 16, No. 1, pp.21 - 40

Nakatake, K., Toshima, A. and Yamazaki, R. 1979 Wave resistance calculation for Wigley, S201 and Series 60 Hulls. Proc. of the Workshop on Ship Wave Resistance Computation, DTNSRDC, U.S.A. pp. 215 - 231

Newman, J.N. 1963 The determination of Wave Resistance from wave measurements along a parallel cut. Proceedings In. Seminar on Theroetical Wave Resistance, Michigan pp. 351 - 377

Newman, J.N. 1976 Linearized Wave Resistance theory. Int. Seminar in Wave Resistance, Tokyo; The Society of Naval Architects of Japan pp 31 - 43

Nishimura, S., Miyata, H. and Kajitani, H. 1985 Finite difference Simulation of Ship Waves by the TUMMAC-IV Method and its applications to hull form design. The Society of Naval Architects of Japan Vol. 157 pp. 1 - 14

Noblesse, F. 1984 Convergence of a sequence of slender ship, low Froude number approximations. Journal of Ship Research Vol. 28, No. 3, pp. 155 - 162

Paterson, A.J.C. 1984 The Analysis of ship bow and stern wave patterns using close range photogrammetry. B.Sc Thesis, Dept of Civil Engineering, U.C.T.

Peregrine, D.H. 1971 A ship's waves and its wake. Journal of Fluid Mechanics Vol. 49, No. 2, pp. 353 - 360

Pos, J.D. and Kilner, F.A.K. 1982 Laboratory photogrammetric wave height measurement. Proceedings of the 18th International Conference of Coastal Engineers Cape Town pp. 295 - 709

Pos, J.D. 1984 A Study of Breakwater Gap Wave Diffraction using close range photogrammetry and finite and infinite elements. University of Cape Town, Ph.D

Schuring, D.J. 1977 Scale Models in Engineering. Pergamon Press

Shearer, J.R. and Cross, J.J. 1965 The Experimental Determination of the components of Ship Resistance for a Mathematical Model. Trans. Roy. Inst. Naval Arch. Vol. 107, pp. 45 - 473

Sorenson, R.M. 1967 Investigation of ship generated waves. Journal of Waterways and Harbour Division, AISCE pp. 85 - 99

Sorenson, R.M. 1973 Water Waves produced by Ships. Journal of Waterways and Harbour Division, AISCE, pp. 245 - 255

Standing, R.G. 1974 Phase and amplitude discrepancies in the surface wave due to a wedge ended hull form. Journal of Fluid Mechanics Vol. 62, No. 4, pp. 625 - 642

Stoker, J.J. 1957 Water Waves. Pure and applied Mathematics Vol. 4, Interscience Publishers Inc., New York

Tatinclaux, J.C. 1975 On the Wave Resistance of Surface-Effect Ships. Trans. Society of Naval Architects and Marine Engineers Vol. 83 pp. 51 - 66

Thomas, G, and Finney, R.L. 1979 Calculus and Analytic Geometry Fifth Edition, Addison - Wesley Publishing Co.

Todd. F.H. 1973 'Viscous Resistance of Ships' Advances in Hydroscience, Vol. 3 pp. 1 - 63

Torlegard, A.K.I. 1976 State-of-the-art of close range photogrammetry. Photogrammetric Engineering and Remote Sensing, Vol. 142, No. 1, pp. 71 - 79

Townsin, R.L. 1968 Viscous drag from a Wake Survey. Measurements in the wake of a 'Lucy Ashton' Model. Trans. Roy. Inst. Naval Arch. Vol. 110

Townsin, R.L. 1971 The Viscous drag of a 'Victory' Model. Results from Wake and Wave Pattern Measurements. Trans. Roy. Inst. Naval Arch. Vol. 113 pp. 307 - 321

Tsai, C.E. and Landweber, L. 1975 Further development of a procedure for determination of ship wave resistance from Longitudinal Cut surface profile measurements. Journal of Ship Research Vol. 19, No. 2 pp. 65 -75

Tsutsumi, T. 1979 Calculation of the wave resistance of ships by the Numerical solution of the Neuman-Kelvin problem. Proc. of the Workshop on Ship Wave Resistance Computation, DTNSRDC, U.S.A. Vol. 1 pp. 162 - 201

Tulin, M.P. 1976 Ship Wave Resistance, a Survey. U.S. Dept of Commerce, NTIS. pp. 1 - 76

Tulin, M.P. 1980 Wave Resistance, State of the art 1980. Proceedings of the continued Workshop on Ship Wave Resistance pp. 5 - 29

Ward, L.W. 1968 Experimental determination of the Wave Resistance of a Ship Model from lateral Wave-Slope Measurements. Webb Institute of Naval Architecture. New York.

Ward, L.W. and Snyder, J.D. 1968 Forces due to gravity waves on a long vertical circular cylinder. Webb Institute of Naval Architecture, New York.

Wehausen, J.V. 1973 The Wave Resistance of Ships. Advances in Applied Mechanics, Vol. 13 pp. 93 - 247

Yokoo, K. and Tanaka, H. 1976 Application of wave analysis to Tank Experiments. Int. Seminar in Wave Resistance, Tokyo; The Society of Naval Architects of Japan Vol. 1 pp. 107 - 124

APPENDIX A

Series 60, C_B = 0,60

Model Lines Plan

SERIES 60, C_B = 0,60 TABLE OF OFFSETS

from "Conference on Ship Wave Resistance Computations", held at Bethesda, Maryland, USA, 1979.

Half breadths of waterline given as fraction of maximum beam on each waterline

Model = 4210W
W.L. 1.00 is the designed load waterline

Forebody prismatic coefficient = 0.581
Afterbody prismatic coefficient = 0.646
Total prismatic coefficient = 0.614

		Waterlines							Area as fraction of max. area to
Sta.	Tan.	0.075	0.25	0.50	0.75	1.00	1.25	1.50	1.00 W.L.
FP	0.000	0.000	0.000	0.000	0.000	0.000	0.020	0.042	0.000
½	0.009	0.032	0.042	0.041	0.043	0.051	0.076	0.120	0.042
1	0.013	0.064	0.082	0.087	0.090	0.102	0.133	0.198	0.085
1½	0.019	0.095	0.126	0.141	0.148	0.160	0.195	0.278	0.135
2	0.024	0.127	0.178	0.204	0.213	0.228	0.270	0.360	0.192
3	0.055	0.196	0.294	0.346	0.368	0.391	0.440	0.531	0.323
4	0.134	0.314	0.436	0.502	0.535	0.562	0.607	0.683	0.475
5	0.275	0.466	0.589	0.660	0.691	0.718	0.754	0.804	0.630
6	0.469	0.630	0.733	0.802	0.824	0.841	0.862	0.889	0.771
7	0.666	0.779	0.854	0.906	0.917	0.926	0.936	0.946	0.880
8	0.831	0.898	0.935	0.971	0.977	0.979	0.981	0.982	0.955
9	0.945	0.964	0.979	0.996	1.000	1.000	1.000	1.000	0.990
10	1.000	1.000	1.000	1.000	1.000	1.000	1.000	1.000	1.000
11	0.965	0.982	0.990	1.000	1.000	1.000	1.000	1.000	0.996
12	0.882	0.922	0.958	0.994	1.000	1.000	1.000	1.000	0.977
13	0.767	0.826	0.892	0.962	0.987	0.994	0.997	1.000	0.938
14	0.622	0.701	0.781	0.884	0.943	0.975	0.990	0.999	0.863
15	0.463	0.560	0.639	0.754	0.857	0.937	0.977	0.994	0.750
16	0.309	0.413	0.483	0.592	0.728	0.857	0.933	0.975	0.609
17	0.168	0.267	0.330	0.413	0.541	0.725	0.844	0.924	0.445
18	0.065	0.152	0.193	0.236	0.321	0.536	0.709	0.834	0.268
18½	0.032	0.102	0.130	0.156	0.216	0.425	0.626	0.769	0.187
19	0.014	0.058	0.076	0.085	0.116	0.308	0.530	0.686	0.109
19½	0.010	0.020	0.020	0.022	0.033	0.193	0.418	0.579	0.040
AP	0.000	0.000	0.000	0.000	0.000	0.082	0.270	0.420	0.004
Max half beam*	0.710	0.866	0.985	1.000	1.000	1.000	1.000	1.000	

*As fraction of maximum load waterline beam.

Series 60, C_B = 0,60

Lines Plan

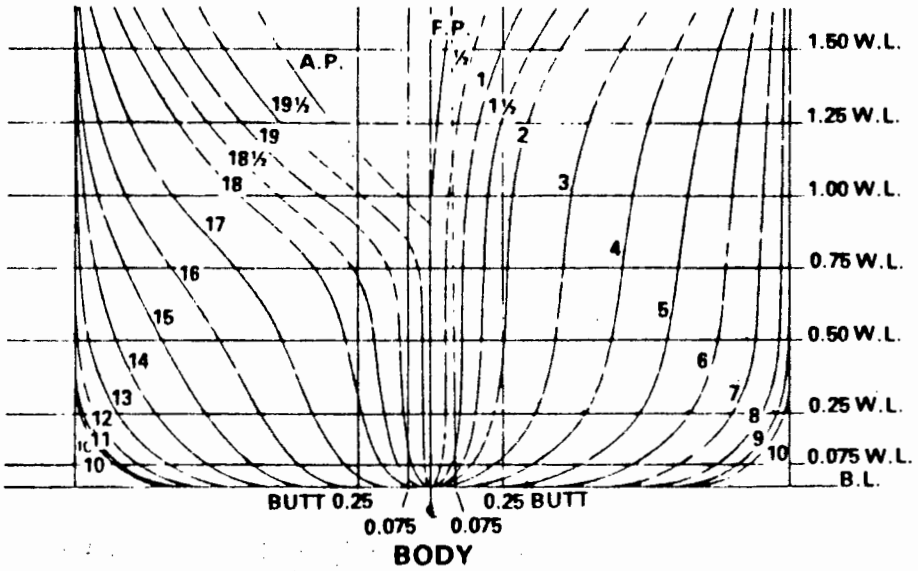

BODY

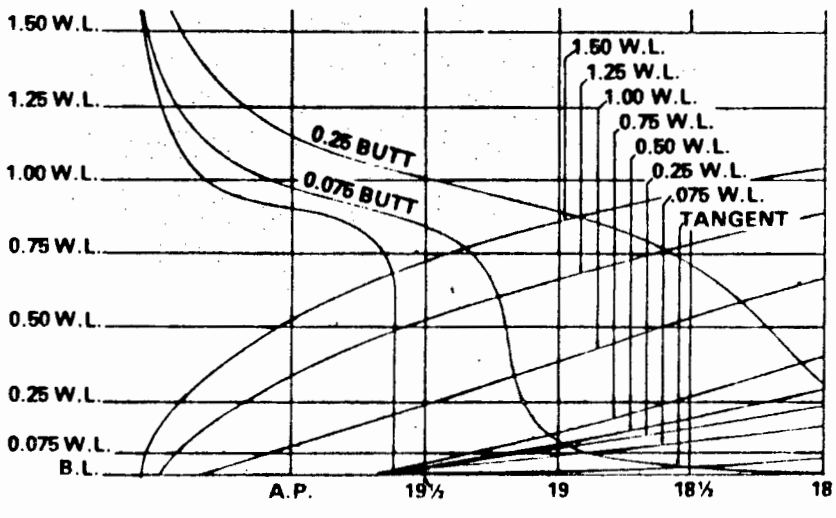

STERN

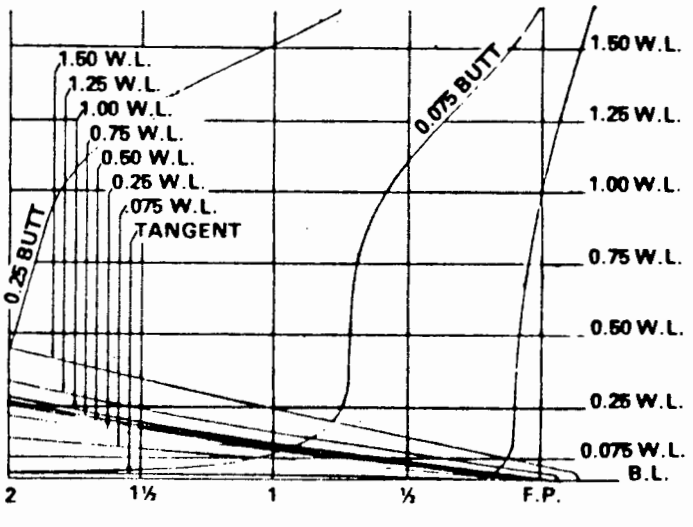

BOW

APPENDIX B

EXAMINATIONS WRITTEN BY THE AUTHOR TO COMPLETE THE REQUIREMENTS OF THE DEGREE

Examination			Credit Rating
CE5B17	Finite Element Analysis	(July 1985)	4
P.O.1a	Physical Oceanography 1a	(July 1985)	5
P.O.1b	Physical Oceanography 1b	(July 1985)	5
CIV519X	Advanced Hydraulic Structures	(November 1985)	5
CIV516F	Coastal Hydraulics	(November 1985)	5
Thesis:	"A Study of Ship Wave Resistance from an Analysis of the Wave Pattern using Close Range Photogrammetry"		20
		TOTAL	44
	Credit requirements for degree		40

UNIVERSITY OF CAPE TOWN

DEPARTMENT OF CIVIL ENGINEERING

FINAL EXAM. MONDAY, 24 JUNE 1985

CE 5B17 : FINITE ELEMENT ANALYSIS

TIME : 3 hours

Note:

The student may refer to class notes and assignments.

1. The diagram shows half a plane symmetric frame structure, which is to be modelled using 5 elements.

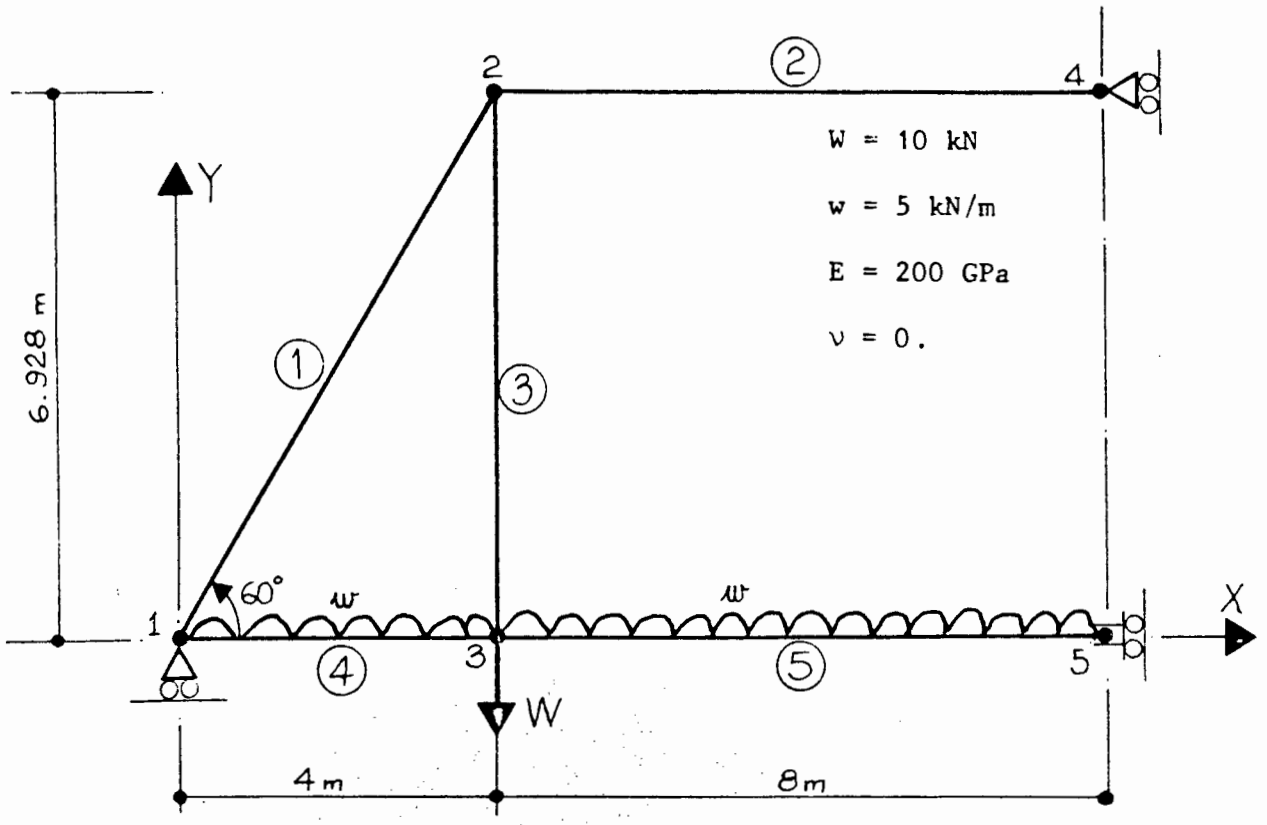

Element 1,2 : linear bar ; $A = 5000\ mm^2$

3 : Bernoulli-Euler beam ; $A = 30000\ mm^2$

$I = 50 \times 10^6\ mm^4$

4,5 : linear Timoshenko beam ; $A = 125000\ mm^2$

$I = 2600 \times 10^6\ mm^4$

$\alpha = 1.2$

(i) Compute the <u>global</u> element stiffness matrices for elements 1, 3 and 4 .

(20)

(ii) Comment <u>briefly</u> on the relative stiffnesses contained in these element matrices.

(3)

(iii) Assemble elements 1 and 4 <u>only</u> into the global system stiffness matrix; show only what is necessary, i.e. nodes 1, 2 and 3 .

(5)

(iv) Compute the global system load vector.

(5)

(v) Assume the following displacement solution (mm and rads) :

Node	u	v	θ
1	0.010	0.	-1.0×10^{-6}
3	0.012	-0.001	-0.5×10^{-6}

Using this solution compute the shear force and bending diagrams for element 4 .

(12)

2. A 5-noded quadrilateral plane stress element is shown below. Side 2-5-3 is curved.

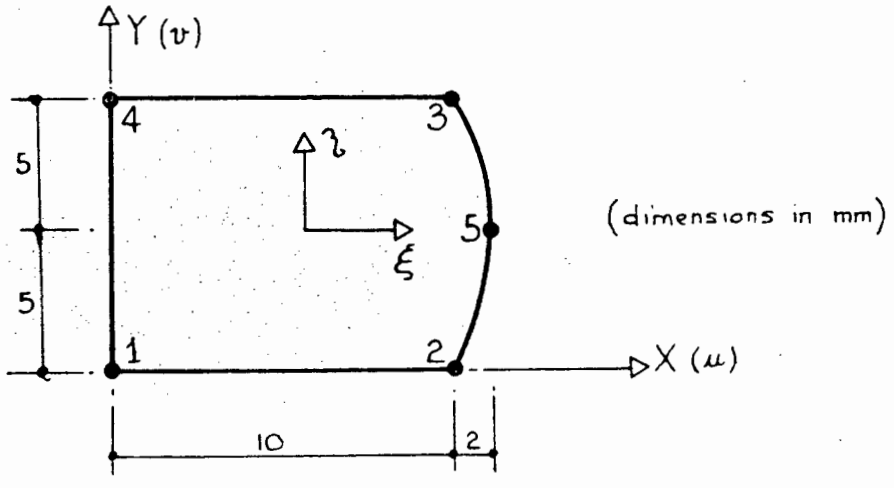

(i) Show that the Jacobian matrix for this element is :

$$J_{11} = 6 - \eta^2 \qquad J_{12} = 0$$

$$J_{21} = -2\eta(1 + \xi) \qquad J_{22} = 5$$

(10)

(ii) For a thickness $t = 1$ mm , compute the volume of the element using exact numerical integration.

(5)

(iii) Show that the normal strain along the side 3-4 is a constant with magnitude

$$\varepsilon_{xx} = 0.1\ (u_3 - u_4)$$

(10)

Note: You may request the element shape functions if you do not have them in your notes.

3. A parabolic shear load is applied across the edges of two 8-node quadrilateral elements as shown in the diagram.

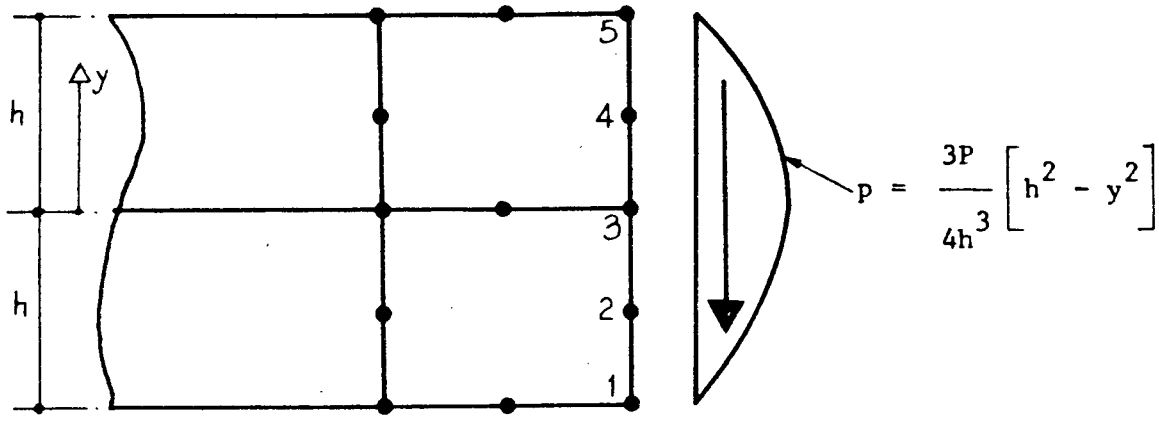

Show that the equivalent nodal load at node 3 is (11/40)P .

(15)

4. A 4-node quadrilateral element and a 2-node bar element together support a point load P = 6000N . Nodes 1, 3 and 4 are fully restrained, and node 2 can only move horizontally.

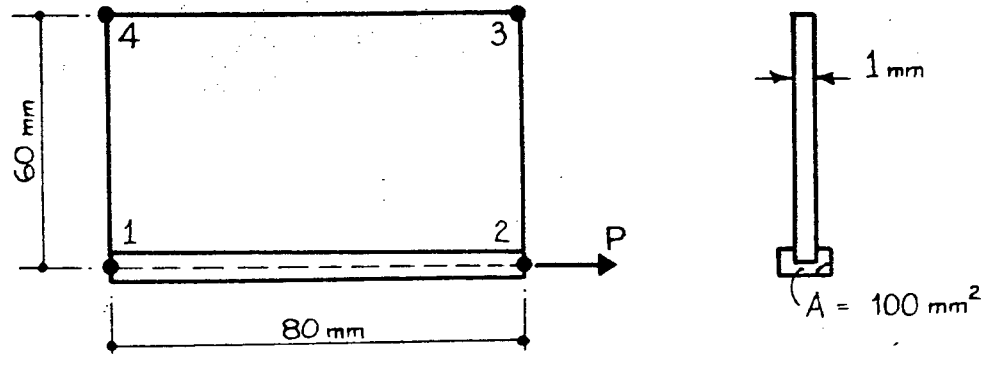

The following additional information is given :

$$\frac{\partial N_2}{\partial x} = \frac{1}{16}(1-\eta) \quad ; \quad \frac{\partial N_2}{\partial y} = -\frac{1}{12}(1+\xi)$$

$$\underset{\sim}{J} = \begin{bmatrix} 4 & 0 \\ 0 & 3 \end{bmatrix} \quad ; \quad E = 300 \text{ GPa} \; ; \quad \nu = 0.3$$

Compute the horizontal displacement at node 2.

(15)

UNIVERSITY OF CAPE TOWN - JUNE EXAMINATION 1985

PHYSICAL OCEANOGRAPHY 1a

TIME: 3 HOURS TOTAL MARKS: 150

Answer ALL questions in SECTION A

Answer TWO questions EACH from SECTION B and SECTION C

Use separate books for Sections B and C.

Section A

Answer ALL questions in this section.

1. Define a barotropic current. (2)

2. Briefly explain the Coriolis force. (2)

3. Sketch a reversing thermometer and explain how it is used. (2)

4. Describe three different instruments used to determine temperature at different depths. (3)

5. Define the terms: potential temperature, salinity, sigma-t, specific volume anomaly, standard ocean. (5)

6. What is the solar constant? (1)

7. What is black body radiation? (1)

8. What are the units of pressure? geopotential? (2)

9. Give examples (with sketches) of fronts in the atmosphere and ocean. (2)

10. What is a Kelvin wave? (1)

11. What three factors are required in order for waves to be present. (3)

12. What is a wave spectrum? (2)

13. What do you understand by "dispersion of water waves" (1)

14. What is the diurnal inequality of the tide - when does it vanish? (1)

15. What are typical oxygen concentrations in the sea? (1)

16. What is the temperature and salinity of Antarctic Bottom Water? (1)

Section B

Answer TWO questions ONLY from this section.

(i) Describe briefly, with sketches where necessary, the surface wind systems around southern Africa. Distinguish between winter and summer circulation patterns and draw surface pressure maps typical of winter and summer. (30)

(ii) Describe briefly the major surface currents around southern Africa. Draw a map of the surface currents and indicate the major topographic features in relation to the currents. (30)

(iii) Given that there is no global gain or loss of heat in the ocean, write down the heat balance equation for the ocean. Describe the various terms and give the magnitude. Pay particular attention to the detail of how the solar radiation reaches the sea surface. (30)

(iv) Describe the circulation and water masses in a section from pole to pole through the Atlantic ocean. Describe the circulation in a vertical section from pole to pole through the atmosphere. What is the jet stream and where can it be found? (30)

Section C

Answer TWO questions ONLY from this section.

(a) Small amplitude gravity waves can be found as a solution to the relevant equations, provided that the dispersion relation holds:

$$\sigma^2 = gk \tanh(kd)$$

where $\sigma = \frac{2\pi}{T}$, T the period of the waves

$k = \frac{2\pi}{L}$, L the wavelength of the waves

g = 10 m/s, d is the depth of water.

Define the terms for "deep" and "shallow" water waves and give the approximate relations for the speed of deep and shallow water waves. (12)

Given that the period T of the waves is independent of the water depth, discuss what happens when gravity waves approach the beach. (12)

If there is a long wave with a wavelength of 1000 km, what will its speed be in water of 4 km depth? (6)

(b) Assuming simple tidal theory, discuss how the tides are generated in principle by the sun and moon. Which tide producing force dominates?

Consider the following tidal record for Simons Bay carefully and discuss various features of the tide there. Expand your discussion to include details of tides around the south African coast. (30)

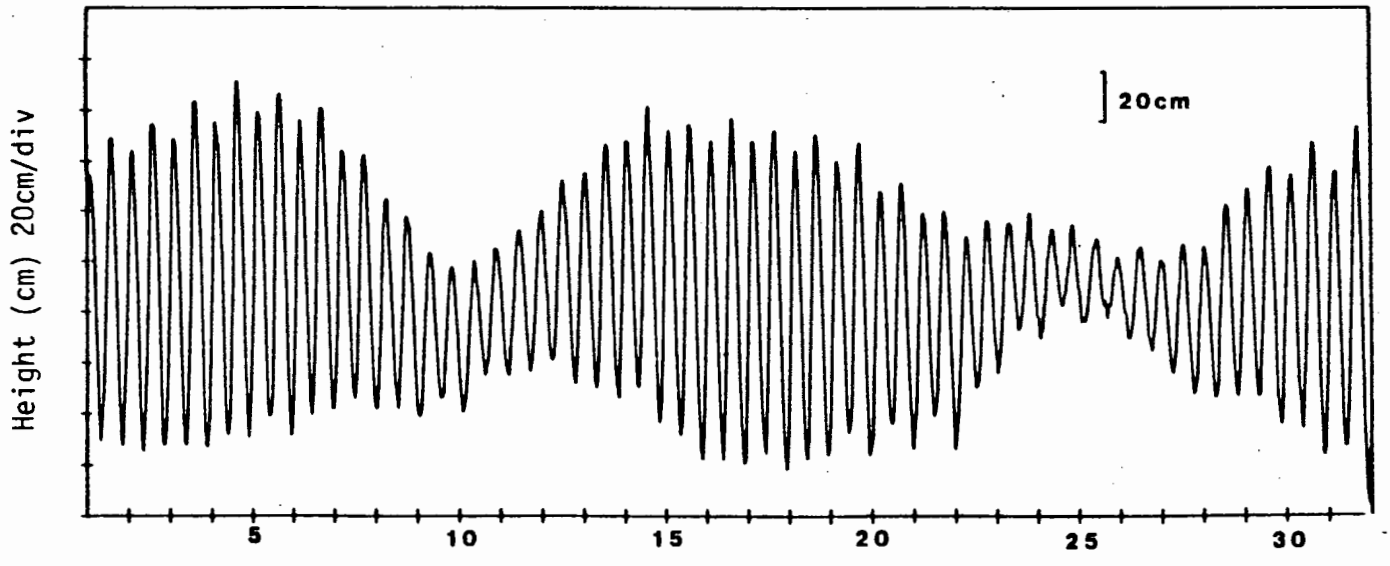

Simons bay sea level October 1982

(c) Starting with the equations of motion for fluids as a rotating earth, make appropriate assumptions so that you can derive the geostrophic velocity equation. (15)

Calculate the geostrophic, barotropic current at 30^{o}S latitude if the sea surface slopes up away from the coast by 1 metre in 100 km. If this current is on the east coast of Australia, in which direction does it flow? (15)

NOTES:

$$\frac{Du}{Dt} = -\frac{1}{\rho}\frac{\partial p}{\partial x} + fv + T_x$$

$$\frac{Dv}{Dt} = -\frac{1}{\rho}\frac{\partial p}{\partial y} - fu + T_y$$

$$\frac{Dw}{Dt} = g - \frac{1}{\rho}\frac{\partial p}{\partial z} + T_z$$

$f = 2\,\Omega \sin \phi$ rad/s

$\rho = 1000$ kg/m^3, $g = 10$m/s^2

(d) Discuss briefly the irregular phenomenon of El Nino in the Pacific Ocean giving some details of the Walker circulation and the southern oscillation. (30)

(e) Discuss the classical ideas of Ekman relating the vertical two dimensional current structure with depth to the wind stress at the surface.

By considering a lateral boundary and an equatorward wind stress, extend these ideas to give a simple model of coastal upwelling. (30)

(f) Write short notes on:
The Phillips-Miles theories of wind wave generation.
Wave spectra.
Sampling temperature and salinity in the sea.
The origin of the most dense water mass in the sea. (30)

UNIVERSITY OF CAPE TOWN

DEPARTMENT OF PHYSICAL OCEANOGRAPHY

Physical Oceanography 1b
November 1985

Time : 3 Hours
Answer ALL questions in Section A (40 marks)
and THREE whole questions from Section B

Total : 100 marks

SECTION A

Short questions. Answer ALL questions in this section.

1. Discuss the concept of a level surface and its relation to the local vertical, explaining the nature of the various contributing phenomena.

2. Explain the quasi-static approximation in the vertical balance of forces in ocean dynamics.

3. What quantity provides a contrast between the following curved currents; the South Atlantic gyre, inertial oscillations, and whirls in river flows.

4. Discuss the horizontal divergence of a geostrophic flow with particular emphasis on the relevance of the beta effect.

5. Explain what is meant by a dispersive wave. Is the Kelvin wave dispersive?

6. What is an amphidromic point?

7. Explain how wave energy can be concentrated at particular points on a coastline.

8. Explain how stratification can restrict the transfer of turbulence down the water column.

9. Discuss how the large scale wind field over the South Atlantic gyre can give rise to a deep central thermocline.

10. Explain how the Agulhas current can be "topographically steered" down the south east coast of South Africa.

(40 marks)

SECTION B

Long questions. Answer THREE whole questions only.

Question 1

The continuity equation can be interpreted as a balance between horizontal divergence and the vertical variation of vertical velocity.

Hence explain

(a) The deepening of a well-mixed layer
(b) The vertical velocity structure in a geostrophic flow
(c) The vertical velocity structure in a planetary scale geostrophic flow.

(20 marks)

Question 2

Many of the large scale surface currents of the ocean are confined to the upper layers of the ocean. Give a full explanation of the sense of the sea surface isobaric surface and the sense of the subsurface isopycnal surfaces associated with such a surface-confined geostrophic current in the Southern Hemisphere.

(20 marks)

Question 3

(a) For surface gravity waves on the ocean, the general geophysical fluid dynamic equations can be simplified considerably. By introducing two appropriate length scales and a time scale, show how the equations can be simplified to give:

$$\frac{\partial u}{\partial t} = -\frac{1}{\rho_0}\frac{\partial p}{\partial x}$$

$$\frac{\partial w}{\partial t} = -\frac{1}{\rho_0}\frac{\partial p}{\partial z} - g$$

$$\frac{\partial u}{\partial x} + \frac{\partial w}{\partial z} = 0$$

Simplify these equations further by splitting the pressure into dynamic and static contributions. Show that these two contributions to the pressure operate at vastly different scales. (You can consider typical waves to have amplitudes of 1 metre, wavelengths of 100 m, and periods of 10 seconds).

(b) Wave energy travels at the "group velocity $C_g = \frac{d\sigma}{dk}$. By considering special simplifications of the dispersion relation

$$\sigma^2 = gk \tanh(kh)$$

find the group velocity in "deep" and "shallow" water in terms of the phase velocity.

(20 marks)

Question 4

(a) In order to determine the tidal attraction due to the moon, we have to consider the variations in the angle γ which is subtended between the sublunar point M and a position P on the earth's surface. With the use of spherical trignometry, the term $(\cos^2\gamma - \frac{1}{3})$ in the tidal potential can be written as

$$\frac{3}{2}\left(\frac{1}{6} + \frac{1}{2}\cos 2\Delta\right)\left(\cos^2\theta - \frac{1}{3}\right)$$

$$+ \frac{1}{2}\sin 2\Delta \cos\alpha \sin 2\theta$$

$$+ \frac{1}{2}\left(\frac{1}{2} - \frac{1}{2}\cos 2\Delta\right)\cos 2\alpha \sin^2\theta$$

where θ is the co-latitude of P
Δ is the declination of moon
α is the transit angle (see accompanying diagram)

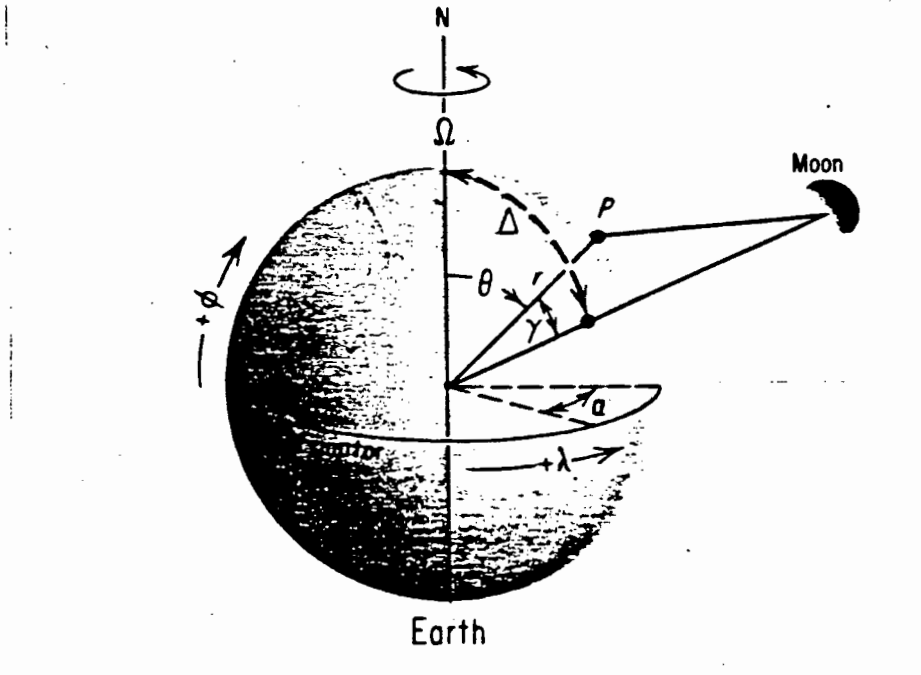

In the light of this equation, discuss the contribution to tides at long periods, diurnal periods and semidiurnal periods. Show also at which latitudes the long period, diurnal, and semidiurnal tides will be weak or absent.

(b) What will the speed of propagation of the tide be if the M_2 component has a wave length of 920 km and period of 12.42 hours? If the tide is considered as a shallow water wave, what would the the appropriate depth be to give the speed found above?

(20 marks)

Question 5

What is the cause of the surface layer phenomenon known as "ice-edge upwelling"? Provide the mechanism and give an opinion as to its frequency of occurrence in the Antarctic.

(20 marks)

Question 6

The full form of the conservation of potential vorticity of a wind forced surface layer of constant density is

$$\frac{d}{dt}\left(\frac{J+F}{h}\right) = \frac{1}{h^2 \rho_0}\left(\frac{\partial s^y}{\partial x} - \frac{\partial s^x}{\partial y}\right)$$

where J is the relative vorticity and h the thickness of the layer, f is the planetary vorticity and ρ_0 the density. The wind stress is (s^x, s^y) and the total time derivative follows the current. This conservation law is to be applied to an ocean gyre and western boundary current in the southern hemisphere.

Estimate the size of the right hand side and show that it is only important for time scales which are very long compared with $\frac{1}{f}$.

Explain how the fast western boundary current responds to its poleward flow along the boundary, and how the slow return gyre current supplies the "lost" vorticity.

(20 marks)

UNIVERSITY OF CAPE TOWN

DEPARTMENT OF CIVIL ENGINEERING

COURSE CE 5D5 : ADVANCED HYDRAULIC STRUCTURES

There is no written examination for this course.

The result will be assessed from two equal value projects.

Project 1 : Analysis of side channel spillway.

Project 2 : Analysis of side weir overflow.

September 1985.

(4 PAGES)

UNIVERSITY OF CAPE TOWN

DEPARTMENT OF CIVIL ENGINEERING

M.Sc. in CIVIL ENGINEERING

UNIVERSITY EXAMINATION : JULY 1986

CIV 516F : COASTAL HYDRAULICS

ALL questions may be attempted. Time: 4 hours

Constants

Sea water density = 1025 kg/m^3
Sea water height = 10 kN/m^3

QUESTION 1

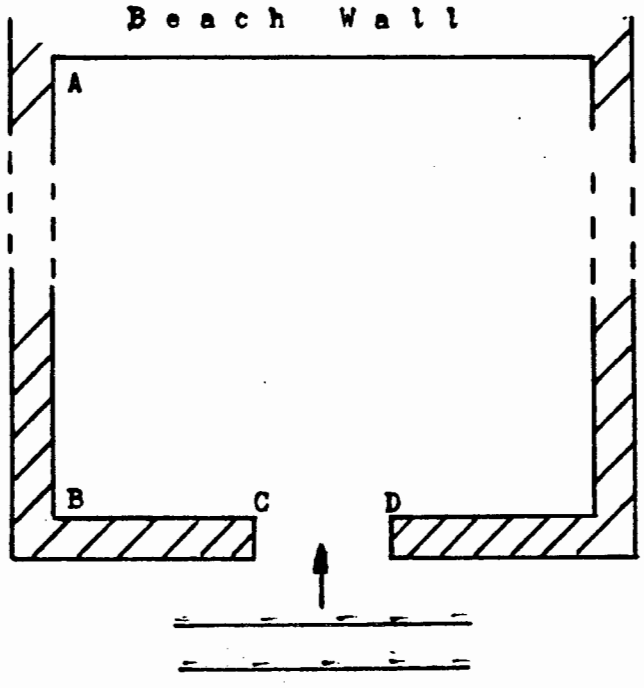

The diagram shows a rectangular shaped harbour with an entrance width of 174 m (CD) and side arm lengths of 261 m (BC). The harbour dimension to the beach wall is about 1,65 km (AB). If wave crests are approaching parallel to BC with a period of 10 seconds and a deep water wave height, H_o , of 4 metres, estimate the wave heights at 5 selected points along the wall AB and also at the harbour centre point. Give the angularity of the wave at the mid point of AB. Ignore refraction and reflection within the harbour, and take the water depth in the vicinity of the breakwater ends as 8,7 m. A selection of diffraction charts are available, ask for the one you need.

QUESTION 2

The standard alignment chart is attached, and a new blank line has been inserted at the bottom of the page. This line is to be used for determining values of u_{max} , the maximum horizontal orbital velocity at the bed, according to the Airy theory. If

$$u^*_{max} = \frac{u_{max}}{\pi H/_T}$$

is to be the dimensionless form of the variable on this line, mark off the positions of the u^*_{max} values given in the following list :

u^*_{max} =			
	0,01	1,00	5,00
	0,10	2,00	6,00
	0,20	3,00	8,00
	0,50	4,00	10,00

Note that H is the local wave height throughout. Suggest a small change in the line label which would permit the scale to be used for maximum horizontal acceleration values. Use the line to solve the following problem.

QUESTION 2 (continued)

A swell of 10 second period with a deep water wave height H_o = 3,2 m approaches a beach with the wave crests parallel to the shore. Plot the value of u_{max} at the bed versus depth from deep water beachwards. Suggested values for depth are:

73m 56m 31m 16m 5m

If the beach sediment is mobile when the bed velocity exceeds 1 m/s, find the depth when this first occurs and check whether this is outside the breaker zone.

(1 diagram attached)

QUESTION 3

(a) The attached diagram shows a wave height record, metres versus seconds. Use the diagram to find the following :-

i. significant wave height by definition
ii. significant wave height by CERC method
iii. significant wave height by the Draper method.

(1 diagram attached)

(b) A wave rider buoy is a type of accelerometer device used for wave height measurements. If such an instrument requires calibration in a laboratory, for a range of typical sea wave periods and wave heights up to 10 m, suggest a way of doing this.

(c)

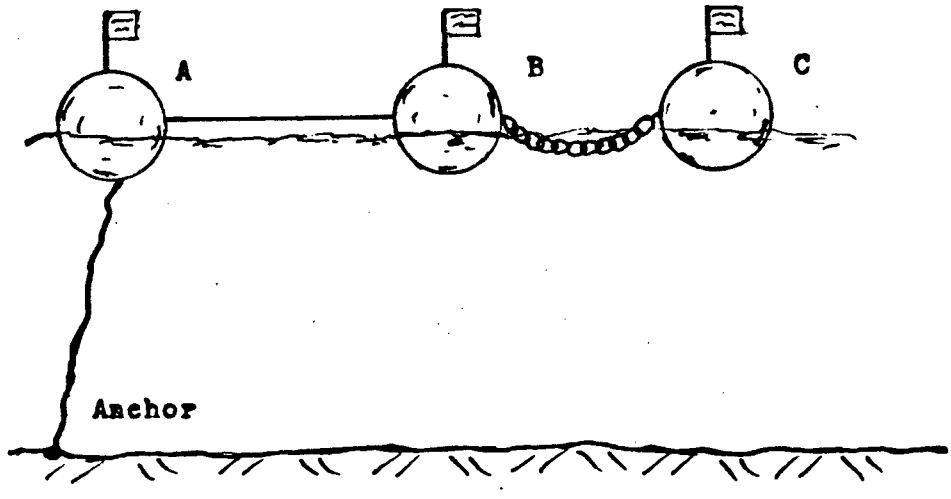

The diagram shows a device anchored to the sea bed outside the surf zone, where A, B and C are identical spherical buoys with visible flags on the top. A is joined to B with a nylon (lightweight) cord

QUESTION 3(c) (continued)

B is joined to C with a fairly heavy catenary chain. Suggest how an observer on the beach could use this device to take a coastal measurement, outline the detailed procedure and specify any beach instrument needed. State whether the device would need calibration.

QUESTION 4

A sea platform consists of a square concrete slab positioned horizontally on four cylindrical vertical piles, each placed at a corner, the slab side being parallel to the local wave crest. The pile diameter is 1 m, the total pile height above the sea bed is 6,4 m, and the slab dimensions are sides of 5 m with a thickness of 200 mm. The local wave characteristics are height 2 m, length 100 m, and period 12 s, the local water depth being 8 m.

(a) Considering the central 1 m high slice of any pile, calculate the horizontal forces per metre due to velocity and acceleration and by plotting these throughout one wave period identify the maximum force and the timing of its occurrence. Check that the velocity and acceleration distributions over the height of the pile are reasonably constant and thus estimate the total force on one pile.

Take $C_D = 1,2$ and $C_M = 2,0$.

(b) Estimate the maximum vertical force on the slab due to wave action.

Take $C_D = 1,0$ and $C_M = 1,8$.

QUESTION 5

In a study of wave penetration into a bay, the 9 m, 8 m and 7 m sea bed contours are approximated by three straight lines with contained angles of 12 degrees as shown on the attached page. An incoming wave orthogonal, 10 second period, impinges on the 9 m contour at an angle of 50 degrees as shown. With the usual approximations obtain by trial the angle at which the emerging orthogonal cuts the 7 m contour. Take the step lines on the 8,5 m and 7,5 m lines.

(1 diagram attached).

- - - - - -

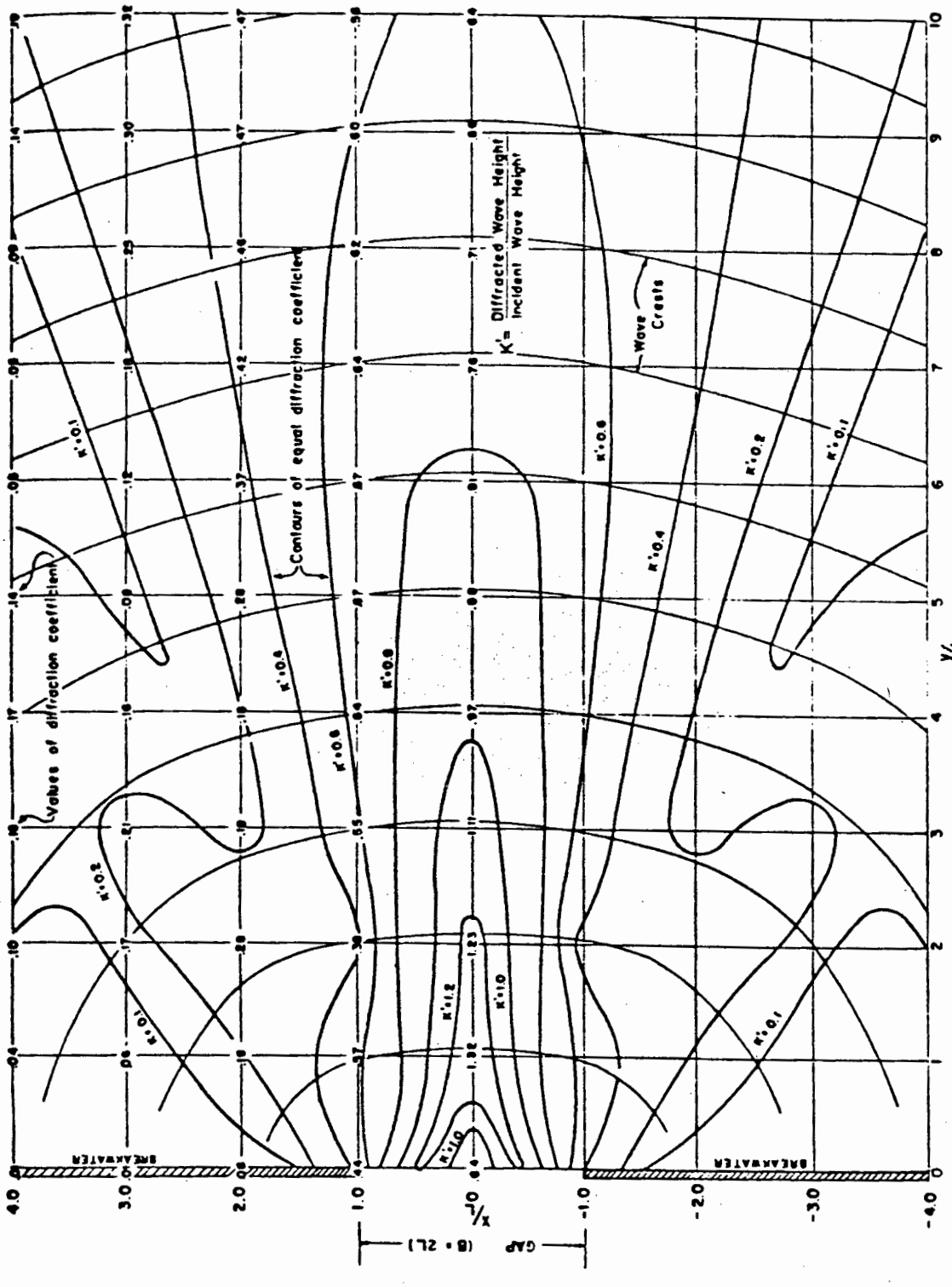

Figure 2-42. Generalized diffraction diagram for a breakwater gap width of two wavelengths (B/L = 2).

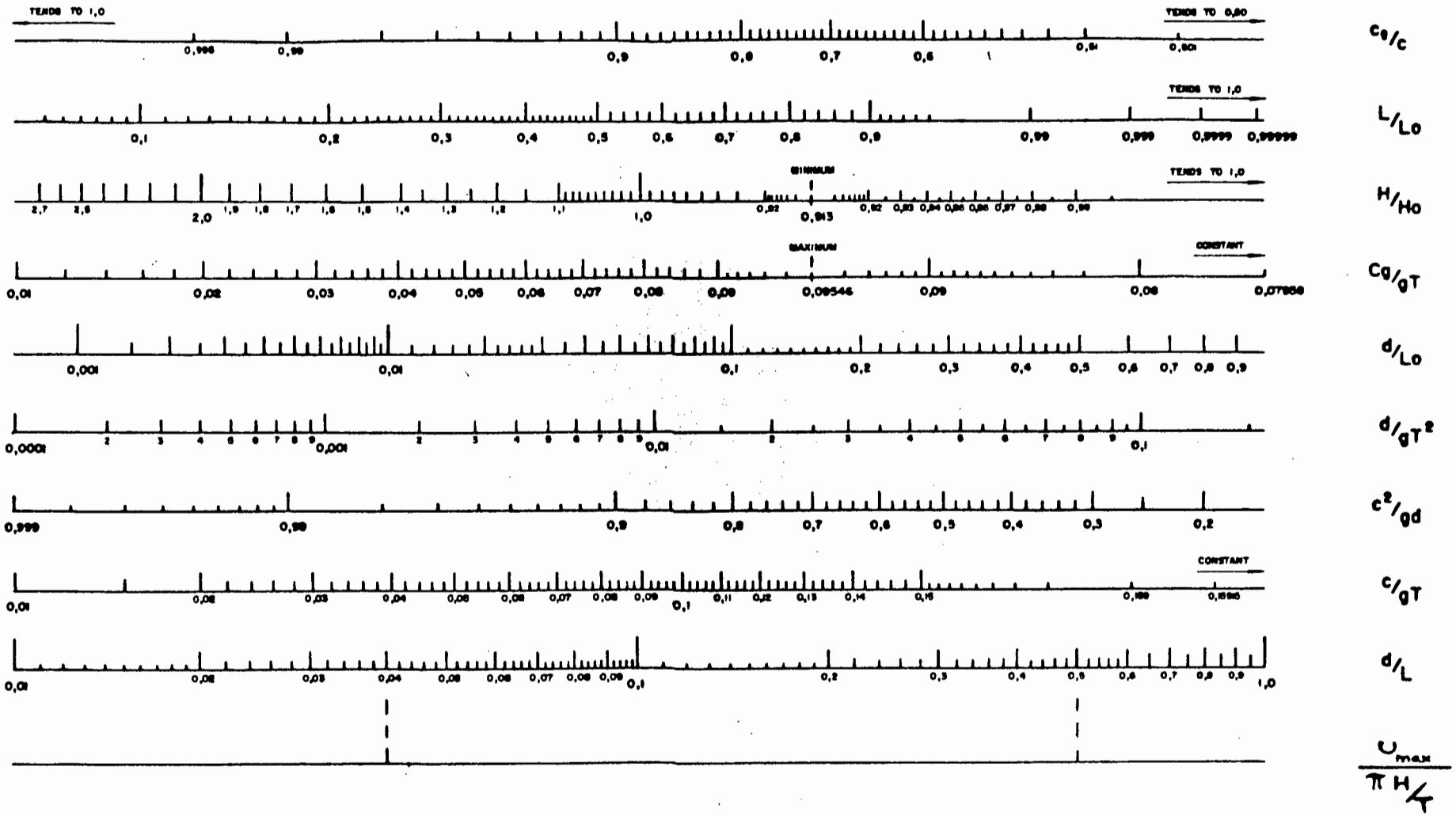

ALIGNMENT CHART FOR DIMENSIONLESS BASIC WAVE RELATIONSHIPS

PREPARED BY M J T
1977

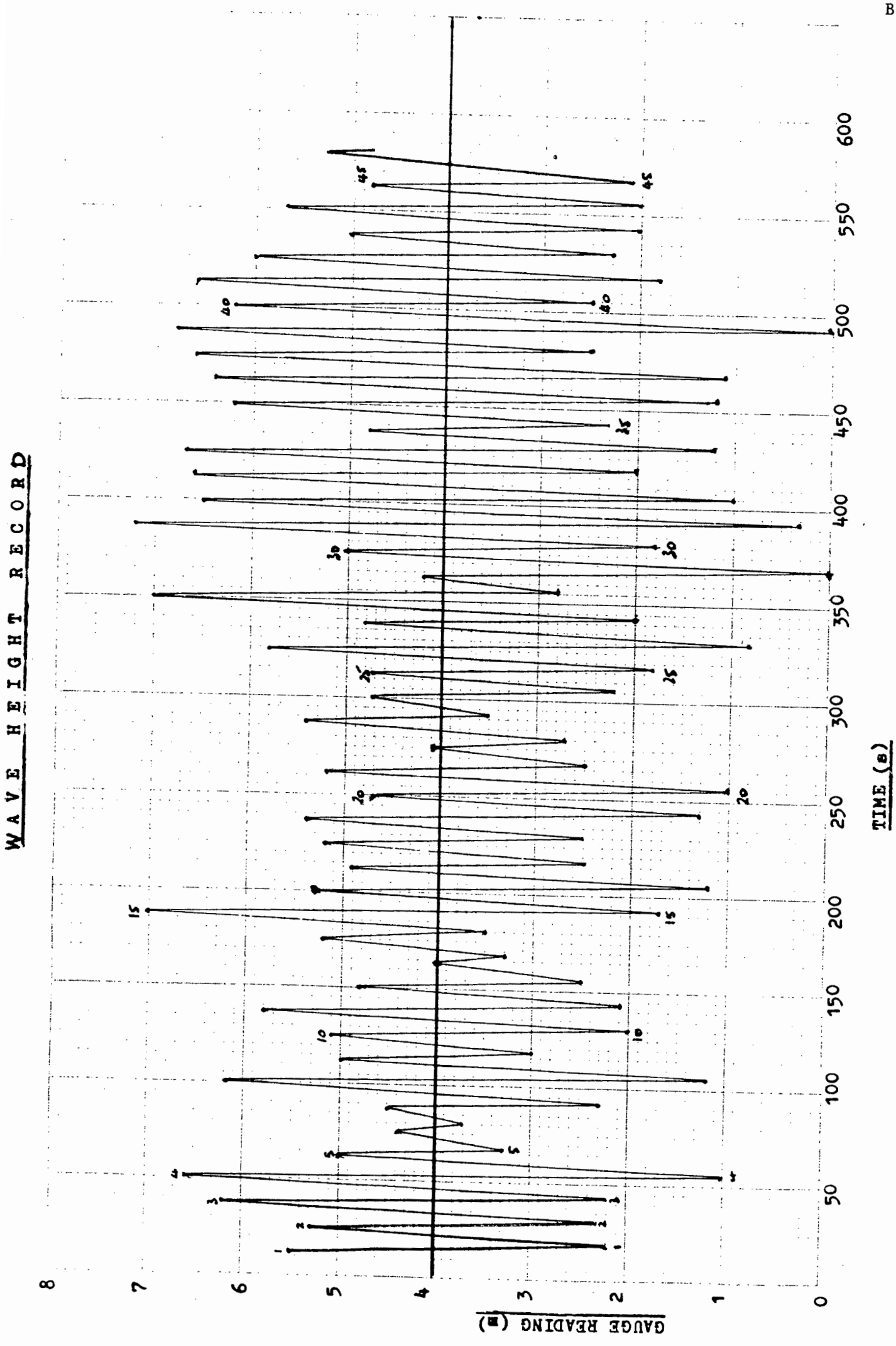
WAVE HEIGHT RECORD
GAUGE READING (m)
TIME (s)
0
1
2
3
4
5
6
7
8
50
100
150
200
250
300
350
400
450
500
550
600

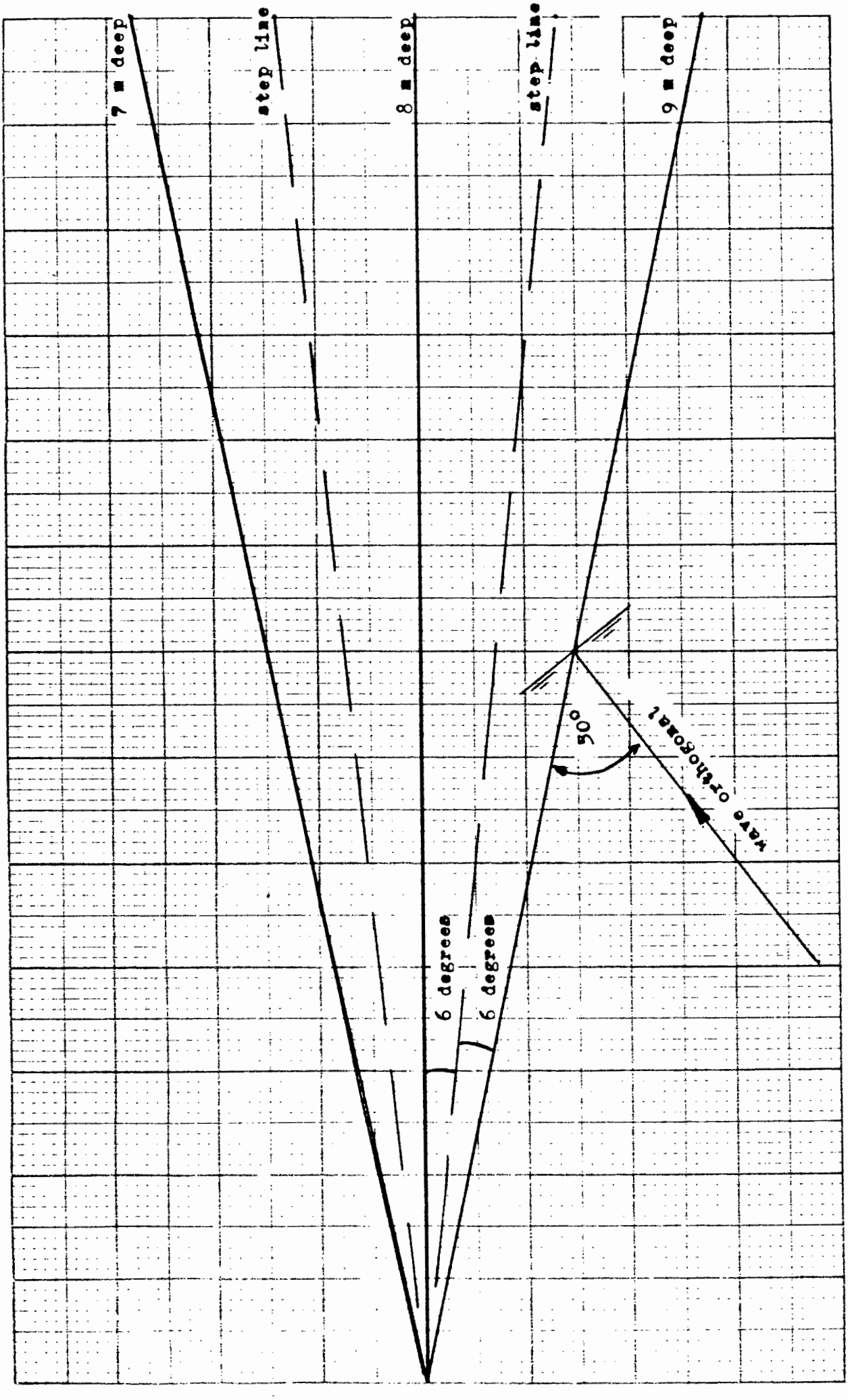
7 m deep
step line
8 m deep
step line
9 m deep
50°
new orthogonal
6 degrees
6 degrees